Re-evaluating the Interactions Between Sand Transport, Wind, and Ripples to Improve Aeolian Sediment Transport Prediction

by

Madeline Kelley

A Dissertation Presented in Partial Fulfillment
of the Requirements for the Degree
Doctor of Philosophy

Approved June 2023 by the
Graduate Supervisory Committee:

Mark Schmeeckle, Co-Chair
Ian Walker, Co-Chair
Christy Swann
Ron Dorn

ARIZONA STATE UNIVERSITY

August 2023

ABSTRACT

Sediment transport by atmospheric flows shapes landscapes on Earth and other planets. Improving the ability to quantify and predict sand transport by windblown (aeolian) processes has important implications for managing erosion, land degradation, desertification, dust emissions, air quality, and other climate change hazards and risks. Despite progress since Bagnold's seminal works in the 1930s, the most frequently used aeolian sand transport equations show discrepancies between predicted and observed transport rates upwards of 300%. Differences of this magnitude strongly support re-examining how fundamental physical aeolian processes are expressed in predictive equations.

Wind tunnel experiments using a Particle Imaging Velocimetry/Particle Tracking Velocimetry (PIV/PTV) system with a high-speed camera and high-powered laser were conducted to visualize fluid motions and sand particle trajectories to provide simultaneous measurements of wind flow and sand transport to re-examine the fundamental physical relationships between flow dynamics, sediment motions, and bedform development.

The first experiment of this dissertation focuses on the characteristics of near-surface sand transport in the saltation cloud. From PTV particle trajectories, mean particle velocities appear independent of freestream wind speed, while velocity distribution characteristics (such as modality) and particle concentration intermittency vary with increasing sand transport. Particle trajectories from rippled bed runs show evidence of local slope influence on near-bed particle vectors.

The second experiment used manual sand grain tracking to quantify particle-bed splash interactions. Results highlight that common rebound and ejecta functions do not sufficiently represent aeolian saltation splash events. Data indicate a shadowing effect of ripples, suggesting feedback between the saltation cloud, splash events, and bedform migration.

The third experiment used dual PIV/PTV analysis to quantify fluid-particle interactions and compare sand concentrations with fluid stresses and turbulence characteristics through the saltation cloud. Results show that increased saltation leads to the disappearance of the constant

fluid stress region, changes in aerodynamic roughness length, and increases in turbulence intensities. Leveraging technology advancements and multiple analysis methods, these results provide new, detailed information on the relationships between flow dynamics, sediment motions, and the presence of ripple bedforms. These novel empirical data illustrate some needed corrections to the theoretical and numerical frameworks for quantifying aeolian sand transport.

DEDICATION

My passion for science alone would not have carried me through this process. My wonderful family, friends, and colleagues made this possible. Thank you to my committee members, who gave me the freedom to try many ideas and the support when most failed. Their patience and kindness were just as important as their scientific expertise. Mark, thank you for letting me play with lasers and for your thoughtful responses to my never-ending questions. Ian, thank you for the many hours on Zoom and for encouraging me to follow my interests. Christy, you opened many doors for me. I would not be the passionate female geomorphologist I am today without you. Ron, I am a better teacher, writer, and science communicator because of you. I will always think of you while riding my mountain bike across this dynamic earth.

Ashley Kostial, Kate Zubin-Stathopoulos, Courtney Currier, Aldo Brandi, Norma Lopez, Liz Dietz, and Laureano Gherardi, your friendship has lifted me through many difficult times. Words cannot express my gratitude. My colleagues (and friends) Christian Gonzales, Zach Hilgendorf, Pete Tereszkiewicz, Nitzan Swet, and Collin Marvin, thank you for all the help, encouragement, and many enjoyable hours working together in the lab and field.

I had the pleasure of working with the amazing Micheala Roberts. This project would not have been possible without her. Micheala, you have many great talents, and I cannot wait to see your future accomplishments.

Thank you to everyone from Naval Research Lab Sediment Dynamics Section, especially Christy Swann, Joe Calantoni, Julian Simeonov, and Chuck Key. The opportunity to work with such extraordinary people made me a better scientist.

My big, wonderful family, including Ma, Da, Patrick, Nunnie, Gordy, Meme, Gigi, Katie, Tim, Jameson, Fiona, and Piper, I love you all. Their love made the distance easier to bare. My parents encouraged my wild dreams and sacrificed much to help me achieve them. Danny, I wish you could be here to see this.

Last but never least, Samuel Jordan, my loving partner, continues to be there for all the highs and lows. I cannot imagine achieving this without you (and Bat and Junebug) by my side.

Your patience and kindness know no bounds. Thank you for the many hours of assistance in the wind tunnel, the numerous trips to coffee shops, and for making it possible for me to disappear into the Grand Canyon, some far-off beach, or a laboratory for months at a time. I am excited to see where our far-reaching travels take us next.

ACKNOWLEDGMENTS

As a student of ASU, I would like to acknowledge that the Tempe campus sits on the ancestral homelands of those American Indian tribes that have inhabited this place for centuries, including the Akimel O'odham (Pima) and Pee Posh (Maricopa) peoples.

TABLE OF CONTENTS

Page

LIST OF TABLES

Table Page

LIST OF FIGURES

Figure Page

Figure Page

Figure Page

Figure Page

Figure Page

Figure Page

Figure Page

INTRODUCTION

This dissertation research grew from a combination of scientific interests and personal passions. Sand transport plays a role in shaping coastal regions, deserts, and semi-arid areas. Coastal zones constitute one of the world's most heavily populated and developed land zones (Luijendijk et al., 2018), while deserts make up about 33% of Earth's land area (Cherlet et al., 2018). Gaining an increased understanding of aeolian sand transport processes would reduce potential negative impacts on ecosystems, air quality and human health, infrastructure failure, and combating climate change (El-Baz & Hassan,1986). The sediment cycle, specifically the sand transport component, is of great academic interest but also highly valuable to societal vulnerabilities and risk management (Tessler, 2015). The opportunity to address basic science questions on aeolian processes with valuable implications for human society was a driving factor in tackling this research.

As a process geomorphologist, the ability to break down complex processes into key components is both extremely useful and exciting. Taking an experimental geomorphological approach, laboratory investigation allows controlled variable manipulation. Importantly, lab studies are reproducible and reduce noise by limiting environmental complexity (Seeger, 2017). The opportunity to apply new instrumentation systems with detailed testing and problem-solving brought me much joy. Thus, the opportunity to conduct novel research in the ASU Greeley wind tunnel before its closure was a personal highlight.

My interest in wind-blown sand stems from the theoretical simplicity of the transport system. The initiation of motion of individual grains occurs when forces from the wind exceed the forces on those grains that resist movement. Once grains are entrained, bedload sand movement is either by reptation/creep or saltation. The former term refers to travel in short hops near the bed surface (Andreotti, 2004). Saltating particles travel in ballistic trajectories that reach centimeters to possibly meters above the bed. Saltation drives other transport modes (Bagnold, 1941), and it underlies the initiation and growth of most aeolian bedforms (Nickling and McKenna Neuman, 2009). Since the initial work of Bagnold (1936), more insight into the complexity of non-

suspended transport and the interactions between the fluid and bed have guided aeolian geomorphology efforts.

Bagnold's series of papers (e.g., Bagnold, 1936) is credited as the beginning of the modern era of studying wind-blown sand. Since then, geomorphology has largely approached the processes of sand transport from a physics-based, mechanical perspective. The number of papers, reviews, and book chapters highlight the continued interest and questions within aeolian research. Some key reviews that shaped my thinking throughout this research include Sarre (1987), Anderson et al. (1991), Valance et al. (2007), and multiple chapters from the 2013 Treatise on Geomorphology, including Bauer (2013), Ellis & Sherman (2013), and Sherman et al. (2013).

Geomorphologists tackle problems at many different temporal and spatial scales. In experimental geomorphology, researchers often create scaled-down physical models to simulate natural processes such as erosion, sediment transport, and deposition. These experiments help to explore how individual variables (i.e., flow velocity or sediment size) influence a geomorphic process (i.e., initiation of particle motion). This reductionist approach involves simplifying natural landscapes into controlled settings to focus on specific processes. While this approach may not capture the full complexity of real-world environments, it allows scientists to examine individual factors and their contributions to landform evolution. The results obtained from laboratory studies can then be scaled up or integrated with other results to inform and validate models that aim to simulate real-world conditions.

An aeolian wind tunnel simulates the mechanics and transport of granular material under the influence of wind flow in the atmospheric boundary layer (i.e., the lowest part of the wind profile between the surface of the Earth and the free flow conditions of the overlaying atmosphere). R.A. Bagnold's wind tunnel studies obtained the first physically-based insight into aeolian dynamics (Bagnold, 1936, 1937, 1938). Since this ground-breaking work, researchers investigated a host of variables other than wind speed, including environmental parameters such as temperature (cryogenic), humidity (McKenna Neuman and Scott, 1998; McKenna Neuman and

Sanderson, 2008), and electrification (Rasmussen et al., 2009). While a substantial part of advances in understanding aeolian processes has come from wind tunnels, most aeolian geomorphologists acknowledge that small-scale, surface-process geomorphology cannot provide an understanding of long-term landscape development. Thus, aeolian geomorphology contains a combination of laboratory, field, remote sensing, and numerical modeling approaches at various scales.

Advances in instrumentation have influenced many subdisciplines with geomorphology (Rhoads & Thorn, 1996), and aeolian geomorphology is no exception. Several researchers have investigated saltation and splash with high-speed photography in wind tunnels. Zou et al. (2001) employed high-speed multi-flash photography to study the particle velocity distribution. Also, Dong et al. (2002) studied variations of the mean horizontal and vertical velocity of sand particles blowing over a gravel surface using a particle dynamic analyzer (PDA). Li and McKenna Neuman (2012) reported the vertical distributions of turbulence intensity with saltating particles using a custom-designed laser-Doppler anemometer (LDA) paired with particle tracking velocimetry (PTV). Unfortunately, few studies with instrumentation have captured a spatial continuous velocity field of both saltating particles and fluid motions.

2-D and 3-D velocimetry techniques have great application in measuring velocity fields of two-phase flows. The most attractive aspect of this optical approach is that it is possible to measure simultaneously the fluid and particles across a spatially continuous area. This dissertation research uses PTV and particle imaging velocimetry (PIV) to quantify the transport phenomena of sand in a simulated atmospheric boundary layer.

The first research chapter presents a study that aims to enhance our understanding of near-surface saltation cloud dynamics in relation to wind speeds and the presence of ripples. The interactions between transported sand, the fluid, and the bed have long been a subject of interest in geomorphology. While previous research has explored these interactions, none have used PTV to measure the natural saltation cloud across a wide range of wind speeds with active ripples.

How do particle velocities scale with wind speed? Do particle velocity distributions vary with height above the bed, location of ripple face, or volumetric flux? Does the variance in the concentration of particles change with wind speed? This study addresses these questions via PTV and quantifies the characteristics of particle trajectories.

This work represents the first phase of a three-part wind tunnel experiment on aeolian sand transport processes. The data on saltation cloud dynamics obtained in this study is the foundation for subsequent chapters that delve into splash events and interactions between the fluid and particles. Overall, this chapter contributes to the field of geomorphology by providing new insights into near-surface saltation cloud dynamics. The findings of this study pave the way for further research in understanding aeolian processes, including highlighting issues with common field models and parameterizing and validating numerical models.

The second research chapter addresses discrepancies in our understanding of splash dynamics. These data are needed to advance the theoretical and numerical models. Manually tracking is used on high-speed imagery to digitize impacts, rebounds, and ejecta. The experimental design aims to incorporate more natural conditions, such as including natural sand, the presence of ripples, fully developed saltation, and higher transport rates.

The results focus on quantifying the frequency, velocity, angle of impact, rebound, and ejecta particles. These data allow for estimating the coefficient of restitution, modes of transport, and influence of ripples. Insights into the influence of ripple slope help understand the potential shadowing effects on splash event mechanics. This study represents the second phase of a three-part experiment on aeolian sand transport processes.

By addressing these aspects of splash dynamics, this chapter works towards resolving discrepancies in aeolian sand transport theory and expands the empirical datasets necessary for numerical modeling and validation. The findings offer valuable insights into the mechanics of splash events and their dependence on wind speed, bed surface characteristics, and ripple slope.

The third research chapter utilizes PIV and PTV methods to investigate the characteristics of a boundary layer flow as the amount of saltating sand particles increases. The

objectives include quantifying the changes in fluid characteristics, specifically turbulence characteristics, and the contributions to the generation of Reynolds stress (RS) as sand flux increases. It also utilizes cross-correlation analysis to explore the relationships between near-bed instantaneous fluid velocities and sand concentrations.

The project seeks to enhance our understanding of the interaction between sand particles within the saltation cloud. These data contribute to advancing our knowledge of the complex feedbacks within the aeolian sand transport, improving our ability to predict and quantify sand transport in natural environments.

In summary, these three research chapters use improved technological advances to study the fine-scale processes of saltation. Results are important for broader geomorphic research as it enhances our understanding of fundamental processes, provide data for model development and validation, and help establish general principles. The hope is that this dissertation serves as an important building block for advancing our knowledge of sandy environments on Earth and other planets.

AEOLIAN SALTATION CLOUD DYNAMICS: PARTICLE CONCENTRATION & TRAJECTORY VARIABILITY WITH INCREASING WIND SPEED AND RIPPLED SURFACE

Introduction

Wind-blown (aeolian) sand transport promotes erosion of ventifacts (McKenna Neuman et al., 2022), increases dust emissions (Jones, 2001), initiates dune formation (Delorme et al., 2023), sand drift and dune dynamics (Livingston & Warren, 2019; Lancaster, 2023) and shapes the surface of Earth and other planetary bodies (Greeley & Iversen, 1985; Kocurek & Ewing, 2012). Dust emissions generated from aeolian sand transport produce public health hazards when the suspension of particulate matter surpasses US-EPA National Ambient Air Quality Standards (Ozer et al., 2006). Coastal dunes, formed from aeolian sand transport, can provide a natural buffer against the associated pressures of rising sea levels (Nordstrom, 1994). Thus, knowledge of aeolian sand transport processes is crucial for reducing potential negative impacts on ecosystems, air quality and human health (Zhang et al., 2016), infrastructure failure, and combating climate change (El-Baz, 2010). Many communities exist on or next to desert dunes (Seely, 1991), and many more live with coastal dunes (Martinez et al., 2004). The ability to quantify and predict aeolian sand transport remains an essential goal amongst geomorphologists, engineers, and environmental planners.

A suite of complex, interrelated processes govern aeolian sand transport, including the initiation of grain motion, air-particle interactions, splash dynamics, and ripple development (Kok et al., 2012). Various types of transport broadly separate into suspended versus non-suspended grain movement (Fig. 1), although this study focuses on non-suspended sand transport. Once the wind speed surpasses a threshold for motion, grains dislodge from the surface and follow a ballistic trajectory in a mode of transport termed saltation. Saltation is estimated to account for more than 75% of the total aeolian mass flux (Bagnold, 1936; Anderson and Haff, 1988) and is fundamentally linked to bedform development and dune formation (e.g., Parteli, 2022). The importance of windblown sand as a geomorphological transport system has been long recognized, but it was not until the early 20th century that scientists and engineers made

progress in predicting sand transport rates using wind and sand characteristics (Sherman & Ellis, 2022).

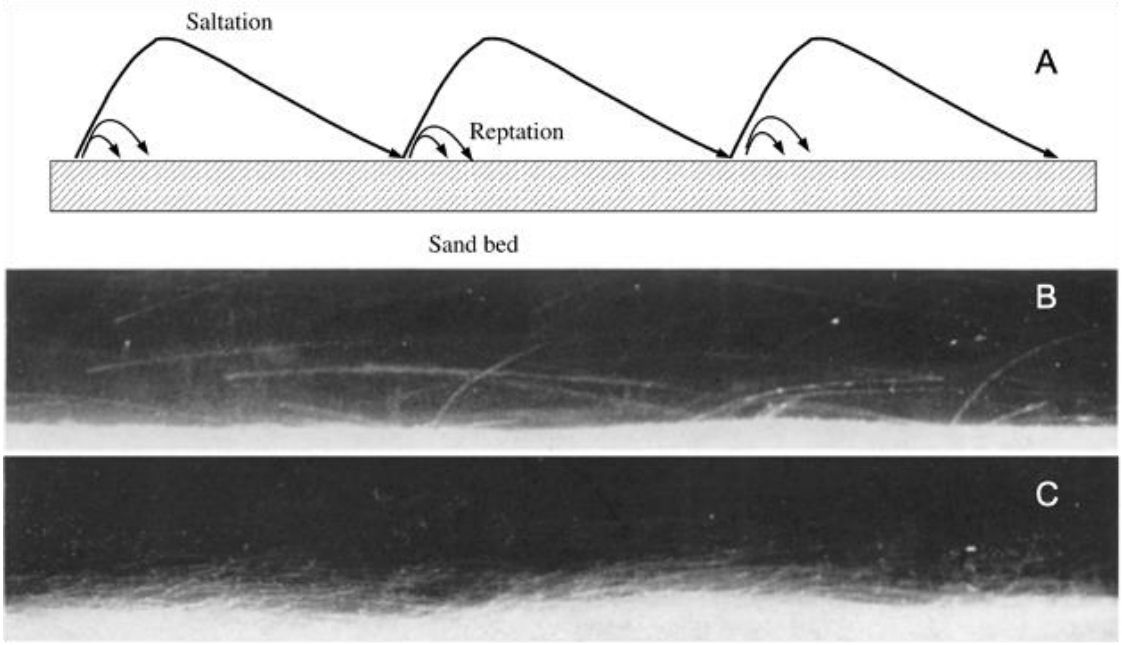

Figure 1: (A) Schematic of non-suspended aeolian sand transport modes: saltation and reptation/creep (Valance et al., 2015). (B&C) Photographs of saltation (Bagnold, 1936). The fainter downward tracks are those of fast-moving grains. (C) Imagery collected during increased sand movement with ripple development.

The most commonly used aeolian sediment transport models (e.g., Bagnold, 1941; Kawamura, 1951; Lettau & Lettau, 1977) predict sand transport as a cubic function of shear velocity, following the seminal work of Bagnold (1936). However, field experiments show these models often over-predict transport when tested in natural environments (e.g., Berg, 1983; Sarre, 1988; Chapman, 1990; McEwan and Willetts, 1994; Sherman et al., 1998; Dong et al., 2004; Bauer, 2009; Sherman et al., 2013). Discrepancies of up to 300% within each model and up to 700% between field observations and model predictions call for a re-examination of the fundamental physics and assumptions to resolve errors in prediction capabilities (Sherman et al., 2013).

Multiple issues have limited the development of a more accurate sand transport model, one of which is the lack of appropriate instrumentation to quantify fluid flow and transport response within the saltation layer. Traditional instruments (e.g., cup or ultrasonic anemometers, acoustic, piezoelectric, or laser particle counters) are typically bulky (Fig. 2) and often only provide single-point observations of sand or wind characteristics with varying resolution. These configurations aim to address a spatial resolution problem but cannot provide spatially continuous, near-bed measurements without obstruction. To address this issue, this study employs a high-speed (HS) camera system that can measure continuously (spatially) near the bed without obstructing wind or sand.

Figure 2: Tradition instrument array with a Safire spacing of 0.05 m and multiple cup anemometers. Dominant wind and transport direction is from the bottom right corner to the top left corner (Fig. 2 from Baas and Sherman 2005).

High-speed (HS) camera systems help solve some issues traditional anemometers and particle counters pose. White & Shultz (1977) pioneered the use of motion film photography with manual particle identification and tracking. Still, experimental observation of sand particles within a fully saturated saltation cloud remains challenging due to inadequate lighting, difficulties with

surface detection, and a high degree of error associated with particle detection and trajectory identification. In recent decades, instrumentation progress improved the capabilities of laboratory imaging and tracking velocimetry techniques for more accurately characterizing transport within the saltation layer (Dong & Wang, 2004; Dong et al., 2004; Beladjine et al., 2007; Zhang et al., 2007; Rasmussen & Sørensen, 2008; Wang et al., 2008; Creyssels et al., 2009). Particle Tracking Velocimetry (PTV) tracks a particle's displacement and velocity throughout a portion of its ballistic trajectory. Grain paths are recorded with an HS camera as they pass through a light sheet. Detected grains are then linked across sequential frames to produce a record of the grain's trajectory during the sampling period.

HS imaging systems are primarily used in wind tunnel simulations of saltation, which have limitations in experimental design and scaling. A saturated state saltation cloud requires the boundary layer flow within the wind tunnel to be fully adjusted and not influenced by fetch length, wall effects, or particle supply limitations. Table 1 updates O'Brien & McKenna Neuman's (2016) review of HS imagery/PTV with automated particle detection and trajectory identification. To our knowledge, no prior research has yet met the saturated particle cloud and sampling range criteria with natural ripple development while reporting the full particle velocity distributions.

Table 1: Summary and evaluation of wind tunnel experiments in which PTV has been employed to study sand transport (updated from O'Brien and McKenna Neuman (2016). Column headings are explained in footnote[1]. An asterisk (*) indicates the criterion was met.

Author(s)	Digital	Automatic		Frame rate (>1000 fps)	Saturated particle cloud			Sampling Range	3D	Bedforms
		I	II		Scale	Supply	Wind speed			
This paper	*	*	*	*	*	*	*	*		*
O'Brien and Neuman (2016)	*	*		*	*	*	*		*	
Zhang et al. (2014)	*			*			*			
Ho et al. (2014)	*	*	*	*	*	*	*	*		
Gordon and McKenna Neuman (2011)	*	*			*	*	*			
Yang et al. (2009)	*			*					*	
Creyseels et al. (2009)	*	*	*	*	*	*	*	*		
Gordon and McKenna Neuman (2009)	*	*	*			*	*	*		*
Wang et al. (2009)	*	*	*	*		*				
Zhang et al. (2008)							*			
Noguchi et al. (2008)	*	*					*			
Wang et al. (2008)	*	*	*	*		*				
Zhang et al. (2007)	*	*		*			*			
Beladjine et al. (2007)		*		*			*			
Rice and McEwan (2001)				*		*	*	*		
Nishimurai and Hunt (2000)						*	*			
Rice et al. (1996)				*		*	*	*		
Rice et al. (1995)				*		*	*	*		
Nalpanis et al. (1993)				*		*	*			
Willetts and Rice (1986)				*		*	*	*		
White and Shulz (1977)				*		*	*			

[1] Explanations from O'Brien and Neuman (2016): i. Digital camera. ii. Automatic I: computer aided image processing to identify particles and assign spatial coordinates. iii. Automatic II: trajectory identification and analysis. iv. Frame rate (FPS): >1000 feet per second. v. Scale: cross sectional area of the wind tunnel is large enough that wall effects are relatively small and saltating particles do not bounce off the roof for the respective wind velocity. The fetch of the tunnel working section is long enough for the concentration of particles within the saltation cloud to stabilize. vi. Supply: bed of sand covers the entire floor area of the tunnel working section and is sufficiently long and deep to avoid constraint on the supply of particles from the surface to the airflow. vii. Wind speed: wind speeds in the tunnel are varied in magnitude over a given range, and exceed that required for the entrainment of the bed material. viii. Sampling range: PTV sampling is carried out over a two-dimensional plane extending from the surface of the test bed to the top of the saltation cloud. ix. 3D: measurement of particle motion in three-dimensional space. x. (NEW) Bedforms: experiment includes runs with natural ripples in sand bed.

Impact ripples are decimeter-scale transverse bedforms that develop quickly once saltation begins and migrate on the surface of aeolian dunes or sand sheets by maintaining a nearly fixed profile in the direction orthogonal to the wind (Bagnold, 1941). Aeolian impact ripples form as reptating grains accumulate into small heaps and grow (Anderson, 1987). As saltating grains impact obliquely onto these heaps, the downwind side of a heap is less likely to be impacted during saltation, thus leading to sand accumulation and ripple growth. Although previous results suggest that splash dynamics differ with bedforms, limited experiments explore the saltation cloud and particle trajectories across ripples at a range of transport rates. Wilson (1972) suggested bedforms equilibrate and migrate in accordance with the current "equilibrium saltation" or "steady state saltation" conditions. Thus, understanding the interactions between the bed and the saltation cloud is critical to modeling aeolian sediment transport processes. Numerical models of aeolian ripple formation introduce systematic variation in particle trajectories along the wind-aligned axis of these bedforms. Yet, Manukyan & Prigozhin (2009) emphasize the experimentally derived statistics that are crucial for the parameterization of models are limited for sand bed surfaces bearing fully adjusted ripples due to a lack of data. Our efforts aim to directly correct this problem by exploring how the particle trajectories change across ripples.

Recent studies have reported the full distributions of near-bed particle characteristics rather than only the mean or median. Gordan & McKenna Neuman (2009) reported the distribution of energy lost for solid vs. loose beds and, later, Gordan & McKenna Neuman (2011), the distribution of impact and ejection speeds for sand vs. acrylic beads. O'Brien & McKenna Neuman (2016) quantified the frequency distributions for the particle component velocities. Jiang et al. (2022), for example, found that the lift-off velocity distribution of aeolian sand particles follows a bimodal distribution, contrasting previous observations of a unimodal distribution for these velocities. This finding is important for future numerical models of aeolian transport that aim to explicitly account for multiple species of aeolian particles, including saltating and reptating grains. Building on previous work, we provide horizontal and vertical velocity distributions across

flat beds and ripples to better understand how wind speed and ripple formation influence the saltation cloud.

This work expands our understanding of near-surface saltation cloud dynamics by quantifying particle trajectory characteristics (concentration, velocity, angle) in response to increasing wind speeds and the presence of ripple bedforms. The complex interactions and feedbacks between sand in transport, wind profile, and bedform morphology have long been of interest to geomorphology (Leeder, 1983; Best, 1993; Walker & Nickling; 2002). To the best of our knowledge, no experiment has measured the natural saltation cloud across this range of wind speeds with active ripple development. Our results focus on the inherent properties of the saltation cloud variability and flux, the momentum extraction by sand grains from the fluid and resultant particle velocity distributions, and links between ripples and modes of non-suspended sand transport (saltation). The present work is the first component of a three-part wind tunnel experiment on aeolian sand transport processes. Later projects build on these saltation cloud dynamics data to explore splash events and fluid-particle interactions.

Methods

Wind Tunnel Facility and Instrumentation

The experiments were carried out in the Planetary Geology Wind Tunnel at Arizona State University (ASUWT) (Greeley et al., 1983; Williams, 1987; Greeley, 2002). As detailed in Figure 3, the facility is a near-surface boundary-layer simulation tunnel with an open-loop suction design. The wind tunnel operates under ambient temperature and pressure conditions and can produce and maintain wind speeds up to 30 m s^{-1}. Its dimensions are 12.2 m long, 0.9 m high, and 1 m wide. Air is pulled into the tunnel by a large fan mounted in the downwind section of the tunnel. An inlet screen smooths and straightens the airflow as it enters. An array of roughness elements on the tunnel floor just downwind of the inlet trip the flow to initiate shearing flow and boundary layer development. The tunnel's bed is separated into an upwind (0-5 m) static bed roughened

with immobilized (glued) sand, while the downwind half (5-10 m) has a 5 cm deep active sand bed.

We used natural, unimodal, well-sorted, medium sand for all experiments with a D50 of 456 μm and a standard deviation of 1.13. This sand was used to fill the active section and was glued on the floor of the static, upwind section. Also, the airflow was seeded with the same sand from a hopper positioned 1 m downwind of the inlet. This initiated the development of saltation within the upwind sections of the tunnel and, thereby, extended the length of the test bed over which the flow was saturated with particles (O'Brien & McKenna Neuman, 2016).

All measurements were taken in the downwind, active bed section, which is enclosed with plexiglass doors for imaging and access to instrumentation. Downwind 9.5 m from the inlet, a side-mounted camera (Phantom Miro 341) captured sand particle motions in the horizontal and vertical directions. Image dimensions were 1024x768 pixels with a spatial resolution of 168 pixels = 1 cm and collected at 2353 fps. The sampling period was selected to balance data storage and resolution. Due to camera storage limitations, the number of images recorded in a single run was 10,692 images over 4.5 seconds. A laser sheet was created to illuminate particles moving through the imaging window using a 7-watt laser diode (nubm44-v2 450 nm) and a 5-degree Powell Lens (Laserline Optics). The sheet covered the entire length and height of the image window. Using a ruler, we measured the laser sheet width at 0.2 cm but estimated its effective illumination width to be 0.3 cm due to scattering at the bed. An Arduino board was used to synchronize the system. The program was based on an 850 μs cycle. The camera and laser received two activation pulses per cycle resulting in one image every 425 μs over a period of 4.5 seconds.

An RM Young Ultrasonic Anemometer Model 81000 3D sonic anemometer was located downwind of the imaging system and collected wind velocity measurements during all runs. The sonic anemometer was mounted upside down so that observations could be collected close to the surface; the center of the measurement area was 15 cm above the bed. During all experiments, the sonic collected u, v, and w velocity fluctuations at 32 Hz. Timestamps were used

to correlate the 3D velocity fluctuations with high-speed imagery.

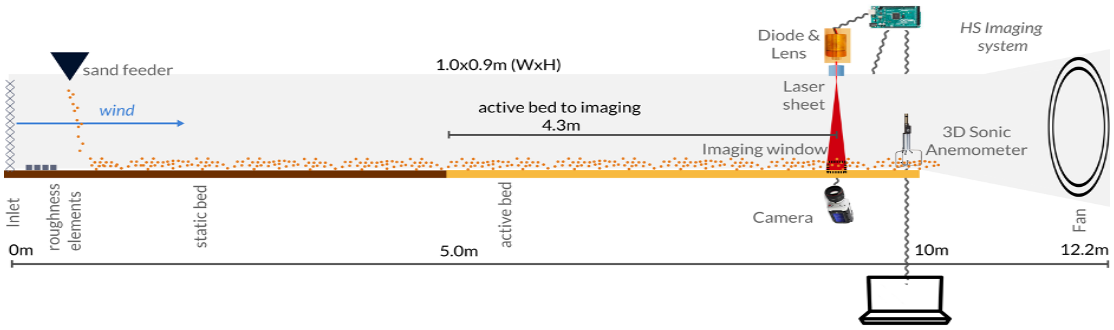

Figure 3: ASUWT with HS imaging system and 3D sonic anemometer.

Experimental Design

Prior to data collection, we ran a series of tests using the anemometer and a pitot tube that was vertically adjustable. We confirmed that the fan speed controller produced consistent freestream velocities and that the measurement location was within a fully-developed boundary layer (i.e., the vertical profile shapes followed the Law of the Wall characteristics and boundary layer thickness was comparable to results using Eq. 3). Given the proper design and settings, wind tunnels can simulate the surface flow of the atmospheric boundary layer. White (1996) outlines requirements for wind tunnel conditions to accurately replicate an equilibrated turbulent boundary layer using similarity scaling with the Reynolds number (Re) and Froude number (Fr) to verify that the fluid momentum exchanges and gravitational influences exerted on settling sediment grains by a simulation fluid-matched nature.

$$Fr = U^2/gH \qquad \text{Eq (1)}$$

$$Re = UH/\nu \qquad \text{Eq (2)}$$

Where U is the flow velocity (ms^{-1}), g is the gravitational constant (9.8 ms^{-1}), H is the height of the flow/tunnel, and ν is the kinematic viscosity. Using equation (1), our Fr values range from 7.1 to 14.5, which are below the suggested value of 20 (White, 1996). From Eq. 2 and our range of wind speeds, we estimated the boundary layer thickness (δ):

$$\delta(x) = 0.37(x/Re^{1/5}) \qquad \text{Eq (3)}$$

Using Eq. 2, our Re values ranged between 426,000 to 552,000 indicating fully turbulent flow. Next, using Eq. 3 and our Re values, our boundary layer thickness ranged between 0.25 m and 0.26m. White (1999) states that first, the downstream length of the measurement location (x) to tunnel height (H) ratio should be at least 5. Secondly, the downstream length of the measurement location (x) should be greater than 10 to 25 boundary layer thickness (δ) lengths.

The ASUWT's downstream measurement location (x) to tunnel height (H) ratio was 10.9; satisfying the suggested value of >=5. The ratio of the measurement location (x) to boundary layer thickness (δ) (from Eq. 3) was 65, satisfying the second requirement of >25. We confirmed our tunnel specifications for saltation cloud development against two criteria outlined by O'Brien and McKenna Neuman (2016). First, the cross-sectional area of the ASUWT wind tunnel was 0.9 m wide x 1.0 m high, which satisfies the recommendation of at least 0.5x0.5 m. Second, North (2014) reported that the aeolian transport system reaches a steady state at approximately 4 m from the upwind edge of a bed of medium sand (d = 250 μm) in the TEWT facility. The measurement location in the ASUWT was 4.3 m from the start of the active bed. Thus, with additional seeding of sand particles upwind (1m from the inlet), steady-state transport was achievable.

In summary, particles were sampled within (1) a fully turbulent boundary layer, (2) a saltation cloud equilibrated with the fluid flow, and (3) a transport-limited system. During these conditions, impacting particles provide the primary mechanism for entrainment and the maintenance of continuous saltation, compared to particle supply limited systems, where fluid drag and turbulent structures are key in maintaining transport phenomena (i.e., streamers). Thus, the common limitation of differences in the turbulent boundary layer structure between the field and laboratory has little implication for this study (O'Brien & McKenna Neuman 2018).

Table 2 shows the nine different experimental runs reported in this study. Runs were conducted on different days, 5/25 and 6/02/2020. For both days of the experiment, the temperature and humidity varied very little between runs (from 91-95°F and 7-8% on 5/25 and 105-107°F and 10-11% on 6/02). The tunnel freestream wind speed ranged from 7.0 to 9.5 ms^{-1}.

This range was selected to provide runs with data from just above the fluid threshold to higher transport rates. The active bed section of the tunnel floor was either flattened or had ripples generated prior to image acquisition during respective ripple runs. All runs resulted in 10,692 images except run 3, which had data corruption issues during transfer resulting in only 5,532 images.

Table 2: Nine experimental runs that vary in wind speed and bed condition (flat or rippled).

Run	Day & Bed Type	Duration (min)	Average U (m/s)	Total Images
1	2020/05/25 Flat bed	4.5	7.1	10,692
2		4.5	7.6	10,692
3*		2.4	8.1	5,532
4		4.5	8.6	10,692
5		4.5	9.1	10,692
6	2020/06/02 Ripples	4.5	7.0	10,692
7		4.5	7.6	10,692
8		4.5	8.7	10,692
9		4.5	9.2	10,692

Figure 4 provides an example of a typical run. Once the tunnel was started, sand was trickled into the feeder. The boundary layer was developed After 10s. We waited for an additional 10s to confirm the wind flow and saltation cloud had equilibrated. Figure 4 shows the flow became steady in terms of a stationary temporal average. Previous papers suggest that the saltation cloud adjusts within 1s of changing wind conditions. Thus, ten seconds is plenty of time to reach equilibrated conditions.

During the last 10 seconds (30 seconds from the start of the tunnel), we used data from the 3D sonic anemometer to measure 10s wind velocity averages and collected 4.5 s of HS imagery from the camera system.

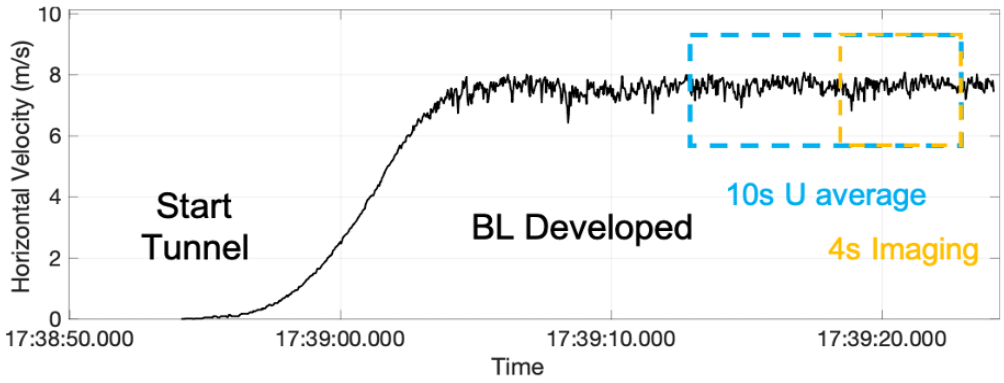

Figure 4: 3D sonic anemometer data from run 7. Once the wind tunnel is turned on, it takes about 10-20s for the boundary layer and saltation clouds to develop and reach a steady state. We used 10s averages to calculate the U mean from the 3D anemometer (blue box). Imaging occurs for 4.5s (yellow box).

Sand Tracking Method

The vertical concentration profiles and particle velocities were quantified from particle trajectories generated from an automated tracking algorithm TrackMate (FIJI/ImageJ) (Tinevez et al., 2017). Only visible particles in motion within a buffered area (1 mm above the bed and 3mm from the left and right sides) were tracked to limit high-reflectance issues near the bed and edge effects.

The algorithm uses a Laplacian Gaussian detector with an estimated object diameter (12 pixels), quality threshold (15), a pre-process median filter, and sub-pixel localization. Next, a Simple LAP tracker was used to track the detected objects with a linking distance of 55 pixels, a gap-closing max distance of 55 pixels, and a gap-closing frame of 2. We applied a post-tracking filter to remove low-quality tracks based on the number of detected objects in a track (i.e., a track must include a minimum of 4 spots), similar to the approach of O'Brien & Mckenna Neuman (2018). The results were exported as XML files for further analysis in MATLAB.

From x, y data coordinate pairs of particle locations captured between image frames in the horizontal and vertical dimensions, respectively, we calculated the u- and v-velocities and angle (θ) using Eqs. 4-6.

$$u_n = \frac{(x_{n+1} - x_n)}{(t_{n+1} - t_n)} \times s_{ms} \quad \text{Eq (4)}$$

$$v_n = \frac{(v_{n+1} - v_n)}{(t_{n+1} - t_n)} \times s_{ms} \quad \text{Eq (5)}$$

$$\theta = tan\left(\frac{Y}{X}\right) \quad \text{Eq (6)}$$

where s_{ms} is scale factor to convert from pixels/frame to ms^{-1} (0.14), t is the frame number, Y is the vertical displacement, and X is the horizontal displacement. Our results use particle characteristics of both edge and track datasets. Figure 5 provides a visualization of each. Once a grain is detected in sequential frames, the vector between two-time steps is called an edge. All edges for the same grain make up a track. We used the mean velocity and angle values of the edges to calculate track characteristics.

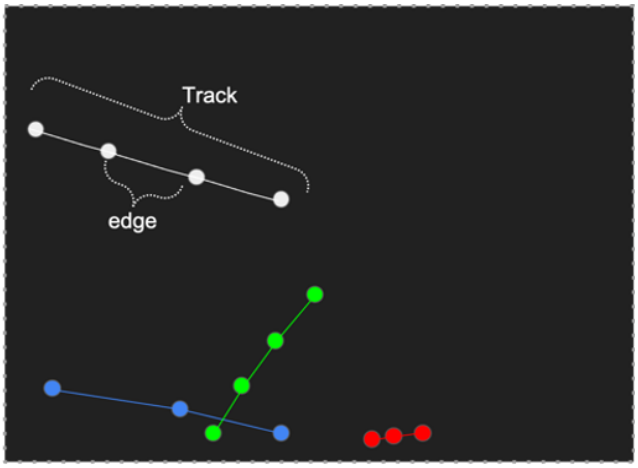

Figure 5: Visualization of object detection and linking. As a grain is tracked, edges connect its location between timesteps. A track is made of all the edges for each individual grain.

Validation of Automated Tracking

A sample of 30 images was used to validate the automated tracks generated by TrackMate. Sand grains in motion from the middle of run 8 were manually tracked and compared to the automated (auto) tracking results of the same frames. In Table 3, we summarize the results and show the trajectories from both methods in Figure 6. In the 30-frame sample, 16 grains were identified in both the manual and auto methods. Eight additional tracks were identified in the

manual but not in the auto-tracking method. One additional grain was identified in the auto but not in the manual tracking method. We calculated the mean differences in the x and y pixel locations of the same grains in manual and auto tracking as 2.6 and 1.7, respectively. This equates to less than a 0.02 cm difference for both.

In Figure 6A, we show all tracks from both methods. Figure 6B shows the detected grains from tracks that were identified using both methods. Note that while more grains are observed/tracked in the manual method, there is no spatial bias compared to the auto tracks (i.e., the manual method tracked additional grains at all heights). We attribute the fewer number of auto tracks to the quality threshold set in the algorithm. Given the small differences in object detection mean x and y pixel locations, we are confident in the auto-tracking method for our current purpose.

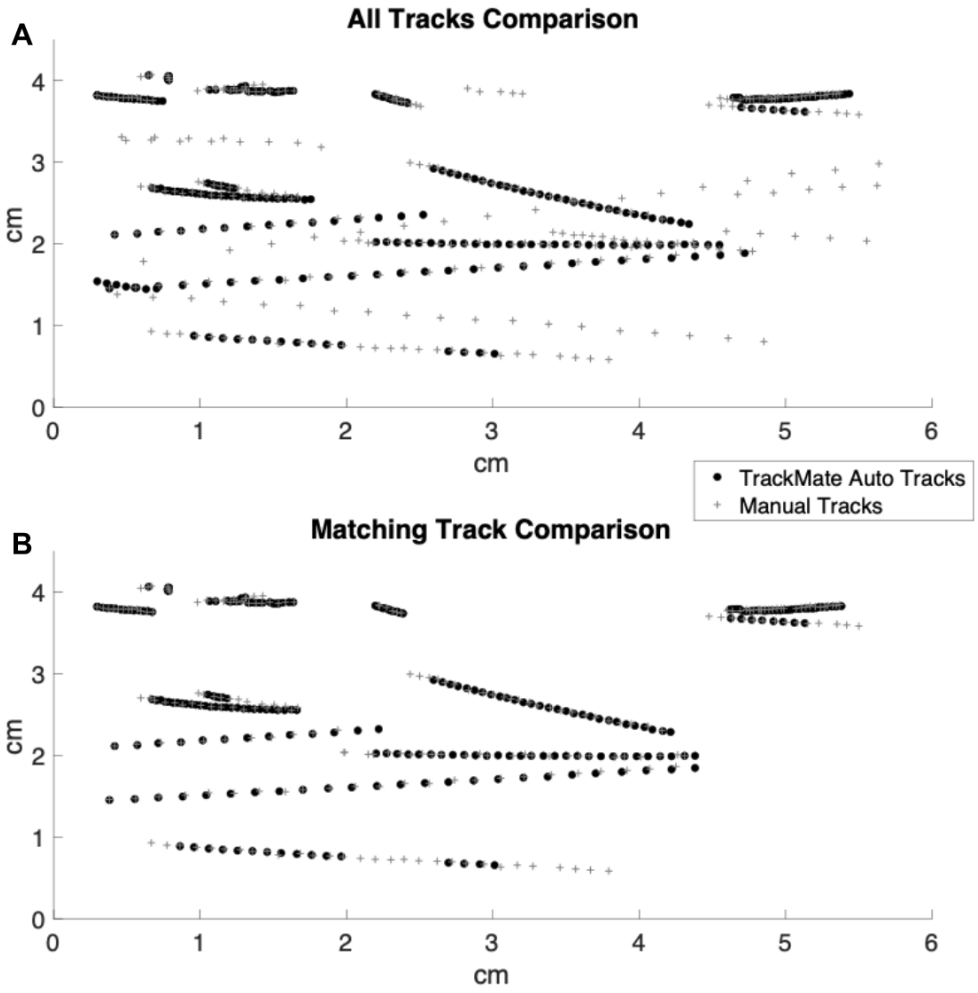

Figure 6: Manual tracking method versus auto tracking method. (A) shows all tracks. (B) shows only tracks that appeared in both the manual and auto methods' results.

Table 3: Results of manual tracking and auto tracking comparison

Total Manual Tracks	24
Total Auto Tracks	18
Manual tracks w/o auto match	8
Auto tracks w/o manual match	1
Total matched tracks	16
Mean difference (x pixel)	2.6

Results

We leverage the capability of this data by exploring multiple variables. First, we report the success of our automated sand tracking method compared to manual tracking. Then, we quantify the sand grain concentrations and wind velocity across each experimental run, discussing the temporal variability. Next, we produce volumetric flux profiles for each experimental run. We calculate the particle velocity distributions for each experimental run for both u- and v-velocities at various heights above the bed. Lastly, we explore the role of ripples by quantifying velocity and particle direction distributions across microtopography.

Run Conditions and Variability

In Figure 7, we show the anemometer data collected at 15 cm to demonstrate our near-stable wind conditions. The raw (32Hz) horizontal velocities, half-second moving means, and the 10-second stationary mean are shown for each run. Though the flow was straightened via the inlet screen, the roughness features and fetch length developed a turbulent shearing flow with some minor variability, which is fairly similar to that associated with natural saltation (White, 1996; O’Brien & McKenna Neuman, 2016).

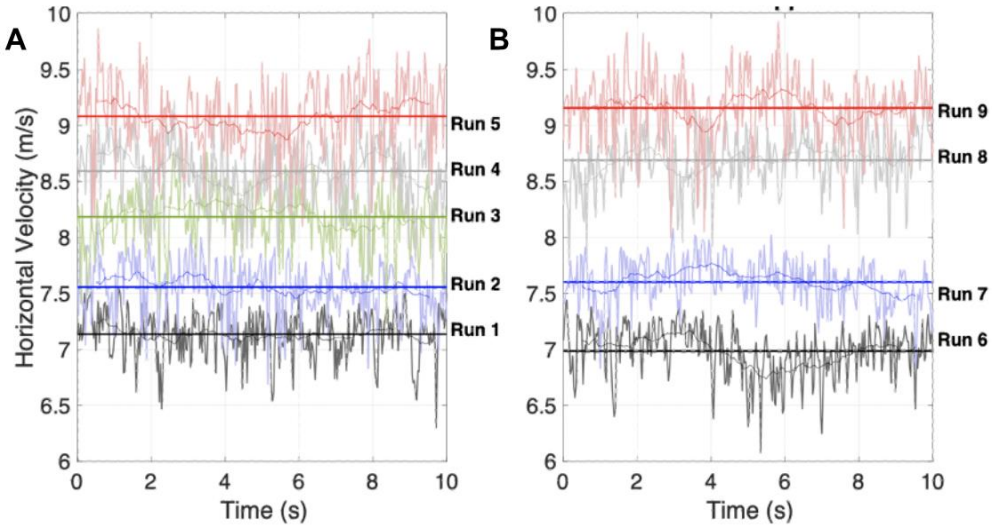

Figure 7: (A) Sonic anemometer data for flat bed runs 1-5, and (B)the rippled bed runs 6-9. For each run, we include raw data (32 HZ), 0.5-second moving mean (smoothed lines), and 10s mean (stationary).

Table 5 shows the total number of detected tracks, the mean value of particle counts per image, the standard deviation value of the particle counts per image, and the variance value of the particle counts per image for each run. The total number of sand grains detected increased with wind speed. Figure 8 shows the grain count time series for the duration of each run (the flat bed runs 1-5 are in Fig. 8A, and the rippled bed runs 6-9 are in Fig. 8B). All runs lasted 4.5 seconds except run 3. Runs 1 (flat bed) and 6 (rippled) had the slowest freestream (~7.0 ms^{-1}), which was slightly above the threshold of motion, and, accordingly, these runs resulted in the least amount of transport. The increase in grains in motion per frame was small, with a freestream of 7.5 and 8.0 ms^{-1} (runs 2, 3, and 7). We saw larger increases in grains in motion during faster wind speed (~9.0 ms^{-1}) runs 5 and 9 flat bed and rippled, respectively. Run 5 began with very high counts of grains in motion, then decreased to a range comparable with run 9.

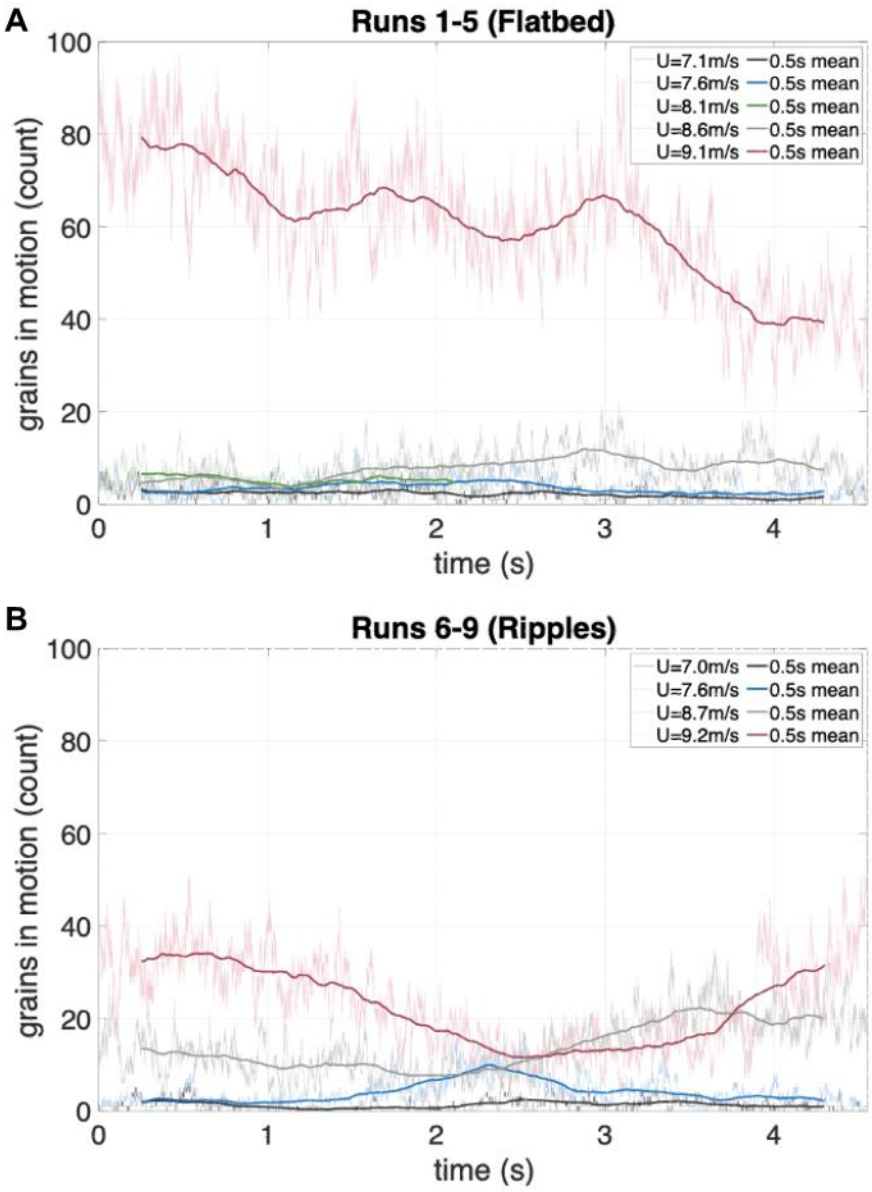

Figure 8: (A) Detected grains from high-speed imagery for all flat bed runs (1-5). Lighter lines show raw counts for each frame, and the darker line shows the half-sec moving mean. (B) Detected grains from high-speed imagery for all ripple runs (6-9). Lighter lines show raw counts for each frame, and the darker line shows the half-sec moving mean. Note: the increase in magnitude (y-axis) as wind speed increases. Note: Data corruption occurred for run 3 (8.0 ms^{-1}) during data transfer; thus, these data were limited to 2.5s. We limit the use of these data throughout the rest of our results.

Saltation is often an unsteady process (Butterfield, 1991; Stout & Zobeck, 1997), which is reflected in our datasets. Due to wind tunnel control, this variability is not linked to larger turbulent eddies or changes in humidity or bed moisture content. The grain counts, particularly for run 5, show a non-stationary time series (Fig. 8A). As a main objective of this study is to explore particle velocities, we plot the particle u-velocities for run 5 to confirm the quality of the data and experimental conditions. Figure 9 shows the horizontal particle velocities (both the original data and smoothed values using a half-second moving mean) time series for run 5 data (provide the SD for the dataset in ms^{-1} to support this?). Velocities fluctuate by a factor of less than two. The long-term trend of the time series is also approximately stationary, unlike the particle count time series for the same dataset (Fig. 8). Based on Bagnold's (1941) assumption that particle velocities scale with shear velocity, our mean particle velocities (Fig. 9) should not vary when the wind speed is held constant. Thus, our constant mean particle velocities (Fig. 9) suggest the particle detection and trajectories within the saltation cloud are correct, even though particle counts (Fig. 8A) fluctuated.

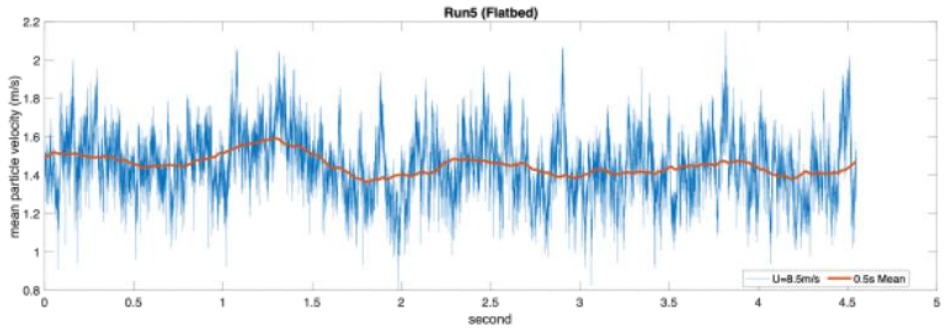

Figure 9: Particle u-velocity time-series for run 5 data.

To further explore the variability and randomness of the saltation particle counts, we plot the variance vs. the mean of grain counts per frame for each run from Table 5.

Table 4: The mean, standard deviation, and variance of the number of grains detected per frame for each run.

Run	Average U (m/s)	No. Sand Grain Tracks	$\bar{x}$	σ	σ^2
1	7.1	700	2.63	1.46	2.13
2	7.6	1,091	3.56	2.02	4.06
3*	8.1	891	5.40	2.63	6.90
4	8.6	2,494	7.55	3.55	12.58
5	9.1	24,663	60.38	14.53	211.05
6	7.0	419	1.89	1.15	1.31
7	7.6	1,250	4.13	3.00	8.97
8	8.7	5,069	13.95	6.14	37.68
9	9.2	8,867	23.21	9.82	96.44

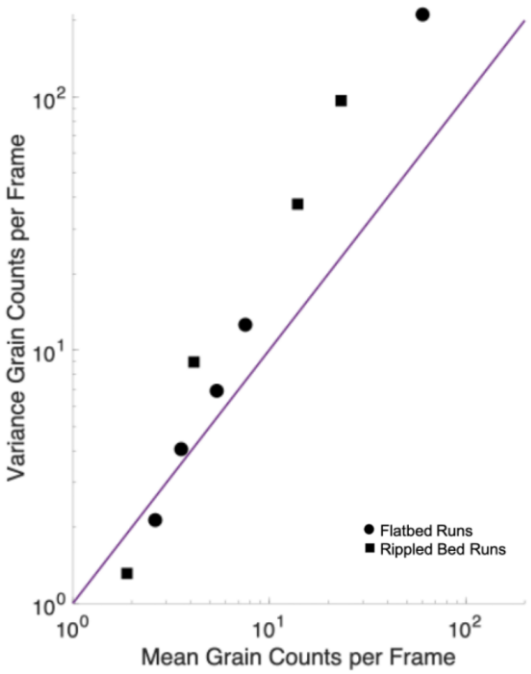

Figure 10: Variance vs. mean grain counts per frame for all runs. The purple line is the line of equality.

From Table 5 and Figure 10, we see that as wind speed and saltation increase, there is a simultaneous increase in the dispersion of particle counts. Figure 11 provides the grain counts per frame histograms for runs 1-5 and shows the deviation from a Poisson distribution as wind speed and saltation increase. These results suggest the saltation process leads to a broader

distribution of grain counts than expected if the process were completely random. Furthermore, the overall process of saltation leads to fluctuations in concentrations.

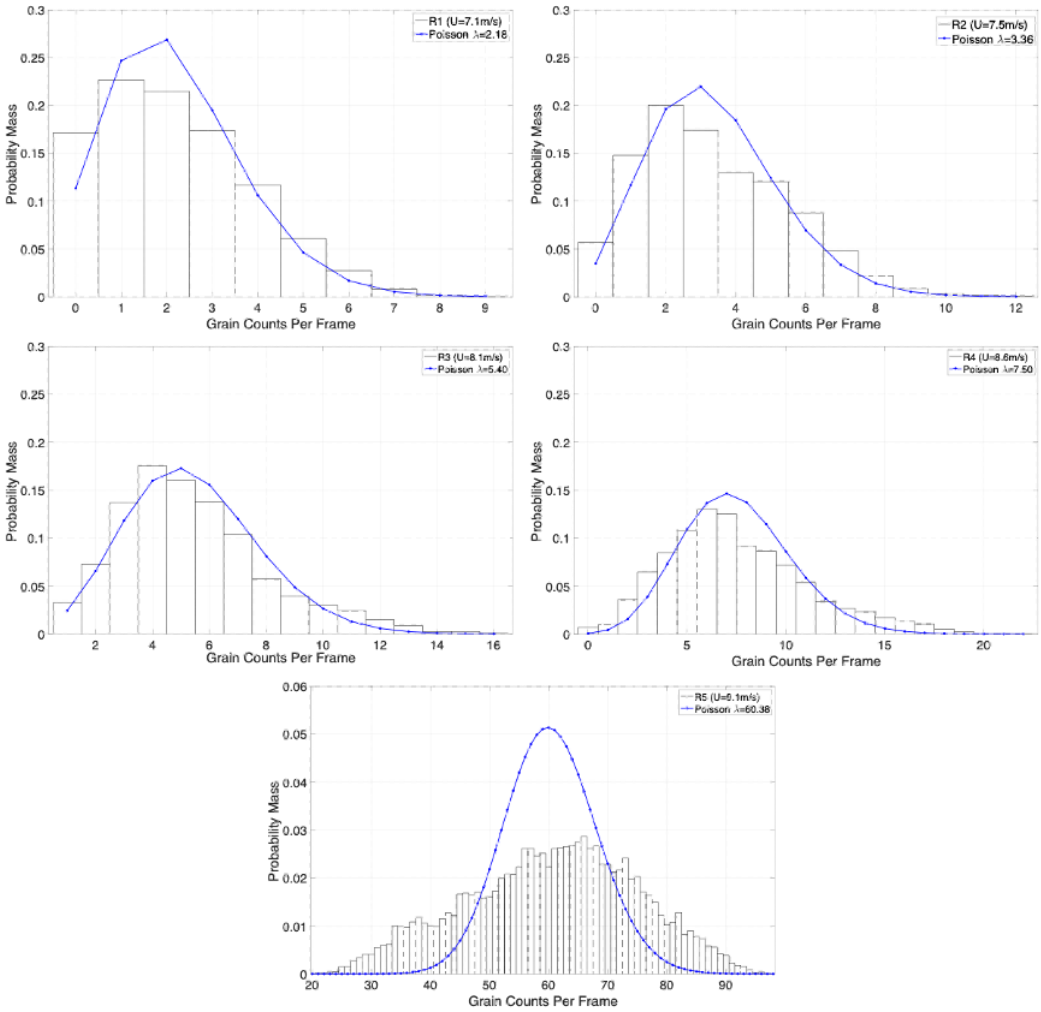

Figure 11: Grain count histograms and Poisson distribution fits for runs 1-5. NOTE: Run 5 has a different y-axis.

Vertical Volumetric Flux Profiles

Quantifying sand grains in motion and characteristic flux profiles are important to understanding the physics of grain behavior and modeling aeolian sand transport. We were able to quantify volumetric flux in 0.2 cm vertical bin increments. Figure 12 shows the bins for a ripple and a flat bed run with grain detection overlayed. Note that the lowest bin in the rippled bed runs

required an adjusted bin volume calculation to compensate for the ripple morphology (Fig 12 A). Volumetric flux (q_v) is calculated for each bin using:

$$q_{vi} = \frac{sum(edge\ displacement) \times v_s}{v_b \times t} \quad \text{Eq (7)}$$

where v_s is the grain volume (0.0495 cm^3), v_b is the bin volume (0.3277 cm^3), and the sampling time period is 4.5s (refer to Fig 5 for particle edge vs. track definition).

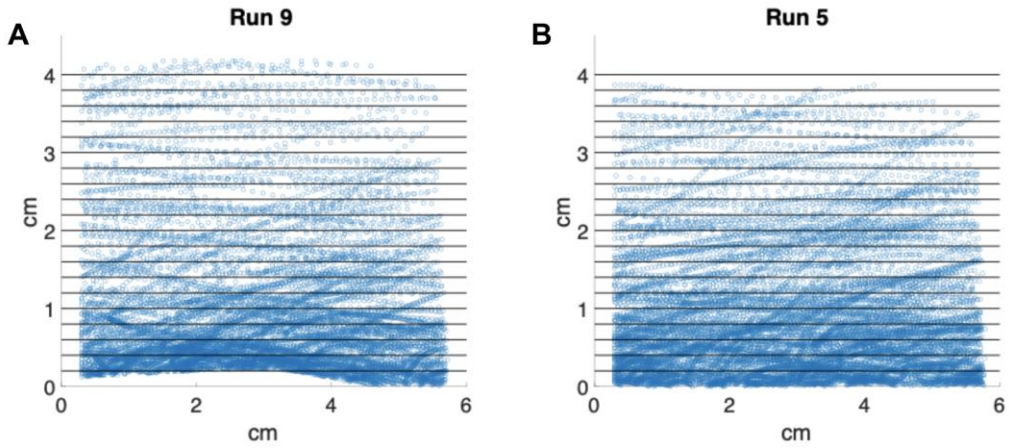

Figure 12: Vertical 2 mm bins (black lines) for volumetric flux profiles overlayed on a sample of detected grains from runs 5 (B) and 9 (A). (A) shows how the 0.2 cm vertical bins overlay a ripple. The bottom bin's volume is adjusted to subtract the ripple's area. (B, run 5) shows how the 0.2 cm vertical bins overlay the flat bed.

We calculate volumetric flux in 0.2 cm vertical increments (Fig. 12). We used the center of the vertical bin (height above the bed) for the y-axis. Figure 12 shows the vertical bins for flat (A) vs. rippled bed runs (b). For the ripple runs (Fig. 12B), we adjusted the lowest bin's volume to account for the ripple shape (i.e., the volume of the bottom bin is smaller because the ripple height is approximately 2mm).

Using Eq. 7, we calculate the volumetric flux to 3.8 cm above the bed for each run (Fig. 13A). There is an increase in the total volumetric flux as wind velocity increases. For most runs, the highest volumetric flux occurs slightly above the bed at 0.4 cm instead of the vertical bin nearest the bed. This is due to changes in concentration and particle velocities (i.e., though more

particles are moving closer to the bed, they are also moving slower). We did not see a strong relationship in flux changes due to ripples (runs 6-9).

Conventionally, flux measurements are normalized using either the total mass or volumetric flux (Chen et al., 1996; Dong and Qian, 2007). Using the volumetric flux profiles (q_{vi}) and total volumetric flux $(q_v)$from Eq. 7, we apply Eq. 8 to get the normalized volumetric flux (q_{vni}) values for each vertical bin:

$$q_{vni} = \frac{q_{vi}}{q_v} \times 100 \qquad \text{Eq (8)}$$

Figure 13B shows the volumetric flux and normalized flux profiles for each run. The profiles all follow a similar trend. The smaller sample sizes of the slower runs, and the resultant increased variability, are noticeable for runs 1 and 6. Overall, most sand transport occurred closer to the bed (<1 cm), which we refer to as the transport layer from here on out. For our datasets, 47-54% of the detected transport occurred within the transport layer. Also, our normalized profiles followed a similar decay rate with increasing distance from the bed.

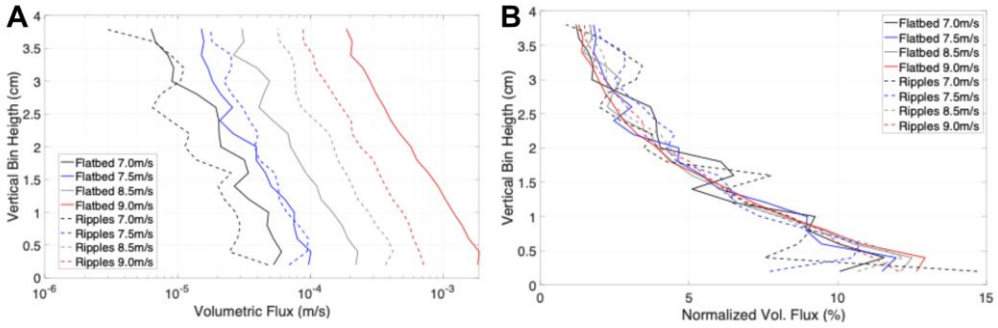

Figure 13: (A) Volumetric flux profiles from all runs. (B) Normalized volumetric flux profiles. Each bin is divided by the run total.

Particle Velocity Distributions

We use violin plots to show particle velocity distributions. Unlike the flux profiles shown in Figure 13, which use data associated with every particle edge, here we use the velocity associated with each particle track. Violin plots are a superset of box plots and give a richer understanding of the data distribution (Hintze & Nelson, 1998). They highlight multi-modal distributions or regions of very sparse data, which could go unnoticed in boxplots. They replace

the box shape with a kernel density estimate of the data. The kernel density estimation uses kernel smoothing for probability density estimation. It is a non-parametric method to estimate the probability density function of a random variable based on kernels (window functions). as weights. The bandwidth of the kernel influences the resulting shape/smoothing. We applied the suggested bandwidth of 0.3 after confirming it produced the optimum amount of smoothing while maintaining the distribution shape (Hintze & Nelson, 1998). Each distribution is set to a standard width of 0.5 in axis space (Bechtold & Bastian, 2016). The tail ends of the distributions are accurately represented and not smoothed to expand beyond the data min and max. For comparison, we provide histogram PDFs of the same data in the supplemental section.

Particle Velocities over a Flat Bed (runs 1-5)

First, we quantify the u- (horizontal) and v-velocities (vertical) for the flat bed runs at multiple heights above the bed. Previous work often only reports horizontal velocities since they contribute more to the total sand flux. However, near the bed, where particles impact and rebound, there are frequent conversions of horizontal into vertical momentum during the particle-bed interactions (Beladjine et al. 2007). Thus, we explore both velocity components.

Figure 14 shows the violin plots for particle (track) velocities at four heights above the bed for runs 1-5. For all flat bed runs, there is a noticeable trend between median u-velocities and height (see Fig. 14 and Table 6), with the median u-velocity increasing with distance from the bed. Also, the median value for the comparable vertical bin is similar for each run, though wind speed increases from 7.0 to 9.0 ms^{-1}. There are changes in the range of the distributions at similar heights across the runs. In general, the range increases with speed. The median v-velocities remain consistently around 0 ms^{-1} with height and wind speed. Comparing runs 1 and 5, the range of the v-velocity remains consistent with height but increases with wind speed.

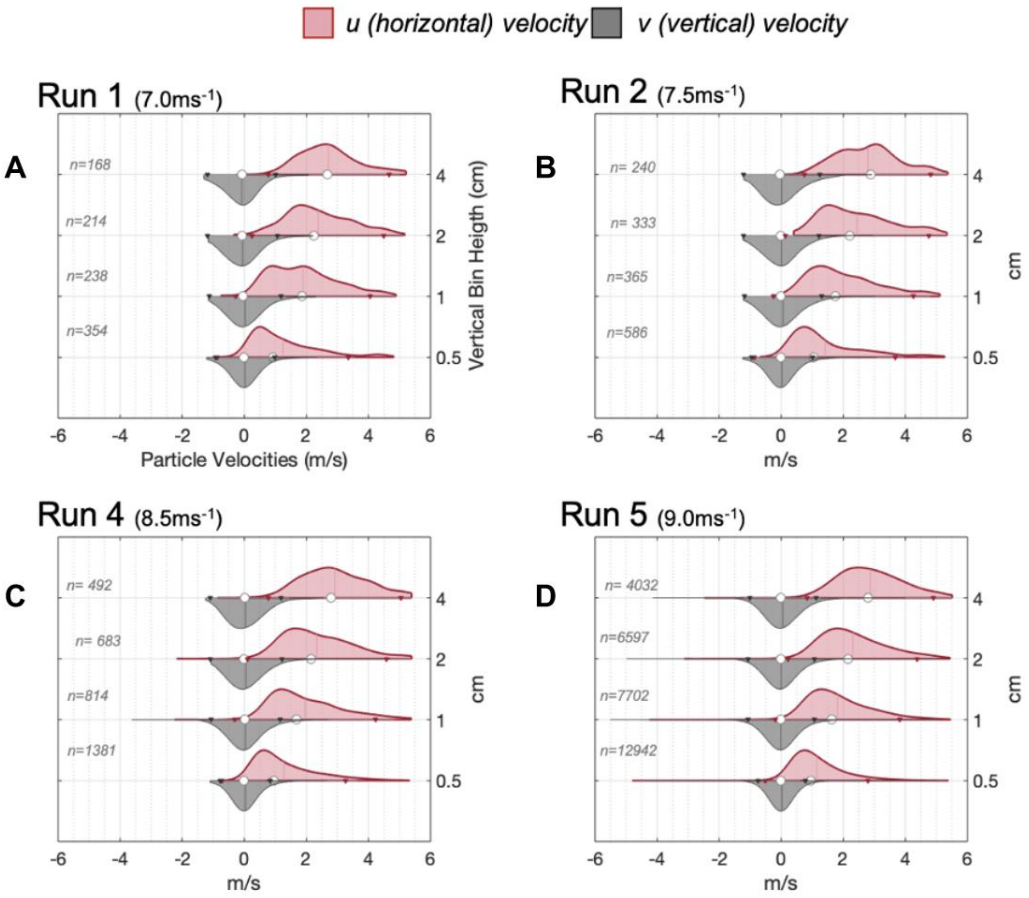

Figure 14: Violin plots of the horizontal and vertical velocity distributions from particle track data for runs 1-5. Trajectories have been separated into 4 vertical bins. The top/red violin plots are the horizontal velocities for each vertical bin. The bottom/black violin are the vertical velocities for each vertical bin. All data points are shown. The median for each distribution is indicated by the white dot. The mean for each distribution is indicated by a vertical line. The number of tracks for each vertical bin is shown to the left of the distribution. 2σ range is shown for each distribution by the inverted triangles.

Modality and Moment Statistics for Particle Velocities over a Flat Bed

The distributions show interesting characteristics beyond the median values. First, the u-velocity plots show multiple modalities (Fig. 14). For instance, run 1 at 0-1 and 1-2 cm vertical bins show multimodal distributions (Fig. 14A). Similarly, runs 2 and 4 (Fig. 14 B&C) also appear

multimodal at various vertical bins. The u-velocity distributions at all heights above the bed for run 5 (Fig. 14D) are more continuous/smooth with one dominant mode. In terms of the v-velocity distributions for all heights and all runs, there is a single mode that corresponds with the median value.

Table 6 shows the kurtosis and skewness values for each distribution. For all runs, the u- and v-velocity distributions have positive kurtosis values ranging from 2.69 to 9.28, which indicates that the distributions are considered peaked. Skewness is a measure of the asymmetry of the distribution, and values indicate the amount and direction of departure from horizontal symmetry. The skewness values for all runs indicate that the u-velocity distributions are mild (>0.1) to very (>1.0) positively skewed, and v-velocity distributions are also mild (>0.1) to very (>1.0) positively skewed, except for run 5, which at 2 cm and 4 cm has a mild, negative skewness.

Table 5: Moment statistics for all flat bed runs 1-5 using particle track data. A positive kurtosis value suggests peaked-ness. A positive skewed value suggests the mean is larger than the median.

	Vertical Bin	Track No.	Mean u-vel	u Kurtosis	u Skewness	Mean v-vel	v Kurtosis	v Skewness
Run 1	0-0.5	354	1.25	4.27	1.28	0.03	6.73	1.00
	0.6-1.0	238	1.89	2.77	0.53	0.03	5.11	0.97
	1.1-2.0	214	2.38	2.69	0.33	-0.06	4.91	0.87
	2.1-4.0	168	2.71	3.26	0.42	-0.08	5.27	0.68
Run 2	0-0.5	586	1.41	4.14	1.29	0.03	9.28	1.37
	0.6-1.0	365	2.00	2.94	0.75	0.06	5.86	1.04
	1.1-2.0	333	2.44	2.49	0.59	0.01	6.12	0.96
	2.1-4.0	240	2.79	2.72	0.22	0.02	4.78	0.89
Run 4	0-0.5	1381	1.28	4.44	1.30	0.04	6.97	1.08
	0.6-1.0	814	1.96	3.37	0.71	0.04	7.76	0.38
	1.1-2.0	683	2.34	3.25	0.45	0.06	9.73	1.45
	2.1-4.0	492	2.91	2.81	0.16	0.04	4.70	0.90
Run 5	0-0.5	12942	1.15	6.35	1.10	0.02	26.98	2.00
	0.6-1.0	7702	1.82	4.06	0.65	-0.01	15.64	-0.25
	1.1-2.0	6597	2.31	3.23	0.53	0.00	12.90	-0.22
	2.1-4.0	4032	2.87	2.97	0.22	0.05	6.70	0.60

Particle Velocities Across a Rippled surface

Previous research has focused largely on flat bed simulations. Our data include multiple runs with naturally developed rippled beds. Figure 15A1 shows particle u-velocity data for the

lowest speed runs for the rippled bed (run 6) and the flat bed run (run 1). We see noticeable differences between the stoss and lee u distributions when compared to each other and to the flat bed run (Fig. 15A1). On the upwind stoss side of the ripple, the horizontal velocity distribution has a median of 0.42 ms^{-1} compared to 0.78 ms^{-1} median value in the lee. The stoss distribution also has a narrower peak and range than the flat bed distribution (Fig. 15A1). The lee distribution also has noticeable differences compared to the flat bed (Fig. 15A1). The median values for lee and flat bed u distributions are comparable (0.78 ms^{-1} on the lee and 0.75 ms^{-1} flat bed) (Fig. 15A1). The lee u distribution peaks around 1.0 ms^{-1} and a smaller secondary peak of around 2.5 ms^{-1} Fig. 15 A1).

For the v-velocity distributions for run 6 (Fig. 15A2), all distribution ranges are narrower than the u-velocities, and the stoss v-velocity distribution is shifted towards the right/positive compared to the flat bed run, with median values of 0.12 and -0.00 ms^{-1}, respectively. The v distribution from the lee has a much narrower distribution than the flat bed data. Most of the v-velocities from lee are negative (downward traveling particles). The median values are -0.21 and -0.00 ms^{-1} for the lee and flat bed data, respectively (Fig. 15A2).

Figure 15B shows the mean particle motion vectors for the slowest wind speed runs (1 and 6) to illustrate differences between average particle trajectories of the stoss, lee, and over the flat bed. Particles on the stoss slope have an upward vector, the lee particles have a downward vector, and the flat bed particles have a relative level/flat vector. In summary, we see noticeable changes in the u-velocity distributions and net particle motion vectors when comparing the particles in motion at low transport states within the transport from the stoss of a ripple to the lee and to a flat bed.

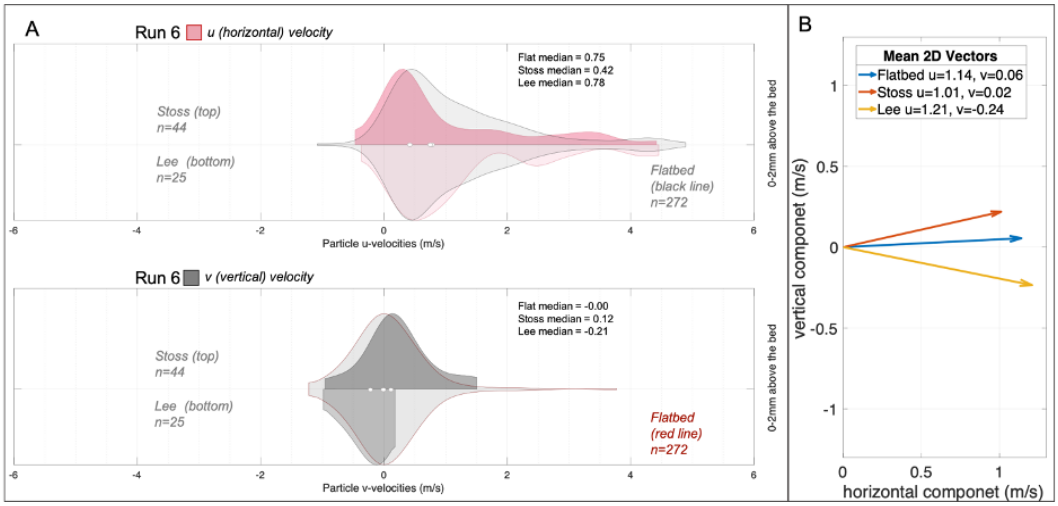

Figure 15: (A) u- (top/red) and v-velocity (bottom/black) distributions for lowest wind speed runs (1 and 6). The u-velocity plots include data from run 6 stoss (top/red) vs. lee (bottom/red) and flat bed run 1 (black outline; same top and bottom). The second violin plot shows the v-velocities for run 6 data from the stoss (top/black) vs. lee (bottom/black) and flat bed run 1 (red outline; same top and bottom). Data are limited to the 2mm AB. The number of tracks in each distribution is included to highlight the sample size. (B) Using the same datasets, the mean u- and v-velocity produce the resultant vectors to highlight differences in rippled bed and flat bed datasets.

Next, we explore the same variables but for faster speeds and higher transport rates (runs 9 and 5). In Figure 16a, the u-velocity distribution for the stoss data peaks at 0.4 ms^{-1} and has a median of 0.48 ms^{-1}. The distribution in the lee peaks closer to 1.0 ms^{-1} and has a median of 0.75 ms^{-1} and more closely follows the flat bed distribution than the stoss.

For the v-velocity distributions for run 9 (Fig. 16a), there is a similar shift in the stoss and lee datasets compared to the flat bed data, as seen in Figure 15A. The stoss data are shifted towards the right/positive values, and the lee distribution is shifted slightly towards the more negative values. The lee distribution is wider than the lee distribution for run 6 (Fig. 17a). The stoss, lee, and flat bed distributions have median values of 0.12, -0.10, and 0.02 ms^{-1}, respectively.

The mean particle motion vectors (Fig. 16B) for the highest wind speed runs (flat bed run 5 and stoss and lee from run 9) show the same trend as the results shown in Figure 15B. The stoss mean u- and v-velocities produce an upward vector, the lee data have a net downward vector, and the flat bed particles have a slightly upward vector (less so than the stoss vector) (Fig. 16B). Though the changes are more subtle than the lower wind speed runs, the stoss has more slower moving particles than the flat bed or ripple lee. on the lee of the ripple, there is a higher concentration of faster-moving particles than the flat bed. Comparing only the u-velocity medians or means of the datasets does not suggest the same results as the full distributions and vector plots of the u- and v-velocity data.

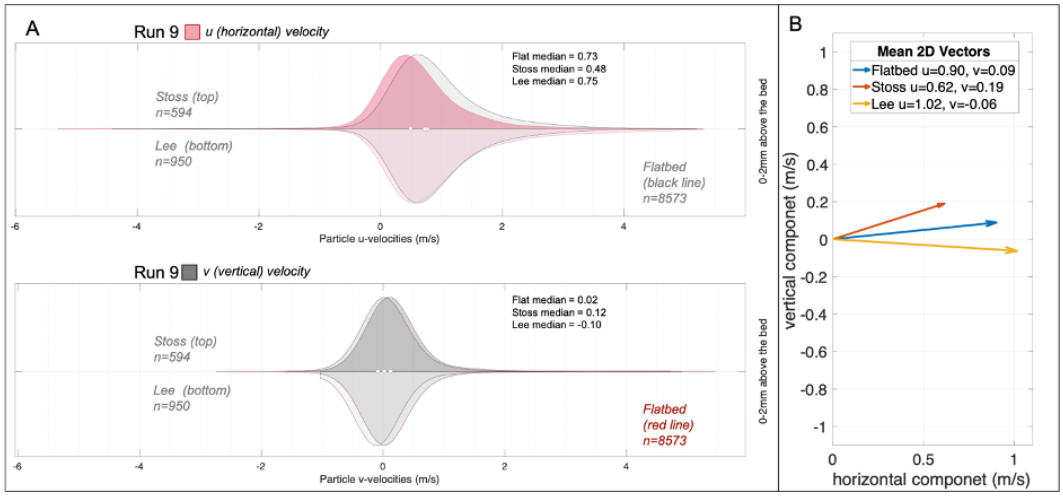

Figure 16: u- (top/red) and v-velocity (bottom/black) distributions for highest wind speed runs over flat and rippled beds. The u-velocities plot includes data from run 9 stoss (top/red) vs. lee (bottom/red) and run 5 (black outline; same top and bottom). The bottom v-velocities plot shows run 9 data from the stoss (top/black) vs. lee (bottom/black) and run 5 (red outline; same top and bottom). Data are limited to the 2mm AB. The number of tracks in each distribution is included to highlight the sample size. (B) Using the same datasets, the mean u- and v-velocity vectors are plotted to highlight differences in rippled bed and flat bed datasets.

Figure 17 is a bivariate histogram of particle u-velocities vs. particle x-direction location. The bin sizes are 0.1 cm and 0.2 m s--$^{-1}$ for the x- and y-axis, respectively. We select only forward-moving particles (u>=0) from the dataset for simplification and include a reference ripple at the bottom of the figure to help conceptualize how velocity and concentration distributions change across the microtopography. Each cell is colorized based on the count of occurrences. All plots use the same color scale.

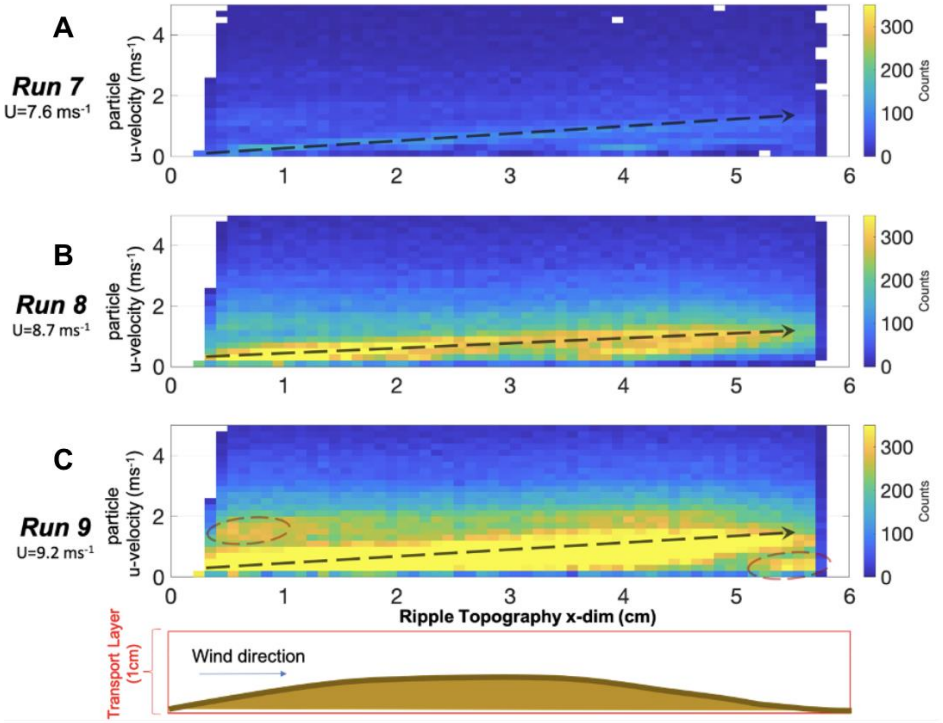

Figure 17: Bivariate histogram of particle u-velocity vs. x-direction location using particle edge data from runs 7-9 (A-C) over a rippled bed.

During run 7 (Figure 17A), as expected, we see lower counts in general due to lower wind speeds, which are associated with lower transport rates. Though faint, the velocity distribution shifts towards higher count values moving from the stoss to the lee. For run 8 (Fig. 17B) and run 9 (Fig. 17C), the same shifts towards higher particle velocities moving from the stoss to the lee become more visible. For run 9 (Fig. 17C), interestingly, there are new 'hot spots' upwind and downwind of the ripple at around 0.5 cm and 5.5 cm indicating an increase in the concentration of fast particles at the beginning of the stoss (0.5 cm), which is followed by an increase in the number of slow-moving particles at the end of lee (before the start of the next ripple). These areas (troughs) appear to have a bimodal distribution at higher transport rates. This

result was not visible in the violin plots since they are not inherently designed to show the continuous spatial variability of velocity distributions across the entire ripple wavelength.

Directionality and Modes of Non-suspended Transport Across Ripples

Until now, we have focused on the saltation concentrations and velocities of all particles in motion over flat and rippled beds. Using data from runs 5 and 9 (highest wind speed runs), we explore changes in particle trajectories due to microtopography for separate modes of non-suspended transport (i.e., creep/reptation vs. saltation) from within the transport layer. To separate by mode of transport, we use u-velocity thresholds based on the assumption that creeping and reptating particles move slower than saltons. For creeping or reptating particles, we use a threshold of greater than or equal to 0.5 $ms^{-1,}$ and for saltating particles, we use a second, higher threshold of greater than or equal to 1.0 ms^{-1}. These data are then further separated by run 9 for the ripple slope (stoss or lee) based on the x-pixel value. Particle directions are shown using polar histogram probability density functions (PDF), which use the number of observations in the bin divided total number of observations times the width of the bin (the area of each bar is the relative number of observations). The bin widths in Figure 18 are 30° and 15° for the creeping and saltating particles, respectively.

Figure 18A shows that trajectories of creeping particles differ in directionality across the flat bed, compared to the stoss and lee slopes of ripples. The near-bed creeping/reptating particles from both flat bed and stoss datasets peak at the 0° to 30° bin and have a similar resultant vector. The near-bed creeping/reptating particles from the lee (negative slope) peak at the 0° to -30° bin. For saltating particles (Fig. 18B), there are more subtle changes between the polar histograms for the flat bed, stoss, and lee data. All distributions peak between 0° and -15°. The slight changes in the distributions show a higher percentage of downward traveling saltons on the lee than over the flat bed and stoss slopes.

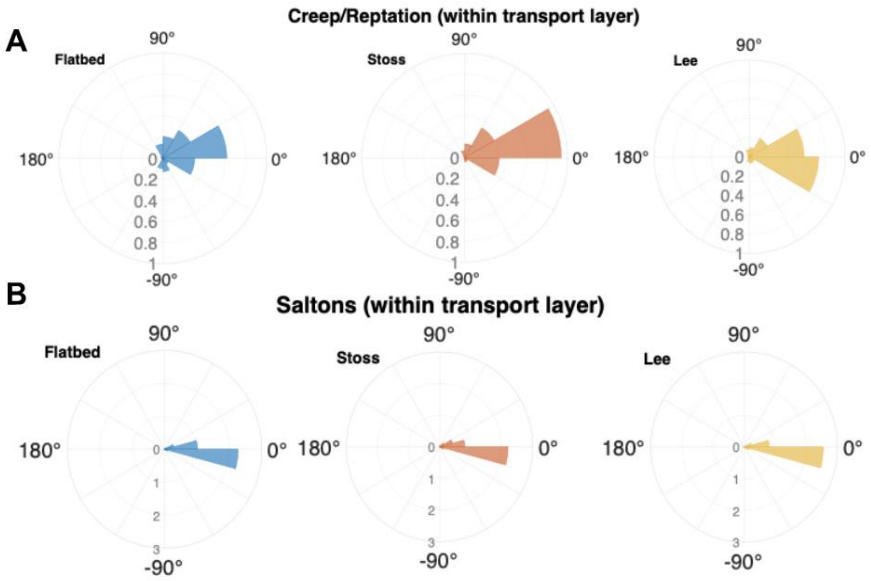

Figure 18: Near-bed, mean sand particle track angles in the transport layer (<1 cm) for (A) creeping/reptating and saltating (B) particles across different micrography for the same free-stream wind speed (~U=9.0 ms^{-1}). Polar histogram PDFs, and the bin width is set to (a) 30° and (b) 15°.

Discussion

Our dataset provides new insights on particle trajectories within the saltation cloud across various wind speeds and rippled bed configurations by overcoming previous difficulties related to lighting restrictions, bed reflectance, bedforms, and high sand concentrations. Our key findings include 1) an increase in over-dispersion of the particles with increasing wind speed and resultant sand transport, 2) a consistent exponential decay rate of normalized volumetric flux, 3) consistent mean particle velocities with increasing wind speed, 4) changing modality, kurtosis, and skewness of particle velocity distributions, and, lastly, 5) changes in trajectories and modes of transport across rippled beds.

Fig. 19 conceptualizes results on particle velocities. Sand transport across a flat bed is conceptualized in Fig. 19A and B. As wind speed and sand transport increase, the mean velocity

remains the same but the distributions shift from bimodality to unimodality. There is a more gradual decrease in the concentration of particles from slow-moving creep to high speed saltons.

Fig. 19 C&D reflect the added complexities that ripples impose on particle velocity. Again, as wind speed and sand transport increase, the mean velocity generally remains the same but the distributions shifts from bimodality to unimodality. Yet, microtopography drives additional differences in modes of sand transport. Fig. 19 C&D show high-speed saltons impact with the bed more on the stoss slopes. Bed impacts (i.e., splash events) often result in newly elected, slow-moving creep/reptating particles. The lee of the ripple appears to also have higher mean velocity values due to fewer splash events and less creep. Thus, the distribution shapes and shifts during higher sand transport are different on the stoss and lee.

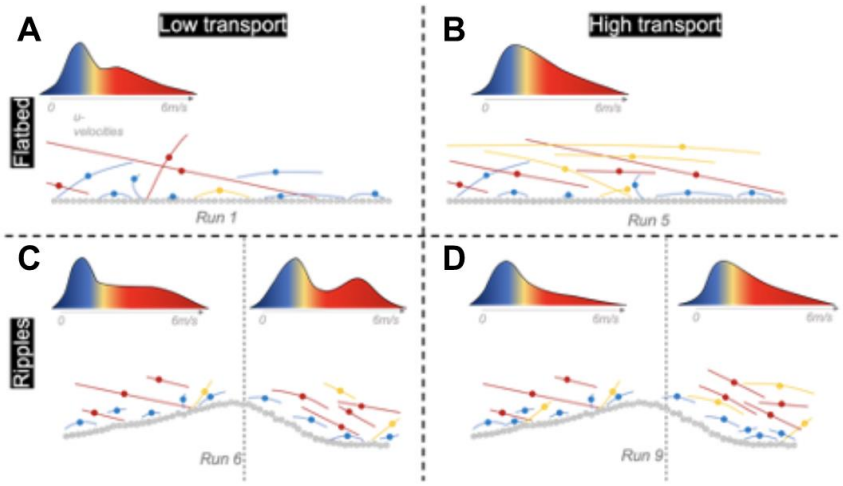

Figure 19: Conceptual diagram of observed changes in particle trajectories, concentrations, and velocities with wind speed and over flat and rippled beds.

There are multiple complex interactions and feedbacks between sand in transport, wind profile, and bedform morphology (Walker & Nickling, 2002). Our results provide new insights on inherent properties of the saltation cloud variability and flux, the momentum extraction by sand grains from the fluid and resultant particle velocity distributions, and links between ripples and modes of non-suspended sand transport.

Saltation Cloud Variability

It is well-recognized that natural saltation is intermittent rather than a continuous process (Shao, 2008), and many observations confirm that aeolian sediment transport is temporally and spatially variable (e.g., Butterfield, 1998; Sterk et al., 1998; Baas & Sherman, 2005; Davidson-Arnott et al., 2009; Bauer, B. O., & Davidson-Arnott, R. G., 2014; Sherman et al., 2018). One form of intermittent transport is characterized by periods when wind speeds drop below the threshold for sand transport, followed by strong intermittent gusts of wind that produce intense bursts and sand transport. The proportion of time that the system is active at a particular location can be represented by the intermittency parameter (γ_p) (Stout & Zobeck, 1997). An intermittency threshold wind speed ($U_{t\gamma}$) can also be calculated from the instantaneous wind speed data assuming that the fraction of time that the wind exceeds the threshold value (γ_t) be equal to the fraction of time that saltation occurs in the record (Davidson-Arnott et al., 2009).

The other form of intermittency concerns the non-uniform distribution of saltating grains revealed by high-frequency sampling (e.g., Sherman et al., 2018). Our results suggest that the overall saltation process leads to broader dispersion in grain counts than expected if the process was completely random. Figure 11 shows that the grain count histograms at higher transport rates deviate from a Poisson distribution. The distributions' variance increases more than the mean at the subsecond time scale as the sand transport and wind speed increase across runs (Table 4). Our results match well with the wind tunnel results of Wang et al. (2014). Greater variance than mean values suggests that intermittency is an inherent property of saltation, and it is not a completely random process. Fine-scale intermittency is separate from the discussion on temporal or spatial variability of saltation seen on beaches, or replicated in wind tunnels, with quantifiable fluctuations in wind speed or bed moisture. Other forcing processes (e.g., wind gusts on a beach, temporal/spatial variation in supply or moisture content) also cause intermittency but at larger scales (e.g., McKenna Neuman, 2004; Bauer et al., 2013; Swann et al., 2021). Our results suggest intermittency may be inherent to the saltation process itself at the subsecond time scale.

As Wang et al. (2014) point out, intermittent saltation seems to occur in all wind tunnel experiments, even when environmental variables are highly controlled. The Poisson distribution is commonly used for modeling discrete distributions and measures the probability of a given number of events happening in a specified time period. Events must be independent and random over time and the mean rate of occurrence is constant over time. Figures 10 and 11 and Table 4 show that our runs with higher wind speed and sand transport deviate from the Poisson distribution, which implies that saltation at higher sand transport rates is not random in terms of particle counts and that intermittency is an inherent property of the saltation process.

Understanding the driving mechanism(s) of saltation variability has important implications for improving sediment transport modeling and quantifications. The dominant theory assumes uniform and steady wind and saltation fields with “equilibrium” or “steady state” saltation (e.g., Owen, 1964; Anderson & Haff, 1988). However, our PTV saltation data do not support this for the highly controlled conditions of wind tunnel experiments. More experiments are still required to determine the potential role of turbulent structures and sand bed state in saltation cloud variability. Though the collisions among sand grains and turbulent structures near the bed are out of the scope of this current work, a complementary study explores this potential driving mechanism of saltation variability further.

Re-evaluating Bagnold’s Assumption of Particle Trajectories

We are not the first to re-evaluate Bagnold's (1941) assumption that mean particle velocities scales with shear velocity (e.g., Namikas, 2003; Kok et al., 2012). Understanding the vertical flux distribution is essential to accurate modeling and prediction of sand flux because the flux profile represents the integration of grain trajectories and, hence, sand mass moving across a surface in saltation. Thus, characterizing the distributions of ejection angles and speeds of grains in saltation or splashed from the bed by saltation impacts is key for accurate sand flux prediction (Ellis & Sherman, 2022). Several functions have been proposed to represent the decrease in particle concentrations away from the bed, such as power functions (e.g., Zingg, 1953; Stout & Zobeck, 1996), logarithmic functions (e.g., Butterfield, 1991; Greeley et al., 1996; Rasmussen &

Mikkelsen, 1998), and exponential decay functions (e.g., Greeley et al., 1996; Namikas, 2003; Liu & Dong, 2004; Dong et al., 2006).

Our results show that, as wind speed increases, the concentration of particles increases, yet the normalized volumetric flux profiles remain consistent. With most transport near the bed, our normalized volumetric profiles follow the same exponential decay rate. Following the method of Ellis et al. (2009), our normalized volumetric mass flux profiles for all runs (flat and rippled beds) best conform to an exponential fit with an R^2 value of 0.9 (Fig. 20).

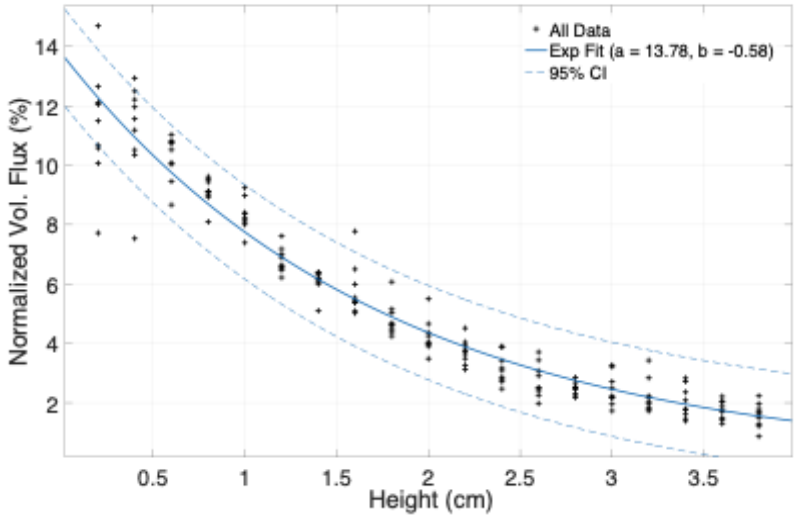

Figure 20: Normalized volumetric flux profiles for all runs 1-9 (flat and rippled beds) with an exponential fit and 95% confidence interval (CI).

Given that all our normalized volumetric profiles for various wind speeds and over flat and rippled beds follow a similar exponential decay, this indicates that the grains, on average, spend about the same proportion of their travel time at any given height independent of wind speed or bed configuration. A relationship between the flux profile and wind conditions has important implications for predicting mean transport rates. If a characteristic flux profile can be determined and linked to corresponding sediment and wind characteristics, it could provide another basis for predicting mean transport rates by integrating the flux profile from the sand surface to the top of the saltation layer instead of using on the common sand transport model derived from relationships to shear velocity (Sørensen, 1985).

While our mean and median particle u-velocities increase with height above the bed, they do not appear to increase with wind speed (Fig. 14). Namikas's (2003) results also suggest that the average launch speed of saltating grains is largely, if not entirely, independent of shear velocity. Similar to our normalized flux profiles, this directly contradicts the fundamental assumption of Bagnold (1941) that sand grain speeds and, hence, volumes in saltation scale directly with shear velocity.

In summary, both our volumetric flux profiles and mean particle velocity results support an interesting implication suggested by Namikas (2003). Constant particle velocities imply that additional momentum extracted by the grains from the fluid is almost entirely transferred to the bed. Thus, the increase in rates of transport associated with higher wind and shear velocities should be related to the ejection of additional grains from impacts. The scope of this paper is unable to test this hypothesis directly, but future work with different analysis methods aims to address this topic.

Re-examining the Role of Shear Velocity on Saltation

Although the previous section might seem to completely diminish the role of shear velocity, examining particle velocity distributions beyond the mean and median reveals interesting characteristics that imply that sand particle trajectories are not completely unaffected by shear velocity. For instance, in Figures 15-17, particle u-velocity distributions shift from bimodal to unimodal with increasing sand concentration. Also, Table 5 shows kurtosis values for u-velocities near the bed increase with wind speed, suggesting more “peaked-ness” and a single mode for the distributions at higher wind speeds. Our findings of bimodality at lower transport rates correspond with Jiang et al. (2022), who show an even stronger bimodality in liftoff distributions for lower speeds. Focusing solely on the ascending particles (lift-off velocity) within the transport layer (<1 cm) from our flat bed runs (1-5), Figure 21 shows the u- and v-velocity distributions. These data (Fig. 21 A&B) compare favorably with the results of Jiang et al. (2022: Figs. 4&5 and Supplemental Figures).

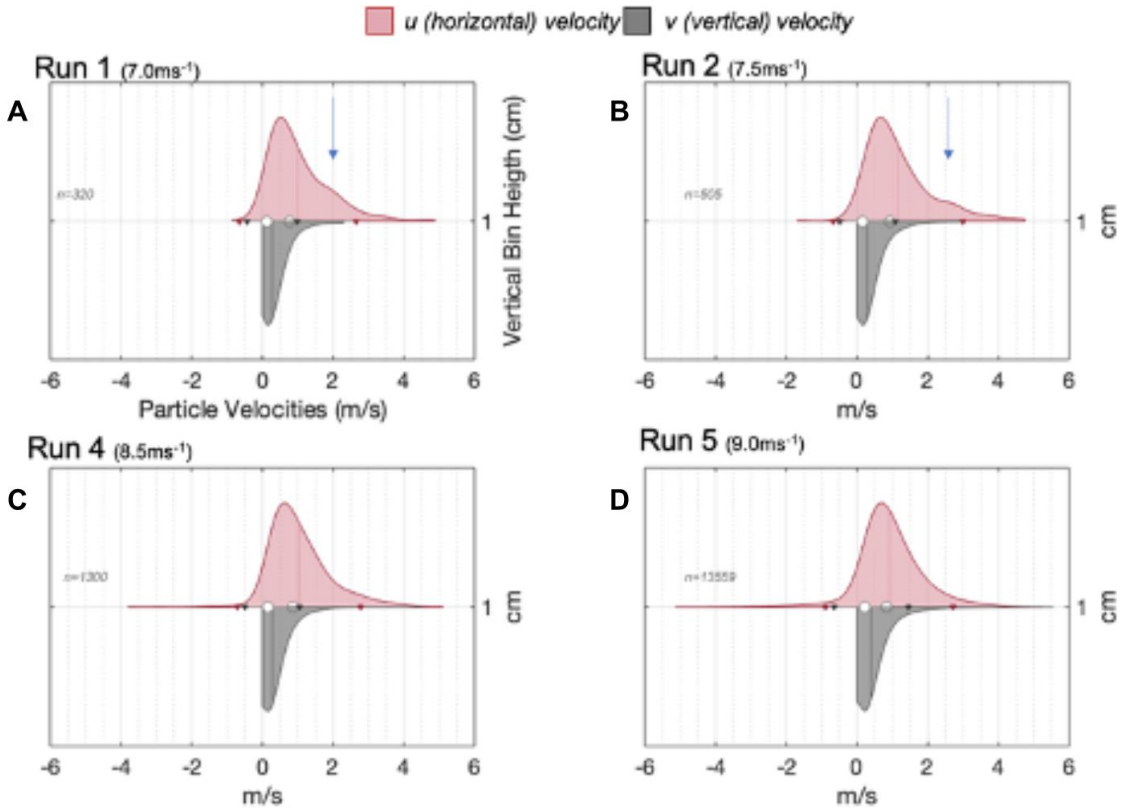

Figure 21: Violin plots of the horizontal and vertical velocity distributions for the flat bed runs 1-5 limited to ascending particles within the transport layer. The top/red violin plots are the u-velocities. The bottom/black violin plots are the v-velocities. The number of tracks in the sample is indicated on the left. The median values are notated by the white dot. The mean values are notated by the vertical line. The 2-sigma ranges are notated by the triangles. The blue arrows highlight multiple modes.

Figure 21 A&B shows the velocity distribution for the two slowest wind speed runs (1 and 2), and the arrows highlight a secondary peak in the histograms at 2.0 and 2.5 ms^{-1}. This suggests a bimodality in the u-velocity distributions, which matches Jiang et al. (2022) results. Yet, these runs (Fig. 21 A&B) had the lowest wind speed and the fewest sand grains in transport. Comparing runs 4 and 5 in Figure 21 C&D, we see the multi-modal distribution shift to a single-mode distribution, which we also saw in Figure 15. Jiang et al. (2022) only collected data at lower wind speeds and sand transport rates, comparable to our runs 1 and 2. The observed bimodality

in particle speeds at lower speeds most likely reflects two different modes of transport - faster particles in saltation and slower particles in creep or reptation. However, as wind speed and sand transport increase, the distribution shape becomes less bimodal. Recall Figure 1 highlights the dominant modes of non-suspended transport. It is common to think of grains moving as saltons or as creep/reptation. Our results suggest that grains move in a range of trajectories, which have saltation and creep as endmembers but not always clear, distinct modes of transport.

Our results support the implication that particle trajectories are influenced by shear velocity without changing mean particle velocities. Particles that leave the bed extract momentum from the fluid, yet, additional energy extracted by these grains from a more energetic wind field (higher shear velocities) is also eventually transferred to the bed. This serves to maintain near-bed mean particle velocities with increasing sand transport and smooth the distribution of particle velocities throughout the cloud. Namikas (2003) suggests that if the bed response mimics a plastic limit, the impact energy in excess of this limit could be used to eject more grains at a range of velocities. This perspective conflicts with common conceptual models, which show saltation, reptation, and creep as separate modes of transport. Our results suggest there is a smoother continuum between saltation and reptation as shear stress increases.

Interactions Between Ripples and the Saltation Cloud

Impact ripples quickly develop once saltation begins. The dominant theory of their formation suggests that the instabilities of grain impact and asymmetry of the bed lead to ripples rather than an aerodynamic or hydrodynamic instability associated with aeolian dunes and fluvial ripples (Anderson, 1987). Though there is some disagreement in the literature, it is proposed that particle trajectories involved in splash events differ between rippled beds and flat surfaces (Gordon & McKenna Neuman, 2011). It is unclear, however, if these differences are due to impacting particle trajectories relative to the surface, the effect of shadowing caused by the ripple morphology, or a combination of the two. While splash dynamics of individual particle-bed interactions are beyond the scope of this work, our observations of near-bed particle trajectories across ripples and flat beds highlight feedbacks between bedforms and the saltation cloud. For

instance, Figure 22 shows resultant vectors of particle trajectories in the transport layer (i.e., < 1 cm) for runs 5 and 9 (U=~9.0 ms^{-1}) (see also Fig. 18 for responses within 2 mm of the bed). For all datasets, the mean velocity increases with height, as expected, but the resultant vectors deviate the most near the bed. As particles travel away from the bed, they experience more fluid momentum, partly explaining why particle vectors over the ripple stoss and lee, and flat bed are most similar towards the top of the transport layer. Vectors over the ripple stoss slope are always more upward than the flat bed and ripple lee vectors, and they always have a smaller horizontal component. This observation suggests a higher concentration of creeping particles on the stoss.

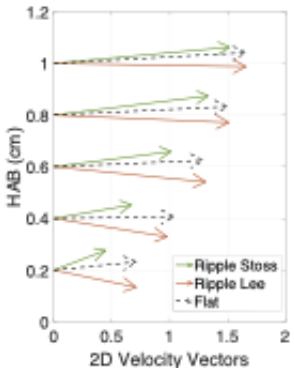

Figure 22: Resultant particle trajectory vectors in the transport zone derived from mean horizontal and vertical velocities for runs 5 (flat bed) and 9 (ripples). Note the significant difference in particle vectors' magnitudes and directions on the stoss and lee of the ripple compared to those over the flat bed and nearest to the bed.

Additionally, these results support previous findings that splash event concentrations differ with bed morphology (Gordan & McKenna Neuman, 2011). To have additional, slow-moving, ejected particles in motion requires more impacts of higher-energy saltons. These impacts can occur more frequently on the stoss, where there is no shadow effect, as in the lee, but also due to the positive slope of the stoss, which increases the impact angle and the potential for more newly ejected particles (Mitha et al., 1986; Anderson, 1987; Rice et al., 1996a; Beladjine et al., 2007).

On the lee side of the ripple, Fig. 22 shows a downward trajectory with a larger u-velocity component, which suggests faster-moving, downward grains. These results also support the idea that saltating grains cannot enter the lee region unless they have a steeper angle of descent to overcome the shadowing effect of the ripple morphology (Gordon & McKenna Neuman, 2011). The particles travel above the lee but probably do not hit the bed until the trough region further downwind. This is further supported by Figure 17. At the highest wind speed (Fig. 17c), we see multiple modes in the velocity distributions in the troughs. The multi-modality suggests that saltons and creep/reptating are present, possibly as newly ejected particles resulting from salton impacting the bed.

A ripple dynamics theory suggests ejection flux drives bedform migration rate. Our results indicate that particle trajectories vary across and differ between rippled and flat beds. Both impacting trajectory and shadowing play a role in the interactions between sediment transport and ripple forms. Figure 17 allowed us to compare particle u-velocity and grain counts across the ripple in a spatially continuous manner. While we see evidence for feedbacks between modes of sand transport trajectories and ripple aspects, incorporating grain size and splash dynamics (impacts and associated ejecta) into a bi- or multivariate analysis could directly address ripple dynamics theory. Yet, this is outside our current scope and further analysis is needed to confirm.

Conclusions

Experimental observation of the saltation cloud at high transport rates and with natural ripple development has been difficult because of lighting issues, camera frame rate and resolution requirements, problems with surface detection, and particle detection and trajectory identification error. In this chapter, the image-based PTV, TrackMate, successfully detected sand grains and produced trajectories across a range of wind speeds (7.0 to 8.7 ms^{-1}) and within 0.5 cm of flat and rippled bed surfaces.

Application of this free, open-source algorithm (name) in a wind tunnel investigation of the horizontal and vertical components of trajectories within a saturated saltation cloud reveals that, while mean particle velocities do not scale with wind speed, velocity distributions do change

(smooth?) with increasing wind speed and sand transport and across microtopography. Resultant changes in the modes of non-suspended transport were also observed. Distinctions between saltating particles and those in reptation/creep become less clear as transport increases.

Ripples are a ubiquitous feature of sedimentary environments. Yet, empirical data on particle velocities over rippled beds has been limited. Our results suggest that there are feedbacks between ripple development and the modes and velocities of particles in transport in the saltation cloud. Near-bed particle trajectories vary between flat and rippled beds, as well as across ripple forms. Distributions of particle velocities from rippled runs suggest that microtopography influences the conversion of horizontal to vertical momentum during bed impacts, critical for sustaining saltation. Also, ripples influence the location of salton impacts and concentration of the associated reptation/creep for impacts, which potentially drive ripple migration.

Limitations with common aeolian sand transport models that tend to overestimate sand flux, may be in part related to Bagnold's assumptions of a particle velocity cubic scaling relationship with shear velocity. Given how well our normalized flux data, and others, follow an exponential decay, pursuing models based on characteristic flux profile relationships to corresponding sediment and wind characteristics may produce more accurate sand transport predictions than current common shear velocity models.

Here, we highlight mean particle velocity is independent of wind speed but changes in overall particle velocity distribution due to interactions between sand transport, wind, and bedforms. Such observations have implications for the parameterization of saltation models, as well as for understanding the inception and growth of aeolian bedforms.

Supplemental Figures

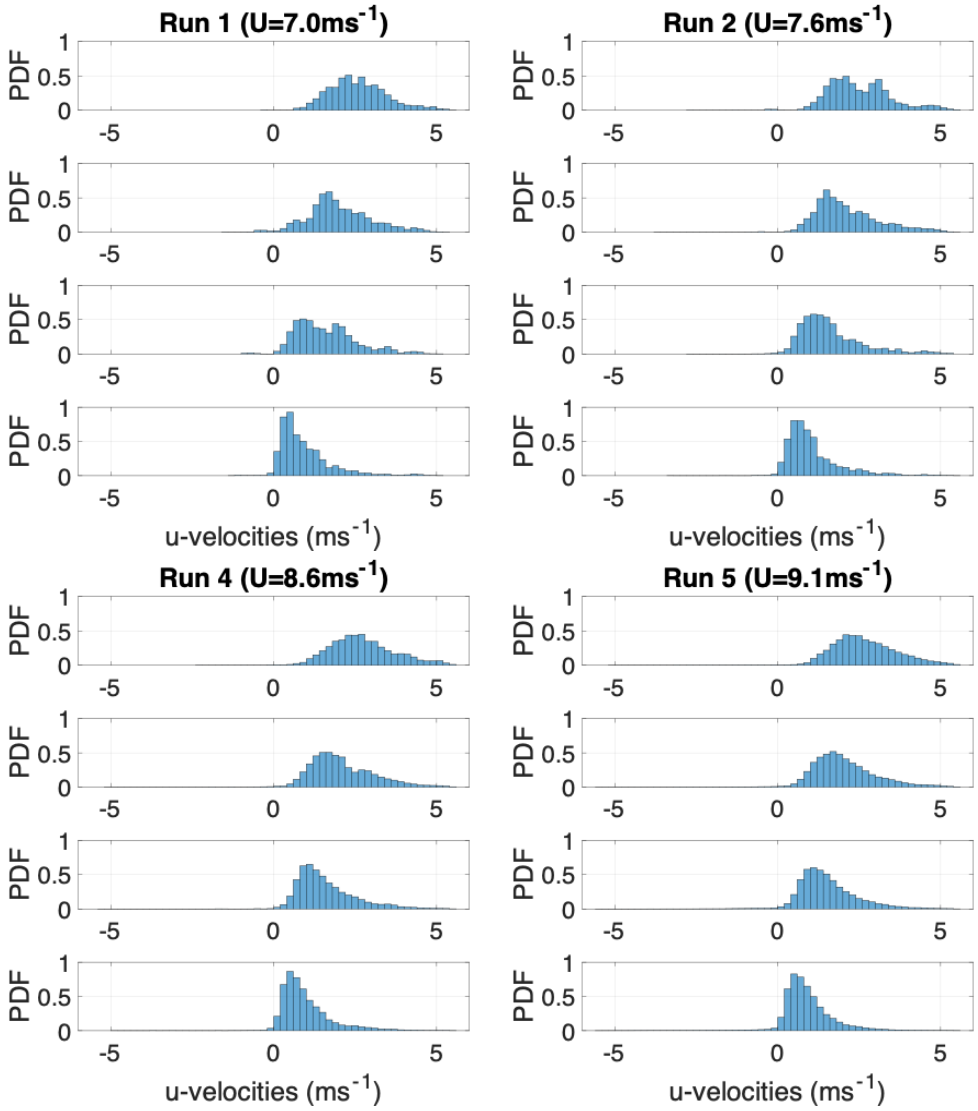

Figure 23: Horizontal velocities runs 1-5. Trajectories have been separated into the same 4 vertical heights as Figure 14.

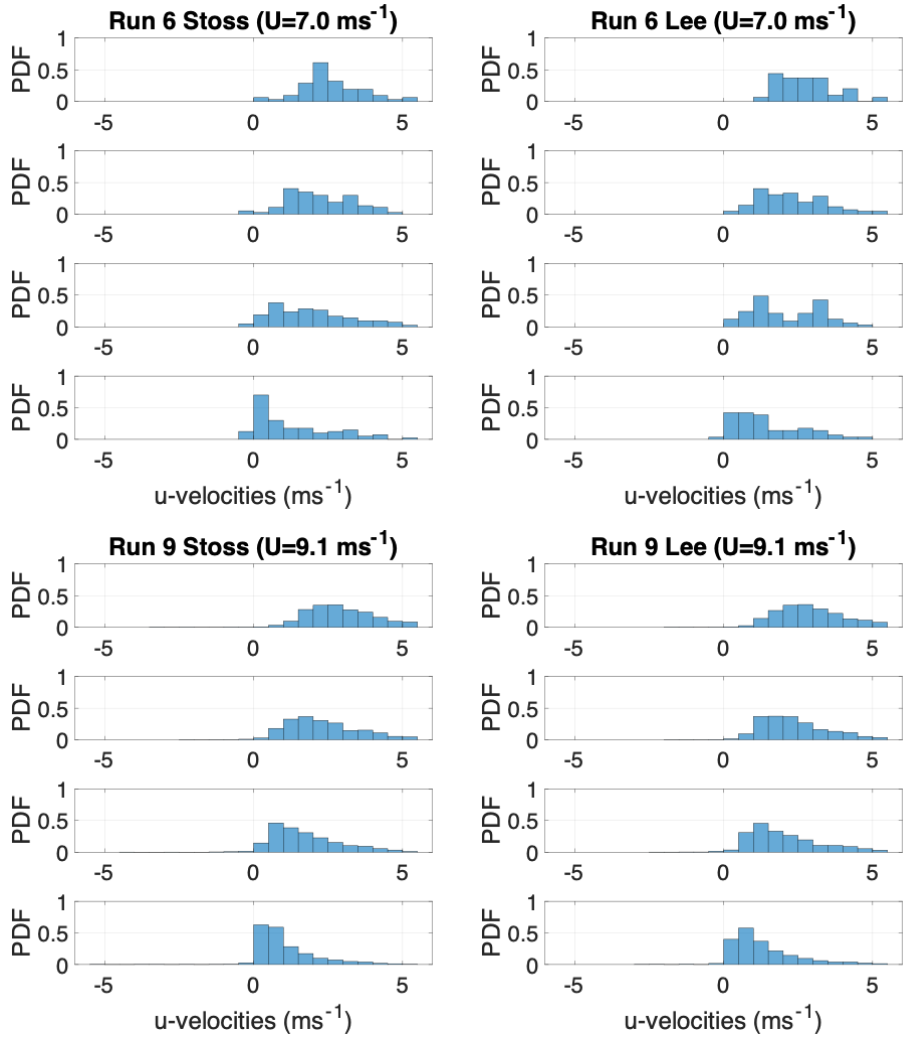

Figure 24: Horizontal velocities runs 6 and 9. Data are separated by stoss and lee ripple locations. Trajectories have been separated into the same 4 vertical heights as Figures 15 &16.

CHARACTERISTICS OF SPLASH EVENTS AND THE INFLUENCE OF RIPPLES

Introduction

Aeolian (wind-blown) sand transport processes play an important role in the geomorphology of Earth and extra-terrestrial environments (Bagnold, 1941; Lorenz et al., 2006; Kok et al., 2012; Telfer et al., 2018). Aeolian sand transport emits dust aerosols, propagates land degradation and desertification, and creates ripples and dunes (Sherman et al., 2018; Zhang et al., 2021). The ability to accurately quantify the effects of aeolian processes has important implications for combating soil degradation and loss of agricultural productivity, health concerns for people living in areas affected by wind-blown sand and dust, impacts of climate change, and infrastructure longevity (Ravi et al., 2011; Evett et al., 2018). Understanding, measuring, and modeling aeolian transport has profound implications for our response to the compounding natural hazards initiated or sustained by wind-blown sand.

Aeolian sand transport begins when the wind speed exceeds a velocity threshold for sand-sized particles (i.e., 0.063 to 2 mm). Above this threshold, sediment is mobilized into multiple modes of transport, each traveling in different trajectories and interacting with the bed (surface of stationary sand) differently. Bagnold (1941) was the first to identify and describe these modes of wind-blown sand transport and identified saltation as the primary mode of aeolian transport. Additional modes of sand transport include creep, reptation, and suspension, which vary depending on grain size and the height above the bed (Fig. 1). Saltating grains travel in a sequence of ballistic trajectories and, when colliding back onto the surface, produce a splash of new ejected grains. Once saltation is initiated, the number of saltating grains increases exponentially due to the multiplicative process of the splash events until the cloud reaches saturation limits (Anderson et al., 1991).

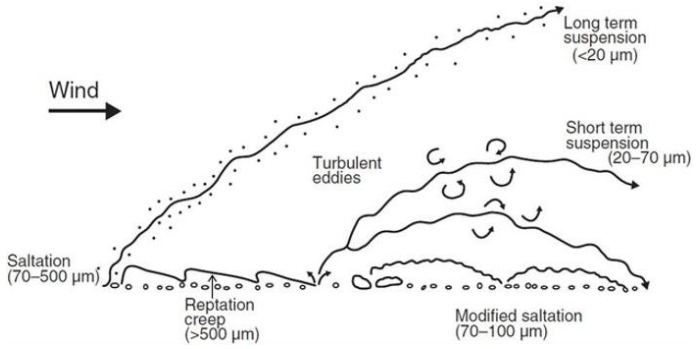

Figure 1: Modes of aeolian sediment transport (Nickling & Neuman, 2009; Tsoar & Pye, 1987). This paper uses reptation and creep interchangeably.

Saltation is thought to be sustained by the combination of fluid forces and particle-bed momentum exchanges during impact (Werner & Haff, 1988). An impacting salton creates a "splash event." Figure 2 outlines a splash event and the three types of particle trajectories we focus on in this chapter. The splash process includes an incoming salton particle on its downward trajectory just before the collision with the bed, its rebound post-collision, and newly ejected particles (ejecta) resulting from the impact of the salton with the bed. The splash process is a very efficient and essential mechanism in aeolian sand transport. Understanding the characteristics of particle trajectories involved in splash events is important to modeling the saltation cloud, predicting sand transport rates, and further understanding aeolian sand transport processes. An accurate, empirically driven description of this process is crucial for theoretical and numerical approaches (Valance et al., 2015).

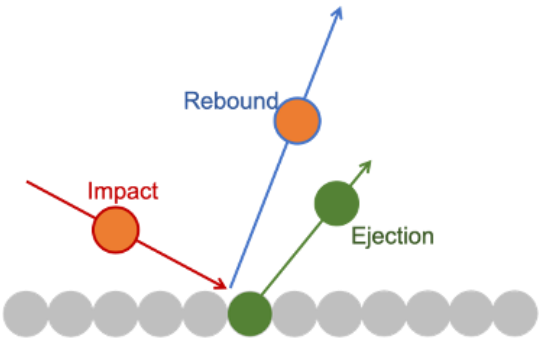

Figure 2: The splash event includes an incoming saltating particle (salton) that hits and bounces off the bed (orange particle). The impact of the salton with the bed is shown by the red vector, and the rebound of the same salton is shown by the blue vector. The newly ejected grain(s) is the green particle and vector.

To gain empirically driven descriptions of particle splash, several studies have attempted to measure sand particles near the surface using high-speed imaging with manual tracking or Particle Tracking Velocimetry (PTV). Progress has been limited because of the difficulty of making reliable measurements within the transport layer (<1 cm above the bed). For example, Figure 3 shows previous lighting difficulties and surface detection near the bed. Consequently, the splash process has been analyzed under somewhat artificial conditions. These include low transport rates (e.g., Willettts & Rice, 1989; Rice et al., 1996; Gordon & Neuman, 2011), experiments involving propelling a single particle or sand grain into a static bed of similar particles (Mitha et al., 1986; e.g., Werner & Haff, 1988; Rioual et al., 2000; Beladjine et al., 2007; Gordon & Neuman, 2011), or studies without natural aeolian ripples (e.g., Willetts & Rice, 1989). It remains challenging to separate discrete particle trajectories within a dense cloud of particles moving within millimeters of the bed surface. PTV's ability to track a particle's displacement and velocity throughout a portion of its ballistic trajectory makes it a desirable method for obtaining information about saltation dynamics (O'Brien & McKenna Neuman, 2016). Though manual tracking is time intensive, it provides increased accuracy in the near-bed region where particle interactions and trajectories quickly change, making automated methods ineffective. This study applies technology improvements in high-speed imaging with manual tracking methods to fill gaps

in the empirical datasets on splash dynamics and improve our understanding of particle-bed interactions involved in aeolian sediment transport processes.

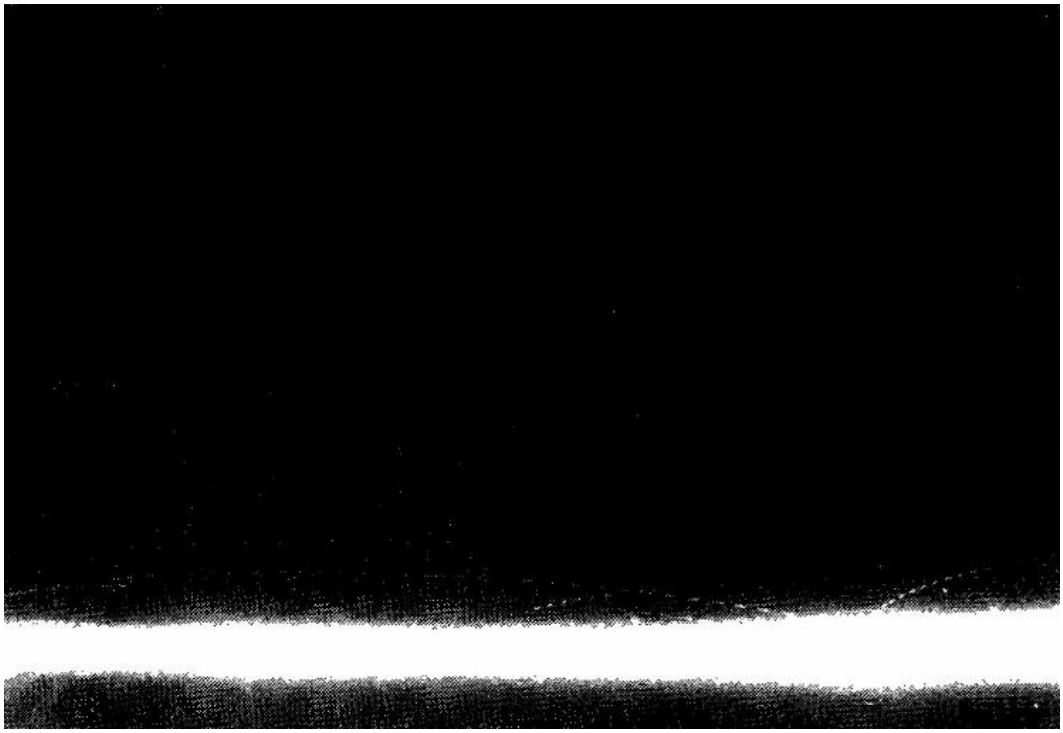

Figure 3: Trajectory photographs for 188~m median diameter sand particles with an interrupted light source (Hunt & Nalpanis, 1985: Fig. 4). Note that high reflectance at the bed increases the difficulty of particle tracking

Background

Saltation can be examined from two frames of reference: emergent characteristics of the saltation cloud or the trajectories of individual grains (Dong et al., 1995). The first approach focuses on the resultant characteristics of a saltation cloud, such as the variation in saltation cloud height, saltation flux, and mean particle velocity. The second approach focuses on the behavior of individual particles during a portion of their trajectory, which is the focus of this study. Specifically, we quantify splash dynamics via particle trajectory characteristics and the frequency of rebound and ejecta particles.

Since the seminal work of R.A. Bagnold (1941), there have been several detailed laboratory studies (Mitha et al., 1986; Werner & Haff, 1988; Willets & Rice, 1989; e.g., Dong et al., 1995; Rioual et al., 2000; Beladjine et al., 2007; Gordon & Neuman, 2011), field observations (e.g., Namikas, 2003), and numerical approaches (Anderson, 1987; e.g., Werner, 1990; Oger et al., 2005; Crassous et al., 2007) that have refined our understanding of splash dynamics. Table 1 summarizes some of the key previous findings. From that body of work, statistics on the splash process were derived, albeit with some discrepancy between experimental results. On average, saltating grains impact the bed at angles ranging from 8° to 15°, then rebound with a smaller velocity and at angles between 20° to 40° (Willets & Rice, 1986; Valance et al., 2015). Mitha et al. (1986), Anderson (1987), and Rice et al. (1996a) found an increase in newly ejected particles with steeper impact angles, while McEwan et al. (1992) found that shallow impacts tended to eject more particles. Thus, conflicting results suggest that uncertainties in the quantification and interpretation of the splash process remain.

Table 1: Modified from Willetts and Rice (1986) Table 2 to include Gordon & McKenna Neuman (2011). Summarizes the previous experimental results on impact and rebound velocity and angle, where u_* is the shear velocity (ms-1), v_i and v_r are the impact and rebound velocity, θ_i and θ_r are the impact and rebound angles, and n_{ej} is the mean number of ejecta per splash. The experiment column describes whether grains move within a saltation cloud or are fired individually at the bed (*Rebound and ejecta are combined).

		Willetts & Rice		White & Schultz		Hunt and Nalpanis		Gordon & Neuman			
Experiment		Collision		Saltation		Saltation		Saltation			
Material		Quartz Sand		Glass Spheres		Irregular Sand		Quartz Sand, Ripples		Acrylic	
size (μm)	355-600	250-355	150-250	350-710	150-300	150-300	90-150	303	303	303	192
u_* (cms^{-1})	39	39	39	39.6	20	20.5	18	22	28	29	16
v_i (cms^{-1})	360	356	394	161	150	140	130	64	59	122	136
θ_i (°)	12.7	11.7	9.6	13.9	14.0	13.0	11.0	16.7	11.0	12.3	8.1
v_r (cms^{-1})	225	216	240	69	76	88	81	31	30	48	51
θ_r (°)	21.3	24.9	33.4	49.9	41.0	34.0	35.0	33.5	32.5	44.7	26.6
v_r/v_i	0.626	0.609	0.607	0.430	0.507	0.629	0.623	0.6	0.62	0.55	0.51
θ_r/θ_i	2.01	2.73	4.21	3.59	2.93	2.62	3.18	2.01	2.95	3.63	3.28
n_{ej}	3.1	1.5	0.9	-	-	-	-	1.1*	1.2*	1.2*	1.4*

There has been great progress in models of saltation (e.g., Creyssels et al., 2009; Kang and Liu, 2010). In most numerical models, the stochastic behavior of particle trajectories during aeolian transport is encoded in a statistical description of the main trajectory parameters, and a splash function is included to model the ejection of new particles after grain-bed collisions (Willetts and Rice, 1986; Werner and Haff, 1988). Empirical data for validating splash functions are primarily from physical models with flat, horizontal beds and low sand transport rates (Gordon and Neuman, 2011). Thus, new empirical data will provide great benefit to numerical modeling efforts.

More recent progress has continued to resolve the aforementioned limitations. While early studies focused on particle splash over flat or smoothly sloping surfaces (Willetts & Rice, 1989; McEwan et al., 1992), they neglected to characterize saltation over more typical rippled bed configurations. As ripples are a product of aeolian saltation in natural boundary layers, it is critical to investigate aeolian sand transport in relation to bedform development. Impact ripples are decimeter-scale transverse bedforms that quickly develop once saltation begins and migrate on the surface of aeolian dunes by maintaining a nearly fixed profile in the direction orthogonal to the wind (Bagnold, 1941). Aeolian impact ripples form as reptating grains accumulate into small heaps and grow (Anderson, 1987). As saltating grains impact obliquely onto the heaps, the downwind side of a heap is less likely to be impacted during saltation, thus leading to sand accumulation and ripple growth (Fig. 4).

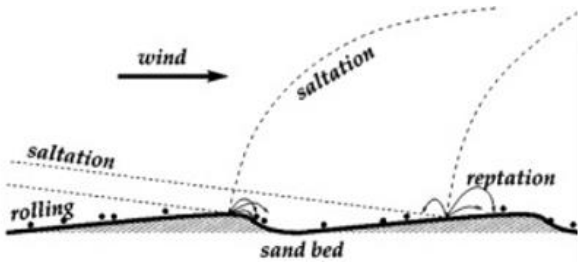

Figure 4: Sketch of saltation and reptation trajectories on wind-blown impact ripples. Modified after Prigozhin L (1999).

Recent studies have incorporated bedforms and explored changes in saltation impact angles (e.g., Beladjine et al., 2007; Gordon & Neuman, 2011). The few experiments that have explored splash characteristics across natural ripples with saltation suggest that splash dynamics differ with bedforms. Willetts and Rice (1989) measured particle collisions along varied slopes by tilting a narrow strip of sand particles up to 15°. Their results suggested that rebound angles are larger than impact angles and that particles on the stoss side are more likely to creep towards the crest than on the lee side. Gordon & McKenna Neuman's (2009) results showed differences in splash dynamics between a positively sloped stoss and a negatively sloped lee face. The report higher particle impact counts and ejection rates on the windward-facing stoss slopes. The PVC bead collision experiments by Beladjine et al. (2007) manipulated impact angles by changing the particle trajectories rather than directly adding ripples. Their results showed a negative relationship between impacting angle and the rebound angle. Due to differences in experimental design, data resolution, and analytical approaches, questions remain on the influence of shadowing effects and changes in impact angle relative to the surface on splash dynamics.

As above, previous studies have observed particle motions within the saltation cloud and near the bed using various instrumentation systems (Willetts and Rice, 1986, 1989; Nalpanis et al., 1993; Rice et al., 1995, 1996 a, b; Rice and McEwan, 2001; Wang et al., 2008, Gordon and Neuman, 2011). Recent advancements in doppler anemometry (LDA), high-speed (HS) imaging, and particle tracking velocimetry (PTV) have provided researchers with increased measurement capabilities. LDA measurements are simpler and faster to obtain and process than PTV image

analysis. LDA validation rates can be low, however, for sand-sized particles moving in dense clouds, and this becomes increasingly problematic within several millimeters of the bed surface where the bulk of sand transport occurs. Particle facets and spin also can give rise to spurious measurements, and LDA cannot obtain information concerning the number of ejecta and energy partitioning in a given collision (Rasmussen and Sorensen, 2008).

PTV systems also have tradeoffs. The image resolution must be high enough to provide accurate particle trajectory information and capture the entire collision in the image sequence. The pulse frequency must be high enough that multiple pulses of a fast-moving impactor particle can be seen. Laser sheet reflectance on the bed can also make tracking within millimeters of the surface difficult. Thus, continuously tracking grains pre- and post-impact within a saltation cloud during high transport rates is difficult. Gordon and Neuman (2011) studied particle splash using PTV measurements carried out along the wind-aligned axis of migrating aeolian ripples for lower wind speeds. However, they used an apparatus to fire single grains at the bed to model higher particle velocities and transport rates. Lastly, it is difficult to associate ejecta with a particular splash event in an automated method with multiple splash events occurring nearby. Though great progress on PTV has been shown, issues remain with its application on near-bed particle trajectories within a dense saltation cloud. Thus, we used HS photography and manual tracking to collect data to study the characteristics of the impact, rebound, and ejecta particles of splash events. Manually tracking is time-consuming but provides the best resolution of all the variables of interest to better understand splash dynamics with increasing wind speed and bedforms.

Objectives

This work aims to resolve discrepancies in splash dynamics to progress aeolian sand transport theory and to expand empirical datasets required as input for and validation of numerical models. We collected HS imagery of splash events across a range of wind speeds, including high transport rates, with ripple bed development, natural sand, and fully developed saltation. This work is the second step in a three-part experiment on aeolian sand transport processes. Our results here focus on quantifying impact, rebound, and ejecta velocities and

angles, the coefficient of restitution, and distributions of ejecta and rebound counts across various wind speeds and over flat and rippled bed surfaces. Lastly, we provide insight into the influence of ripple slope (stoss vs. lee), which informs potential shadowing effects on splash event mechanics.

Methods

Wind Tunnel Facility and Instrumentation

A series of wind tunnel experiments were conducted in the Arizona State University Wind Tunnel (ASUWT), a 12.2 m long, 0.9 m high, and 1 m wide near-surface boundary-layer simulation tunnel with an open-loop suction design, Figure 5. Operating under ambient temperature and pressure conditions, the tunnel can produce and maintain wind speeds up to 30 m s^{-1}. Air is pulled into the tunnel by a large fan mounted in the downwind section of the tunnel (Fig. 5). An inlet screen smooths and straightens the airflow as it enters (Fig. 5), and an array of roughness elements on the floor of the tunnel trip the incoming airflow to initiate a shear. The tunnel's bed is separated into two sections. The upwind half (0-5 m) has a static bed roughened with immobilized (glued) sand. The downwind half (5-10 m) has a 5 cm deep active sand bed.

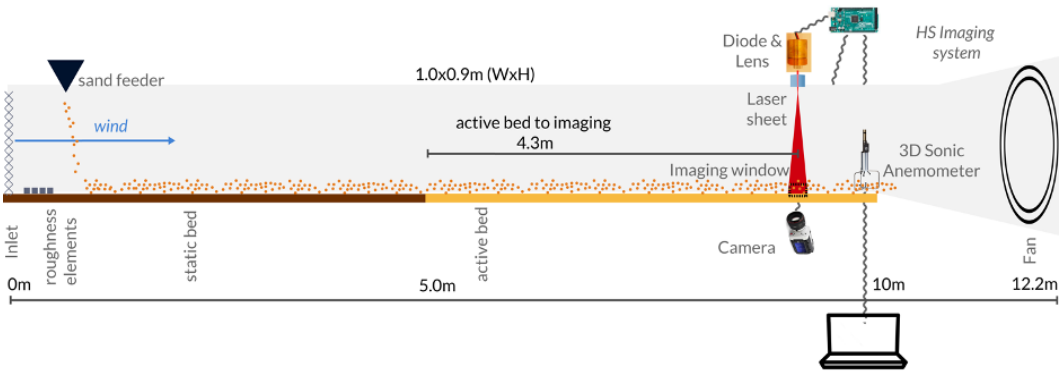

Figure 5: ASUWT with imaging system and 3D sonic anemometer.

For all experiments, we used natural, unimodal, well-sorted, medium sand with a D_{50} of 456 μm and standard deviation of 1.131 μm. 0.5 cm of sand filled the active section and was glued on the floor of the static, upwind section. Additionally, following the methods of O'Brien &

McKenna Neuman (2012), airflow was seeded with the same sand from a hopper positioned 1 m downwind of the inlet to initiate the development of saltation within the upwind sections of the tunnel and, thereby, extend the length of the test bed over in which the flow was saturated with particles.

All measurements were taken in the downwind, active bed section, which is enclosed with plexiglass doors for imaging and access to instrumentation. Downwind 9.5 m from the inlet, a side-mounted HS camera (Phantom Miro 341[1]) captured sand particle motions in the streamwise and vertical directions. Image dimensions were 1024x768 pixels, and the spatial resolution was 168 pixels = 1 cm. Images were collected at 2353 frames per second. The sampling period was selected to balance data storage and resolution. Due to imaging speed and camera storage limitations, the number of images recorded in a single run was 10,692 images over 4.5 seconds. To illuminate particles moving through the imaging window, a laser sheet was created using a 7-watt laser diode (nubm44-v2 450nm) and a 5-degree Powell Lens (Laserline Optics). The sheet covered the entire length and height of the image window. We measured the laser sheet width at 0.2 cm using a ruler but estimated its effective illumination width to be 0.3 cm due to scattering at the bed. An Arduino board was used to synchronize the system. The program was based on an 850 µs cycle. The camera and laser received two activation pulses per cycle resulting in one image every 425 µs over a period of 4.5 seconds.

An RM Young Ultrasonic Anemometer Model 81000 3D sonic anemometer was located downwind of the imaging system and collected wind velocity measurements during all runs. The sonic anemometer was mounted upside down so that observations could be collected close to the surface; the center of the measurement area was 15 cm above the bed. During all experiments, the sonic collected u, v, and w velocity fluctuations at 32 Hz. Time stamps were used to correlate the 3D velocity fluctuations with high-speed imagery.

Experimental Design

Table 2 summarizes the eight different experimental runs. Wind tunnel experiments can be sensitive to variations in ambient temperature and humidity (McKenna Neuman, 2004),

particularly in an open circuit tunnel that draws in outside air. Individual runs were conducted on May 25th, 2021 and June 2nd, 2021. There was minimal temperature and humidity variation between runs: the outdoor temperature and humidity ranged from 91-95°F and 7-8% on May 25th and 105-107°F and 10-11% on June 2nd. The experiments were conducted across freestream wind speeds ranging from 7.0 to 9 ms^{-1}. Our goal was to collect observations of particle motion just above the fluid threshold, where fewer grains are in motion to higher transport rates where particles saturate the boundary layer. To test the influence of bed configuration on saltation impact and ejecta response, we conducted experiments on both flat and rippled surfaces in the active bed section of the tunnel. Prior to data collection, the active bed section was either flattened manually or developed a rippled surface during a pre-run. This included the tunnel running at 9 ms^{-1} for ~10 min to allow saltation to generate impact ripples through the active bed section.

Table 2: Eight experimental runs that vary in wind speed and bed condition (flat or rippled surface).

Run	Day Bed Type	Duration (min)	Average U (ms^{-1})	Total Images	Splash events
1	2020/05/25 Flat bed	4.5	7.1	10,692	43
2		4.5	7.6	10,692	44
3*		2.4	8.1	5,532	35
4		4.5	8.6	10,692	50
5	2020/06/02 Rippled bed	4.5	7.0	10,692	27
6		4.5	7.6	10,692	52
7		4.5	8.2	10,692	53
8		4.5	8.7	10,692	51

Figure 6 provides an example of our experimental protocol during a typical run. Once the tunnel starts, sand is trickled into the feeder, which feeds saltation into the wind tunnel. After approximately 10 seconds, the boundary layer (BL) is developed. We wait an additional 10 s to confirm that the shear flow and saltation cloud have equilibrated. During the last 10 s (30 s from

the start of the tunnel), we used data from the 3D sonic anemometer to get 10 s wind velocity averages and collect 4.5 s of HS imagery.

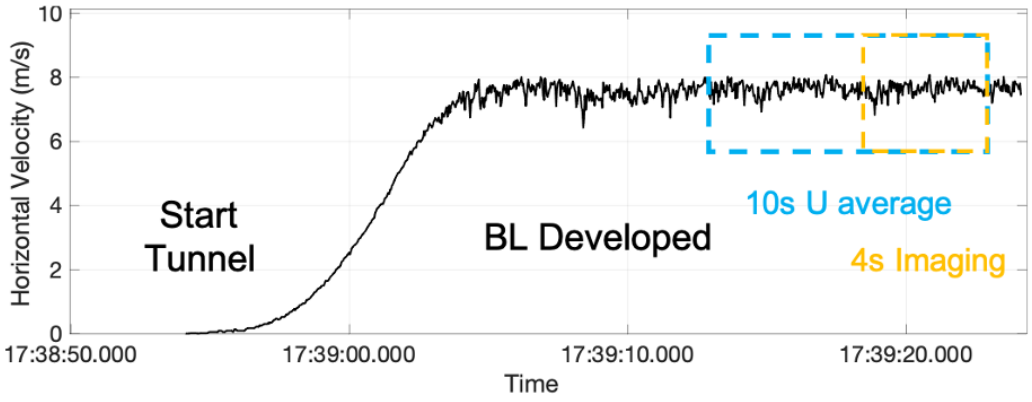

Figure 6: 3D sonic anemometer data from Run 6 (rippled bed, U_∞ = 7.6 ms^{-1}). Once the wind tunnel is turned on, it takes about 10-20s for the boundary layer and saltation clouds to develop and reach a steady state. We used 10s averages to calculate the U_∞ mean from the 3D anemometer (blue box) and collect imagery for ~4.5 seconds (yellow box).

Manual Sand Particle Tracking

Manual tracking was required to quantify the detailed splash characteristics. We aimed to digitize 50 splash events from each run with approximately 10,600 images. As described in the conceptual diagram (Fig. 2), a splash event starts with a salton impact (Track 1) and is then often followed by a rebound of the impacting particle (Track 2) and new ejecta (Track 3). As wind speed increases, the number of saltons and splash events increase. To determine saltation impact and resulting ejecta response over flat and rippled surfaces, we needed to track individual saltons and correlate those with the ejecta. Given the many grains in motion at higher wind speed runs, we could not manually digitize all splash events. Thus, we developed a digitization protocol to analyze splash mechanics from an unbiased selection of samples across each run.

Of the >10,600 images per run, we grouped images in sets of 100 and randomly ordered them. Then, we examined and digitized splash events in each group until we reached 50 events. If a splash event continued past the 100 images in the set, we would incorporate the necessary number of images to complete the digitization of the event. Randomly ordering groups of 100

images allowed us to sample unbiasedly across the 4.5 s sampling period. Table 2 provides the total number of digitized splash events for each run. For runs 1, 2, and 5, each resulted in 43, 44, and 27 digitized events due to fewer particles in motion at lower wind speeds. For run 3, only 35 splash events were observed due to fewer images. This dataset was for only 2.5 s (approximately half the time) due to data corruption issues during transfer.

We track the grains within 5-10 frames of the impact. Tracking criteria include: 1) the impacting salton trajectory must have crossed the reference line that runs 0.5 cm above the bed to help separate saltating vs. creeping particles) and 2) we must be able to see the impact and rebound of that particle, plus all the ejecta particles. If necessary, we expand the 5-10 frames post-impact for ejecta to incorporate their slower trajectory. Ejected particles are also labeled as to whether they reach the 0.5 cm reference line above the bed. The output includes details on the digitized grain motions, including track number, frame, and x (streamwise) and y (vertical) coordinates (Fig. 7). These data allowed us to calculate the grain's distance, velocity, and angle.

Track n	Frame n	X	Y
1	46	56	15
1	49	71	8
2	54	72	7
2	58	77	12
3	55	73	6
3	59	75	8

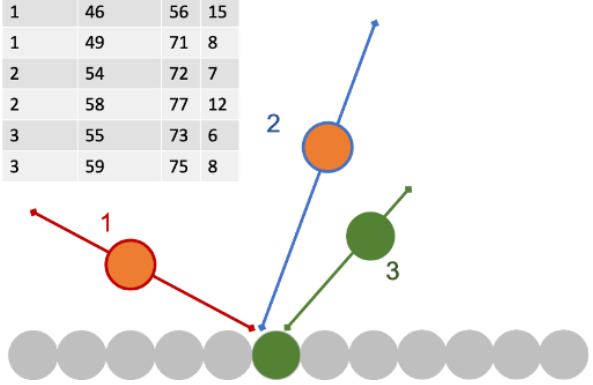

Figure 7: A modified Figure 2 showing digitization outputs from the manual tracking method. The distance, velocity and angle can be calculated from x, y coordinates from pre- and post-impact.

Particle Velocity and Angle

From x, y data coordinate pairs of particle locations captured between image frames in the streamwise and vertical dimensions, respectively, we calculated the 2D velocity (v) Eq. 1:

$$v_{i,r,e} = \frac{\sqrt{(x_{n+1} - x_n)^2 + (y_{n+1} - y_n)^2}}{(t_{n+1} - t_n)} \times (s_{ms}) \qquad \text{Eq (1)}$$

where s_{ms} is scale factor to convert from pixels/frame to ms^{-1} (0.14), t_n is the frame number for the current frame, t_{n+1} is the following frame, x_n is the x-pixel location for the current frame and x_{n+1} is the x-pixel location for the following frame, and, lastly, y_n is the y-pixel location for the current frame and y_{n+1} is the y-pixel location for the following frame. Impact characteristics are notated as v_i and θ_i, rebounds characteristics are notated as v_r and θ_r, and ejecta characteristics are notated as v_e and θ_e. We calculate the particle impact and rebound angles using Eq. 4.

$$\theta_{i,r,e} = tan\left(\frac{(y_{n+1} - y_n)}{(x_{n+1} - x_n)}\right) \qquad \text{Eq (2)}$$

Figure 8 shows the initial and terminal sides that create the enclosed angle (θ°). Note that impact particles are not measured from the standard position; the initial side is along the negative x-axis. Also, the flat and ripple bed splash event angles use the same x-axis. The ripple runs

include changes in local bed slope (i.e., stoss and lee), and the particle angles calculated using Eq. 3, were not adjusted for the local slope of the ripple features (Fig. 8). This allows for easier comparison of data across all runs.

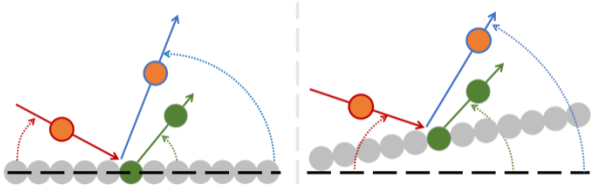

Figure 8: A modified Figure 2 showing the theta angle measurements for impact (red), rebound (blue), and ejecta particles (green). The right-side shows angle measurements for ripples still use the same (flat) x-axis.

Coefficient of Restitution

In addition to measuring particle velocity and angle, it is common to estimate a particle's retained energy after it collides with the bed. This is measured by the coefficient of restitution (CoR) defined in Equation 3:

$$\epsilon = \frac{v_r}{v_i} \qquad \text{Eq (3)}$$

CoR (ϵ) is the ratio of a particle's rebound velocity to its impact velocity. Though the CoR uses particle velocities to produce a value between 0-1, it provides information on the bed's plastic properties; ability to absorb momentum from impacting grains. As grain moves and ripples form, grain size sorting and grain packing occur. These bed characteristics influence the amount of energy a particle can retain after its collision with the bed. Thus, we utilize the CoR in addition to particle velocities and angles to explore splash dynamics across a range of wind speeds and bedforms.

Statistical Significance Testing

We use a two-sample t-test to compare the means of the various distributions of particle characteristics (i.e., impact, rebound, and ejecta velocities and angles and coefficient of restitution). This is a parametric test. Though many of the distributions are not normal, the t-test is

still appropriate since each sample group has more than 25 observations per group and no extreme outliers (Cessie et al., 2020). The calculation is show in Equation 4:

$$t = \frac{(\overline{x_1} - \overline{x_2}) - (\mu_1 - \mu_2)}{\sqrt{\frac{s_1^2}{n_1} + \frac{s_2^2}{n_2}}} \quad \text{Eq (4)}$$

where $\bar{X}_1$ is the mean of the first sample, $\bar{X}_2$ is the mean of the second sample, μ_1 is the mean of the first population, μ_2 is the mean of second population, s_1 is the standard deviation of the first sample, s_2 is the standard deviation of the second sample, n_1 is the size of the first sample, and n_2 is the size of the second sample. This type of hypothesis testing reports where the null hypothesis (the sample means are the same) can be rejected. If rejected, then the alternate hypothesis (the sample means are different) is possible.

Results

A total of 355 splash events were digitized and analyzed: 172 and 183 impacts for the flat bed and rippled bed runs, respectively. Our results include (1) the impact, rebound, and ejecta velocity distributions from our flat bed and, (2) from the rippled bed runs, (3) the distribution of angle trajectories from our flat bed runs, (4) differences in CoR values for splash events on a flat bed vs. rippled, (5) the newly ejected particle counts and probability, and (6) the influence of ripple slope. Overall, we find a limited influence of freestream velocity on mean particle velocities, but notable relationships appear between ripple aspect (local slope) and particle angles and impact. Tables 3 and 4 summarize splash event results for the flat bed (runs 1-4) and rippled bed (runs 5-8), respectively.

Table 3: Flat bed runs 1-4 splash event summary statistics.

		Run 1	Run 2	Run 3	Run 4
	U_∞ (ms^{-1})	7.1	7.6	8.1	8.6
v_{i_flat} (ms^{-1})	n_{i_flat}	43.0	44.0	35.0	50.0
	$\bar{x}$	2.6	1.9	2.1	2.0
	σ	1.4	1.1	1.5	1.1
θ_{i_flat} (°)	$\bar{x}$	17.5	18.8	19.1	14.4
	σ	8.1	6.7	7.5	7.5
v_{r_flat}	n_{r_flat}	43.0	44.0	35.0	50.0
	$\bar{x}$	1.5	1.3	1.3	1.4
	σ	0.9	1.0	0.9	0.8
θ_{r_flat}	$\bar{x}$	41.6	42.3	35.5	43.8
	σ	23.1	20.4	16.9	26.0
v_{e_flat}	total n_{e_flat}	47.0	16.0	16.0	34.0
	mean n_{e_flat}	1.1	0.4	0.5	0.7
	$\bar{x}$	0.27	0.34	0.30	0.32
	σ	0.17	0.29	0.22	0.18
θ_{e_flat}	$\bar{x}$	61.5	57.9	76.1	60.2
	σ	31.0	23.6	28.4	29.0
e_{flat}	$\bar{x}$	0.58	0.68	0.62	0.70

Table 4: Rippled bed runs 5-8 splash event summary statistics.

		Run 5	Run 6	Run 7	Run 8
	U_∞ (ms^{-1})	7.0	7.6	8.2	8.7
v_{i_ripple} (ms^{-1})	n_{i_ripple}	27	52	53	51
	$\bar{x}$	2.1	2.4	1.6	2.1
	σ	1.5	1.4	1.8	1.3
θ_{i_ripple} (°)	$\bar{x}$	16.1	20.0	20.7	17.1
	σ	8.2	8.8	7.6	9.2
v_{r_ripple}	n_{r_ripple}	27	52	53	51
	$\bar{x}$	1.2	1.3	1.0	1.2
	σ	0.9	0.8	0.9	0.8
θ_{r_ripple}	$\bar{x}$	44.1	52.8	44.7	47.1
	σ	20.0	31.6	28.4	23.0
v_{e_ripple}	total n_{e_ripple}	23	36	17	43
	mean n_{e_ripple}	0.85	0.69	0.32	0.84
	$\bar{x}$	0.26	0.35	0.26	0.27
	σ	0.13	0.22	0.16	0.19
θ_{e_ripple}	$\bar{x}$	78.7	57.0	49.3	62.7
	σ	40.8	20.2	24.7	30.9
e_{ripple}	$\bar{x}$	0.57	0.54	0.63	0.57

Impact, Rebound, and Ejecta Velocities

Impact velocities: v_{i_flat} & v_{i_ripple}

We quantify the impact velocities (v_i)(see Eq. 1) across the four flat bed runs (1-4, U_∞ = 7.1 to 8.5 m s^{-1}). The distribution of impact velocities for each flat bed run, v_{i_flat}, are shown via histograms (Fig. 9A) and boxplots (Fig. 9B). The v_{i_flat} medians are 2.4, 1.3, 1.6, and 1.8 *m* s^{-1} for runs 1-4. The maximum and minimum impact velocities are an order of magnitude difference, with the largest v_{i_flat} range from the lowest freestream velocity run (v_i = 0.6-7.1 ms^{-1}, U_∞ = 7.1 m) (Fig. 9).

To resolve trends and statistical differences in impact velocity (v_{i_flat}), and mean freestream speed (U_∞), we compare boxplots of impact velocities between flat bed runs with increasing mean freestream wind speed (Fig. 9B). Though not a true statistical test of significance, comparing boxplots for overlap provides insight on the statistical difference between the samples (i.e., if the boxplots do not overlap then perhaps there is a statistically significant difference). The lower and upper quartiles define the box of the boxplots. The lower (first) quartile is the middle number that falls between the smallest value of the dataset and the median. The upper (third) quartile is the central point that lies between the median and the highest number of the distribution. The quartile 1 and 3 (Q1-Q3) range for all runs overlap. This suggests no significant differences in impact velocities as mean freestream wind speed increases. Additionally, using Eq. 3, a two-sample t-test reports the statistical differences between the means of each sample (runs 1-4, U_∞ = 7.1 to 8.5 ms^{-1}). The null hypothesis is that the mean impact velocities are statistically equal across increasing freestream velocities. Results suggest the null hypothesis can be rejected at the 5% significance level when testing runs 1 to 2 and runs 1 to 4, indicating that these mean impact velocities are statistically different for these specific runs. The t-test for all other sample combinations (run 1 to 3, run 2 and 3, and runs 3 and 4) reported that the null hypothesis could not be rejected at the 5% significance level, suggesting

that the majority of our flat bed mean impact velocities are statistically similar as the freestream increases.

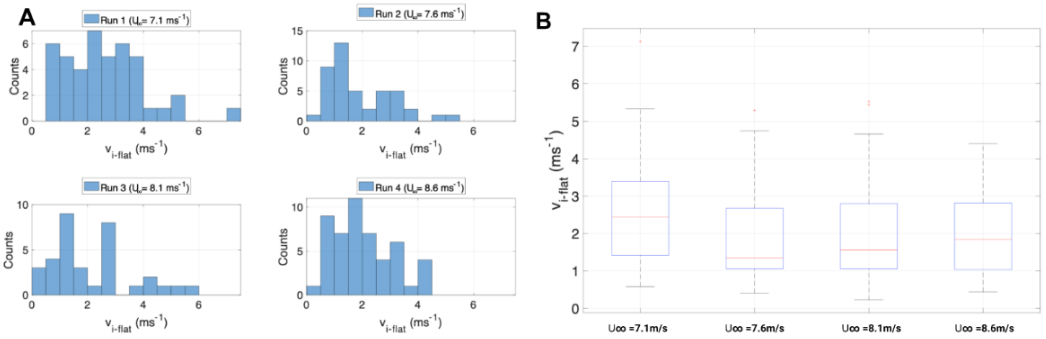

Figure 9: Flat bed impact velocities (v_{i_flat}) shown via (A) histograms and (B) box and whisker plots for runs 1-4 (U_∞ = 7.1 to 8.6 ms^{-1}).

We found similar results for the impact velocities from the rippled bed runs 5-8 (U_∞ = 7.1 to 8.6 ms^{-1}). Table 4 provides the summary statistics (v_{i_ripple}), and the velocity distributions are shown in Figure 10. Median v_{i_ripple} values are 1.9, 2.4, 1.1, and 1.8 ms^{-1} for runs 5-8 (U_∞ = 7.1 to 8.6 ms^{-1}) (Table 5). Maximum impact velocities over the rippled bed range from 5.8 to 7.5 ms^{-1}, and all minimum v_{i_ripple} are less than 0.5 ms^{-1} (Table 4, Fig. 10B).

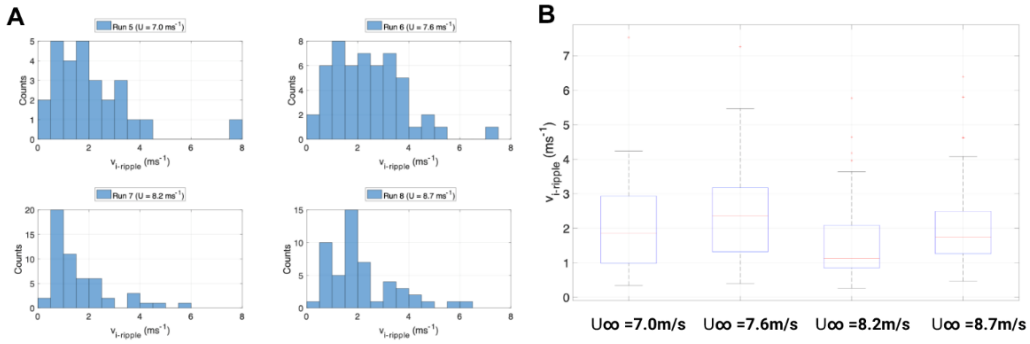

Figure 10: Rippled bed impact particle velocities (v_{i_ripple}) via (A) histograms and (B) box and whisker plots for runs 5-8 (U_∞ = 7.0 to 8.7 ms^{-1}).

The overlap of the boxplots in Figure 10B suggests the v_{i_ripple} distributions are similar. The same two-sample t-test and hypotheses were used to determine if the impact velocity means for rippled bed runs are statistically equal. Similarly to the v_{i_flat} dataset, the majority of the

v_{i_ripple} results are not statistically different from one another. T-tests for runs 6 and 7 (rippled bed, U∞ = 7.6 to 8.2 ms^{-1}) and runs 7 and 8 (rippled bed where U∞ = 8.2 to 8.7 ms^{-1}) indicate that the null hypothesis could be rejected at the 5% significance level and that the v_{i_ripple} means between these pairs are statistically different. T-tests for all other run comparisons (runs 5 vs. 6, 5 vs. 7, 5 vs. 8, and 6 vs. 8) show that the null hypothesis could not be rejected at the 5% significance level. Results suggest that increases in freestream velocity have little to no influence on the impact velocities across rippled surfaces.

Rebound Velocities: v_{r_flat} & v_{r_ripple}

The rebound velocities (v_r) for the four flat bed runs (1-4) were calculated using Equation 1 and are summarized in Table 3 (U∞ = 7.1 to 8.6 ms-1). The distributions of rebound velocities for each flat bed run, v_{r_flat}, are shown via histograms (Fig. 11A) and boxplots (Fig. 11B). The v_{r_flat} mean range is from 1.3 to 1.5 while the median values are slightly lower and range from 0.1 to 0.3. The v_{r_flat} distribution is generally lower than impact velocities (v_{i_flat}). Similar to the v_{i_flat} distribution, the v_{r_flat} maximum and minimum rebound velocities have an order of magnitude difference. For example, run 1 (U_∞ = 7.1 m) v_r ranges from 0.3-4.1 ms-1.

Comparing the boxplots in Figure 11B there is an overlap between the Q1-Q3 range/box for all runs overlap, suggesting no significant differences in rebound velocities as mean freestream wind speed increases. This is confirmed by T-tests for all v_{r_flat} distributions, which support that the null hypothesis could not be rejected at the 5% significance level (i.e., the sample means are statistically the same). Given the lack of statistically significant differences between the runs, it appears that rebound velocities do not scale with increasing mean wind speed for the range of freestream velocities investigated here.

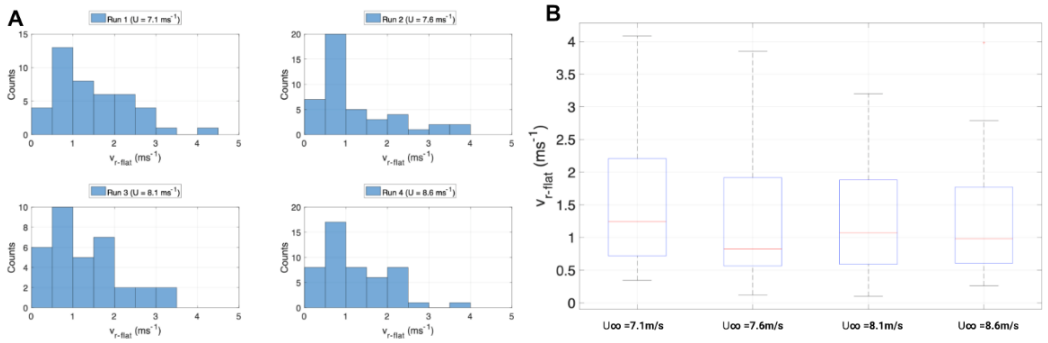

Figure 11: Flat bed rebound particle velocities (v_{r_flat}) via (A) histograms and (B) box and whisker plots for runs 1-4 (U_∞ = 7.1 to 8.6 ms^{-1}).

Table 4 and Figure 12 show rebound velocities, v_{r_ripple}, measured over the rippled bed. Median rebound velocities for runs 5-8 (U_∞ = 7.0 to 8.7 ms^{-1}) are 0.8, 1.1, 0.7, and 0.9 ms^{-1}, respectively. Maximum rebound velocities are all less than 5.3 ms^{-1} with minimum values below 0.5 ms^{-1}. Overlap between boxplots in Figure 12B suggests similarity across the v_{r_ripple} distributions. T-tests confirm that all v_{r_ripple} comparisons could not reject at the 5% significance level. Thus, the v_{r_ripple} means are all statistically similar and not influenced by increasing wind speed.

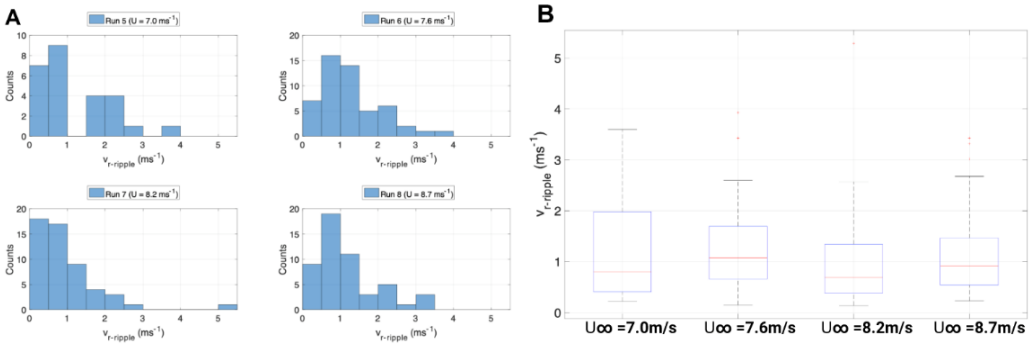

Figure 12: Rippled bed rebound particle velocities (v_{r_ripple}) via (A) histograms and (B) box and whisker plots for runs 5-8. (U_∞ = 7.0 to 8.7 ms^{-1}).

Ejecta Velocities: v_{e_flat} & v_{e_ripple}

Table 3 provides the summary statistics for the ejecta velocities (v_e). Figure 13A shows the ejecta velocities histograms for each flat bed run (v_{e_flat}). The v_{e_flat} mean and median ranged from 0.27-0.34 ms^{-1} and 0.24-0.33 ms^{-1}, respectively. These values are much lower than the impact (v_{i_flat}) and rebound velocities (v_{r_flat}). The maximum v_{e_flat} value for all flat bed runs is 1.51 ms^{-1}.

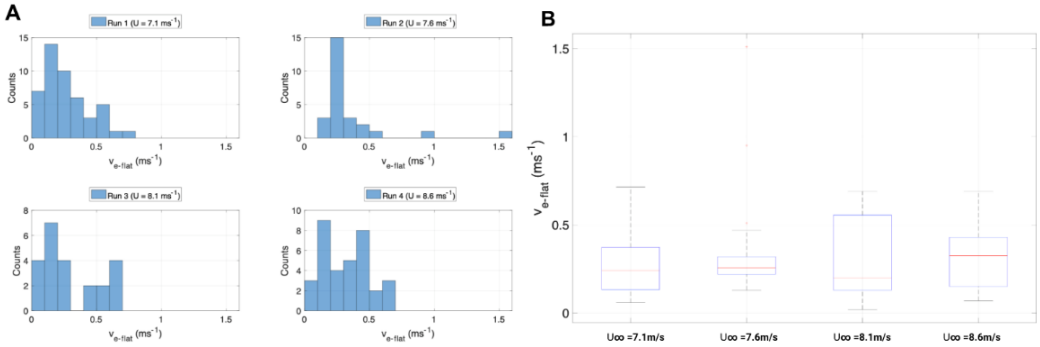

Figure 13: Flat bed ejecta velocities (v_{r_flat}) via (A) histograms and (B) box and whisker plots for runs 1-4. (U_∞ = 7.1 to 8.6 ms^{-1}).

The overlap of the boxplots in Figure 13B and results of the t-tests suggest that ejecta velocities also do not scale with increasing mean wind speed. Furthermore, the t-tests confirm that all the ejecta velocities (v_{e_flat}) means are statistically equal.

The velocity distributions for ejecta (v_{e_ripple}) and related summary statistics for the rippled bed runs (5-8, U_∞ = 7.0 to 8.7 ms^{-1}) are shown in Figure 14 and Table 4. The median v_{e_ripple} range from 0.2 and 0.4 ms^{-1} across the four runs. Minimum v_{e_ripple} values for each run are all below 0.09 ms^{-1} with maximum values below 1.32 ms^{-1}. Overlap in the distributions (Fig. 14B) and t-tests indicate that the null hypothesis could not be rejected at the 5% significance level for all runs. Similar to the flat bed runs, there is no significant difference in ejecta velocity distributions across runs with increasing wind speeds.

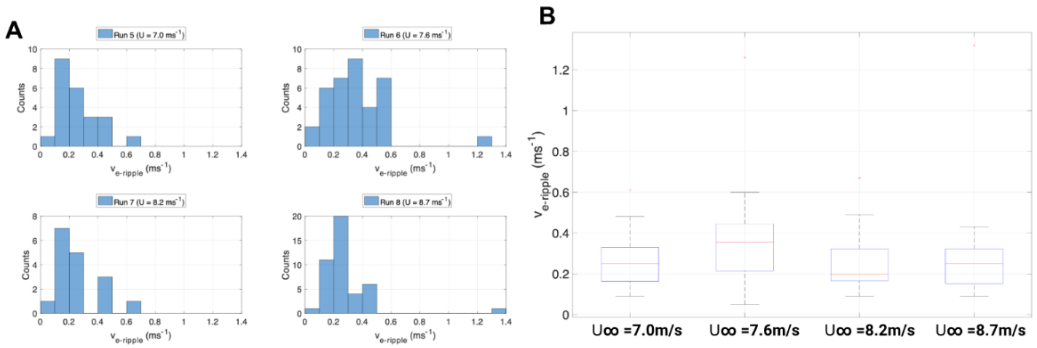

Figure 14: Rippled bed new ejected particle velocities (v_{e_ripple}) via (A) histograms and (B) box and whisker plots for runs 5-8. (U_∞ = 7.0 to 8.7 ms^{-1}).

A key contribution of this project is incorporating runs with natural rippled beds. Data shown in Figures 10-15 and Tables 3 and 4, as well as the series of t-tests, support our findings that increasing wind speeds have little to no effect on mean particle velocities across both flat (U_∞ = 7.1 to 8.6 ms^{-1}) and rippled surfaces (U_∞ = 7.1 to 8.6 ms^{-1}).

Coefficient of Restitution Across Flat and Rippled Bed

To understand the rebound process and particle-bed interactions, it is common to use the coefficient of restitution, CoR or ϵ, which is defined as the ratio of the rebound velocity to the impact velocity (Eq. 3). Tables 3 & 4 show the mean restitution coefficient (ϵ_{ripple}) for each flat bed run (1-4, U_∞ = 7.1 to 8.6 ms^{-1}) (ϵ_{flat}) and rippled bed run (5-8, U_∞ = 7.0 to 8.7 ms^{-1}). Values range from 0.54 to 0.70.

Figure 15 shows the histogram counts and normal distribution fit (PDF) for ϵ_{flat} and ϵ_{ripple}; grouped by bed surface type. For the flat bed runs 1-4 (U_∞ = 7.1 to 8.6 ms-1), ϵ_{flat} distribution has a mean value of 0.6 ms^{-1} indicating that the average salton velocities are 40% slower post-impact. For the rippled bed runs 5-8 (U_∞ = 7.0 to 8.7 ms^{-1}), the ϵ_{ripple} distribution mean is slightly lower at 0.57 ms^{-1}, which also supports a mean particle velocity reduction of about ~40% post-impact.

Furthermore, the t-tests between the flat bed (ϵ_{flat}) and rippled bed CoR datasets (ϵ_{ripple}) show the null hypothesis could not be rejected at the 5% significance level, indicating that the means are equal and CoR of splash events is not influenced by bedforms. The second round of t-tests compared runs with increasing wind speed. Comparing ϵ_{flat} distribution runs 1-4 (U_∞ = 7.1 to 8.6 ms^{-1}) to each other, all resulting in not rejecting the null hypothesis (means are equal) at the 5% significance level. T-tests for the ϵ_{ripple} distributions (runs 5-8, U_∞ = 7.0 to 8.7 ms^{-1}) found the same result: the mean values are not significantly statistically different. Thus, our ϵ_{flat} and ϵ_{ripple} distributions are statistically similar, and CoR distributions showed no distinguishable response with increasing wind speed or bedforms.

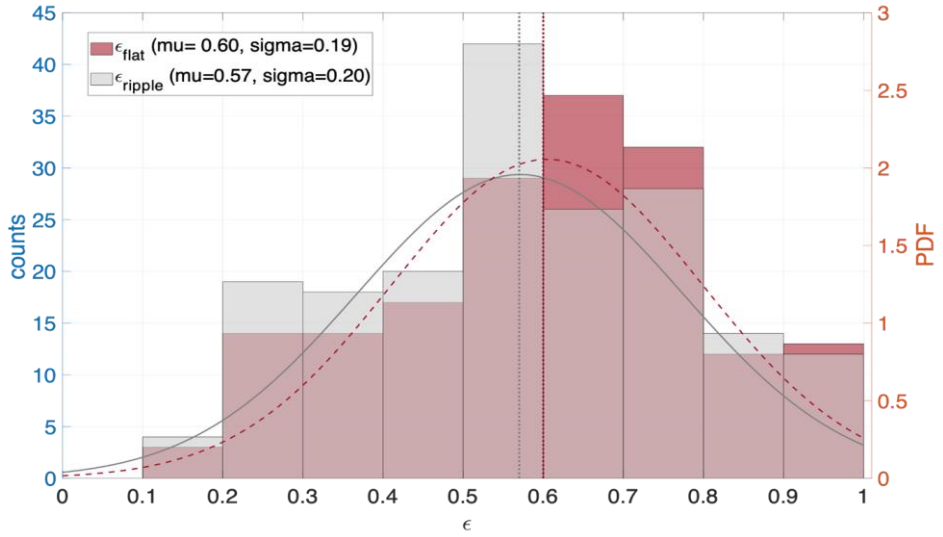

Figure 15: The coefficient of restitution histograms and normal distribution PDFs for the flat bed runs 1-4 (U_∞ = 7.1 to 8.6 ms^{-1}, dashed line), and the rippled bed runs 5-8 (U_∞ = 7.0 to 8.7 ms^{-1}, solid line).

Above we reported that mean impact and rebound velocities did not increase with freestream velocity. Yet, impact and rebound velocities do vary within any given run (Fig. 9-12). Figure 16 shows the relationships between increasing impact velocity on rebound velocity as well as the CoR. For both the flat bed datasets (runs 1-4) and rippled bed datasets (runs 5-8), rebound velocity increases with impact velocity (Fig. 16 A&C). Figures 16 B&C show the CoR has no or a slightly negative relationship to impact velocities. Rebound velocities increase with impact velocity, but the ratio between the two, on average, remains constant, although there is a large spread in the data defining these relationships.

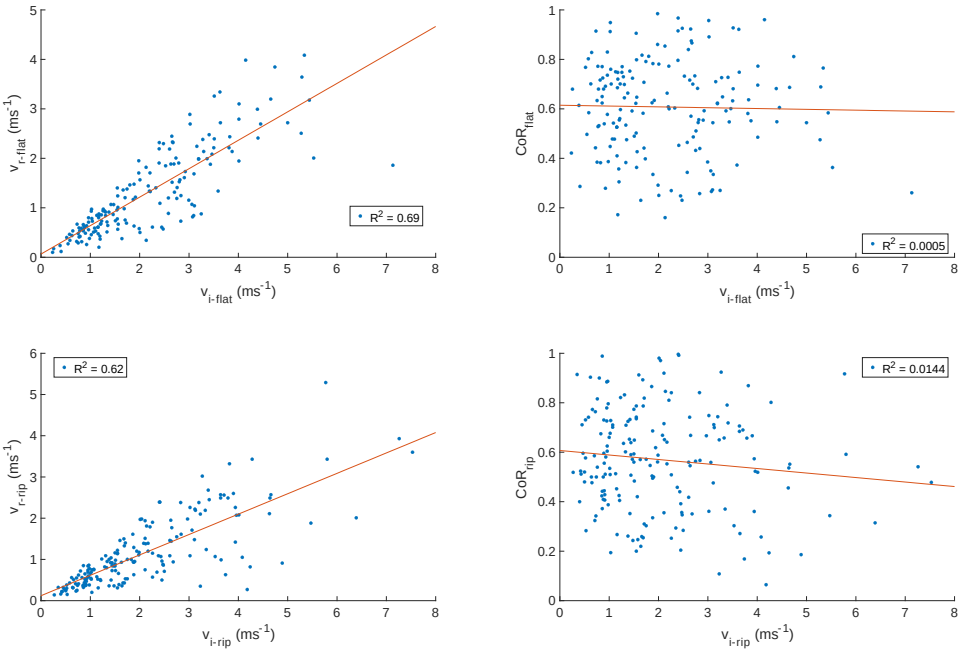

Figure 16: A&C show a strong positive relationship between rebound velocity vs. impact velocity, and B&D show a slightly negative relationship between CoR and impact velocity. A&B are splash events from flat bed runs 1-4 ($U\infty$ = 7.1 to 8.6 ms^{-1}), and C&D are splash events from rippled bed runs 5-8 ($U\infty$ = 7.0 to 8.7 ms^{-1}).

Impact, Rebound, and Ejecta Angles Across Flat Beds

Sand grain trajectories are determined by the ballistic variables of launch speed and launch angle. We calculate impact (θ_i), rebound (θ_r), and ejecta angles (θ_e) and compare the distributions for statistically significant differences related to increases in freestream velocity and/or the presence or absence of ripples. The distributions of particle angles from the flat bed runs (1-4, U_∞ = 7.1 to 8.6 ms^{-1}) are summarized in Table 3. Polar histograms are provided in Supplemental Figures.

Results suggest that mean freestream velocity has little to no effect on the mean impact angle ((θ_{i_flat}). Mean impact angles (θ_{i_flat}) ranged from 14.4 to 19.1° for flat bed runs 1-4 (U_∞ = 7.1 to 8.6 ms^{-1}). The θ_{i_flat} distributions had narrow ranges and smaller standard deviation

values, σ = 6.7 to 8.1 ms^{-1} (Table 3). Note that these particles were all saltons; a criterion for identifying the start of a splash event to digitize (Sec. 4.3). Generally, the mean and standard deviations for the rebound (θ_{r_flat}) and newly ejected particle (θ_{e_flat}) angles are larger than those of the impacting saltons (θ_{i_flat}). Rebounding particles leave the bed at mean angles ranging from 35.5 to 43.8°, but ejecta leave the bed at mean angles between 57.9 to 76.1°. Distributions of rebounding particles and ejecta exhibit a larger spread and standard deviation than the impacting angles of saltons.

The same two-sample t-test was used to compare salton impact angle distributions from increasing wind speed runs as well as for the rebound and ejecta angle distributions. T-test for the impact angle flat bed datasets (θ_{i_flat}) suggest rejecting the null hypothesis for runs 2 and 4 (U_∞ = 7.6 and 8.6 ms^{-1}) and runs 3 and 4 (U_∞ = 8.1 and 8.6 ms^{-1}). T-test for all other run comparisons (4/6 tests) suggests the null hypothesis (means are equal) can not be rejected at the 5% significance level. Thus, the majority of our results indicate that the impact angle distributions remain statistically similar as wind speed increases.

T-test for the rebound angles (θ_{r_flat}) across all flat bed runs 1-4 (U_∞ = 7.0 to 8.6 m s-1) indicate that the null hypothesis could not be rejected at the 5% significance level; the rebound angle means across all runs are equal. Results for the ejecta angles (θ_{e_flat}) had varying results. Results for runs 2 and 3 (U_∞ = 7.6 and 8.1 ms^{-1}) and runs 3 and 4 (U_∞ = 8.1 and 8.6 ms^{-1}) suggest that the null hypothesis could be rejected. The remainder of the t-test results (4/6 tests) all indicated that the null hypothesis could not be rejected at the 5% significance level. These results support that freestream velocity has little to no effect on the mean rebound angle (θ_{r_flat}) and ejecta angles (θ_{e_flat}).

Previous experiments report relationships between impact and rebound angle. Figure 17 shows the rebound vs. impact angle for all splash events from the flat bed runs. The linear regression produces an R^2 of 0.0035. It is unsurprising not to find a strong relationship with impact angle given the standard devotions in Table 3.

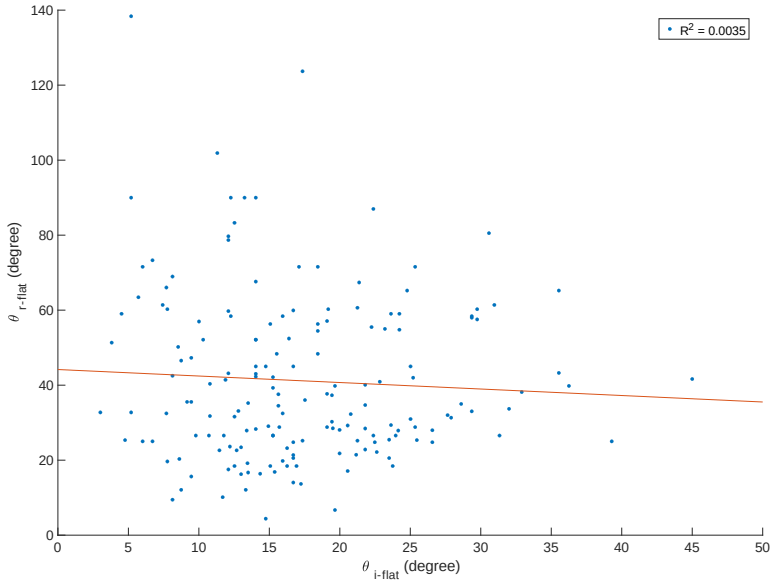

Figure 17: Rebound vs. Impact angle for all splash events from the flat bed runs 1-4 (U_∞ = 7.1 to 8.6 ms^{-1}). The linear regression has an R^2 of 0.004.

Impact, Rebound, and Ejecta Angles Across Rippled Beds

To quantify the effect of ripples' slope on particle trajectory characteristics, we group splash events from runs 5-8 (U_∞ = 7.0 and 8.7 ms^{-1}) by location on the ripples (i.e., stoss, lee, crest, or trough). Figure 18 shows the image segmentation by x-pixel value for each aspect. Eq. 2 calculated the salton impact (θ_i), rebound (θ_r), and ejecta angles (θ_e).

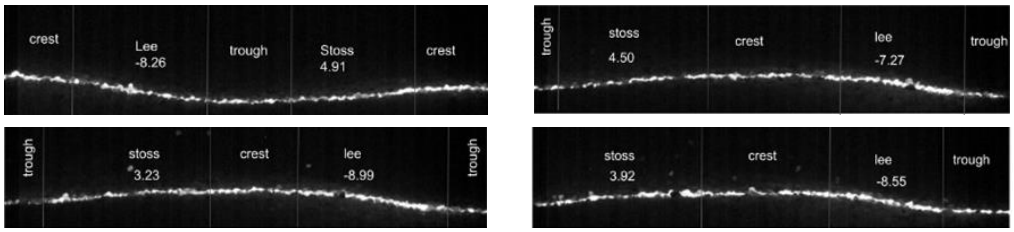

Figure 18: Images from rippled bed runs (U∞ = 7.0 to 8.7 ms-1) that indicate the different aspects of ripple microtopography (stoss, lee, crest, trough). (A) run 5, (B) run 6, (C) run 7, and (D) run 8.

Table 5: Summary statistics of splash characteristics from rippled bed runs (5-8, U_∞ = 7.0 to 8.7 ms^{-1}) group by ripple aspect.

Run	Ripple Feature	n_i	V_{i_ripple}		$theta_{i\_ripple}$		V_{r_ripple}		$theta_{r\_ripple}$		n_{ej}	V_{e_ripple}		$theta_{e\_ripple}$		CoR
			mean	std	mean	std	mean	std	mean	std		mean	std	mean	std	
5	stoss	11	1.95	1.12	14.33	5.96	1.15	0.87	40.51	19.08	0.91	0.27	0.10	65.98	38.16	0.59
	crest/trough	14	2.27	1.87	16.41	9.68	1.30	1.00	49.20	19.10	0.79	0.24	0.15	89.71	22.61	0.57
	lee	2	1.76	0.17	23.28	4.66	0.65	0.40	4.23	10.02	1.00	0.22	0.16	75.82	77.47	0.37
6	stoss	20	2.38	1.70	18.56	8.22	1.18	0.92	61.27	26.65	0.95	0.31	0.18	55.29	15.29	0.50
	crest/trough	25	2.58	1.23	19.93	8.98	1.39	0.79	46.63	28.93	0.60	0.30	0.13	53.68	20.23	0.54
	lee	7	1.91	1.07	24.39	9.54	1.00	0.64	50.68	49.68	0.29	0.44	0.08	36.82	21.24	0.52
7	stoss	22	1.42	1.20	18.13	7.09	0.81	0.73	49.45	35.33	0.36	0.22	0.13	32.62	10.74	0.57
	crest/trough	18	1.84	1.23	20.38	6.74	1.29	1.20	47.78	22.91	0.28	0.25	0.13	66.85	25.53	0.70
	lee	13	1.44	1.02	25.48	7.59	0.75	0.43	32.09	18.78	0.31	0.31	0.26	54.36	23.33	0.52
8	stoss	26	2.35	1.41	13.40	5.81	1.21	0.82	46.06	22.22	1.04	0.35	0.26	69.41	31.29	0.51
	crest/trough	20	2.03	1.27	18.47	9.94	1.20	0.86	48.84	25.24	0.60	0.21	0.10	56.07	27.78	0.59
	lee	4	1.41	0.48	32.40	6.37	0.63	0.36	47.22	24.81	0.75	0.21	0.12	25.93	4.85	0.45

Table 5 shows the mean and standard deviation for salton impacts, rebounds, and ejecta trajectories. Across all runs and aspects, impact angle (θ_{i_ripple}) mean and standard deviation values are consistently lower than the rebound angles (θ_{r_ripple}). This matches the θ_{i_flat} results (Table 3). However, the mean impact angles are consistently larger on the lee (θ_{i_lee}) than those on stoss or crest/trough (θ_{i_stoss} and $\theta_{i\_c/t}$). This suggests that saltating grains need larger impact angles to be able to impact the lee aspect of the ripple.

For runs 6 and 7, which have larger impact counts (n_i) on the lee, the mean rebound angles are larger on the stoss (θ_{i_stoss}) than the mean rebound angles on the lee (θ_{i_lee}) (Table 5). From Tables 3 and 4, we can compare the means from each flat bed run (θ_{r_flat}) and each rippled bed run (θ_{r_flat}). θ_{r_flat} ranges from 35.5-43.5°, and θ_{r_ripple} ranges from 44.1-52.8°. It is interesting that the mean rebound angles are all larger from the rippled bed runs. Though still

inconclusive, these results suggest that the increases in the local slope (i.e., stoss) can result in larger rebound angles of saltons.

Newly Ejected Particle Counts

For each digitized splash event, the number of rebounds and their associated ejecta were documented. An important finding was that >99% impacting particles rebounded for all digitized splash events (e.g., all but one impacting salton rebounded). Thus, there are no figures for rebound data, and this section focuses on the newly ejected particles.

The number of ejecta per splash is shown in Figure 19 and Tables 3 and 4. The height of the newly ejected particles was also recorded. Particles were classified as remaining within the transport layer (where mean fluid velocities are low) or as leaving the transport layer (particles reached a height >=1 cm). An important finding was that each impacting particle rebounded for all digitized splash events. Thus, there are no figures for rebound data, and this section focuses on the newly ejected particles.

Histograms and cumulative distribution functions (CDFs) of the newly ejected particle counts for all the experimental runs (Fig. 19 A-D: flat bed runs 1-4, U_∞ = 7.0 to 8.6 ms^{-1}) (Fig. 19 E-H: rippled bed runs 5-8, U_∞ = 7.1 to 8.7 ms^{-1}). The left axis shows the distribution of the number of newly ejected particles that remain close to the bed (<1 cm) and the number of particles that leave the transport layer (>=1 cm). The right axis shows each run's CDF. The CDF shows the probability that the variable will be less than or equal to that value. Thus, the CDF value where x equals zero provides the probability that a splash event will result in no newly ejected particles.

Splash events frequently resulted in zero newly ejected particles. The flat bed runs 1-4 (U_∞ = 7.0 and 8.6 ms^{-1}) are shown in the left column of the plots (Fig. 19 A-D), and the rippled bed runs are in the right column (Fig. 19 E-H). CDF curves where x equals zero show the probability for zero newly ejected particles ranging from 0.44 to 0.81. For runs 2, 3, 6, and 7 (Fig. 19 B,C,F), the probability of ejecting new particles is well above 0.5 and runs 4 and 5 (Fig. 19 D, E) are slightly below 0.5 probability.

The maximum number of newly ejected particles ranged from 2-6 across runs 1-8 (Fig. 19 A-H). Most newly ejected particles stayed within 1 cm of the bed. Of the newly ejected particles that did reach >=1 cm, frequently, it was only one or two. Large splash events, >=3 newly ejected particles, are seen in all runs except run 7 (Fig. 19 G) (rippled bed, $U_\infty = 8.2$).

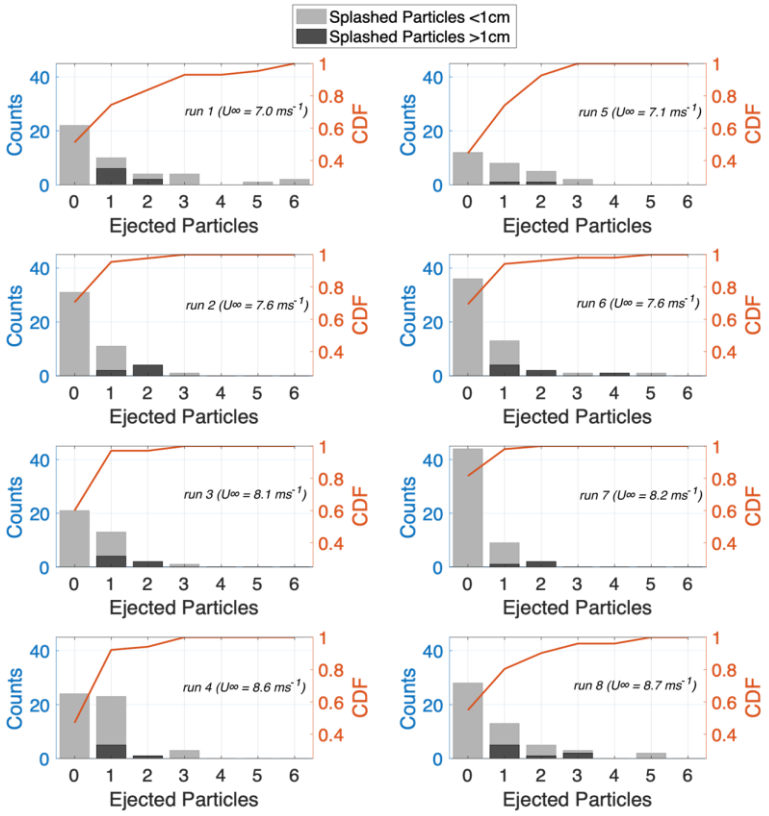

Figure 19: Distributions of newly ejected particle counts for flat bed runs 1-4 (A-D) and rippled bed runs 5-8 (E-H). The left axis shows non-normalized histogram counts for ejected particles that remain close to the bed (<1 cm) or leave the transport layer (>=1 cm). The right axis shows the CDFs for all ejected particles for each run.

Splash Events With and Without Newly Ejected Particles

Figure 20 A&C show the slightly positive relations between ejecta counts and impact velocity from our flat bed runs and rippled bed runs. There is the opposite relationship between

ejecta counts and impact angle (Fig. 20 B&D). Both are weak relationships with R^2 values below 0.2.

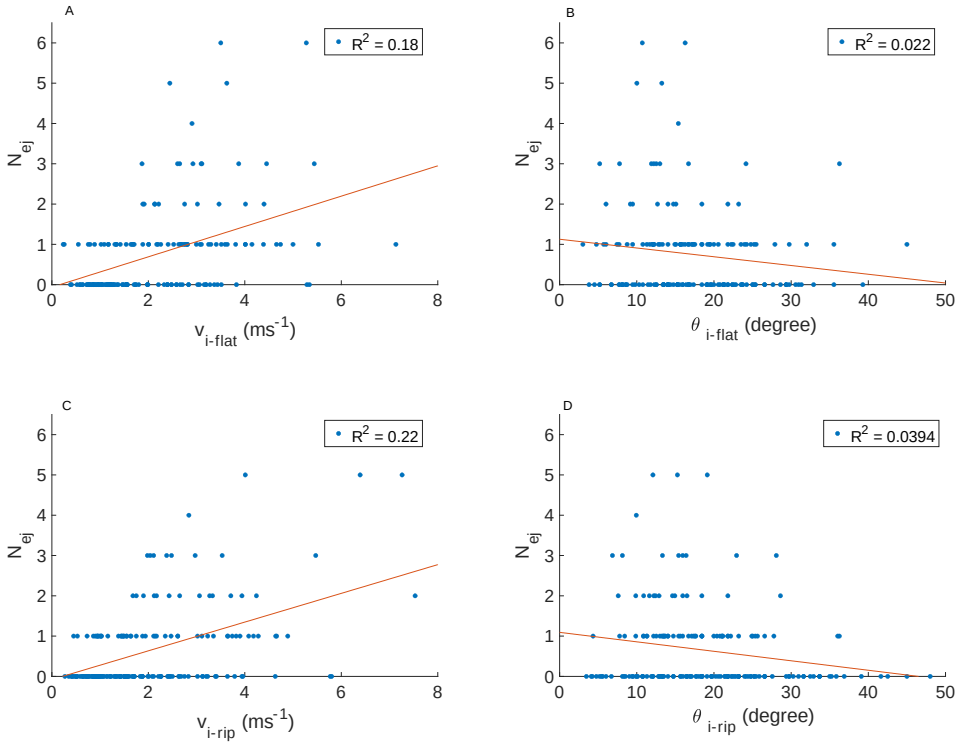

Figure 20: (A&C) ejecta counts vs. impact velocity, and (B&D) ejecta counts vs. impact angle. (A&B) show the flat bed data, and (C&D) show the rippled bed data.

To understand further why some splash events, result in newly ejected particles while others do not, impact velocities (v_i), angles (θ_i), and coefficient of restitution (ϵ) are analyzed between splash events with different resultant ejecta particle counts. Histograms of impact velocity, impact angle, and CoR and fitted distributions for flat bed runs are shown in Figure 21 A, and Figure 21 B shows the rippled bed runs. Table 6 also shows the summary statistics and distribution parameters.

For the flat bed runs (Fig. 21 A), splash events with newly ejected particles are generally associated with higher impact velocities (v_{i_flat}). The v_{i_flat}mean is 2.71 ms^{-1} for splash events with ejecta compared to a v_{i_flat} mean value of 1.67 ms^{-1} for splash events with no ejecta (Fig.

21A). There is a similar relationship for the rippled bed runs (Fig. 21 B). The mean v_{i_tipple}value for splash events with ejecta 2.63 ms^{-1} and 1.69 ms^{-1} or splash events with no ejecta.

There is an opposite trend between impact angle (θ_i) and ejecta counts. Splash events with newly ejected particles generally had lower impact angles (θ_i) (Fig. 21 A&B). Ejected particle splashes had a mean angle of 16.42° and 16.59° for the flat and rippled bed runs. These values are lower than the no ejected particle events, with 17.99° and 20.34° for the flat and rippled bed runs, respectively (Fig. 21 A&B).

There is a slight shift toward higher CoR (ϵ) values for the splash events without newly ejected particles for both the flat bed and rippled bed data (Fig. 21 A&B). The mean ϵ values for the splashes with ejected grains are 0.51 for the flat bed runs (runs 1-4, U_∞ = 7.0 to 8.6 ms^{-1}) and 0.58 for the rippled bed runs (runs 5-8, U_∞ = 7.1 to 8.2 ms^{-1}). The mean ϵ values for the splashes without ejected grains are larger; 0.61 for the flat bed runs (runs 1-4, U_∞ = 7.0 to 8.6 ms^{-1}) and 0.63 for the rippled bed runs (runs 5-8, U_∞ = 7.1 to 8.2 ms^{-1}).

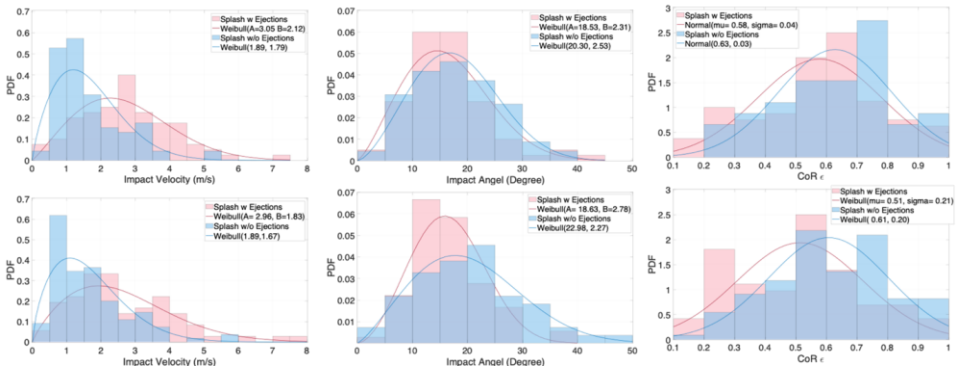

Figure 21: Distributions of impact velocity and angle and event CoR for (A) flat bed runs (1-4, U_∞ = 7.0 to 8.6 ms^{-1}) and (B) rippled bed runs (5-8, U_∞ = 7.1 and 8.7 ms^{-1}). Splash events distributions with >=1 newly ejected particles are red, and those without newly ejected particles are blue.

A series of t-tests between the flat bed distributions (Fig. 21A) suggest that the only variable that produced statistically significant different distributions between splashes with and without ejecta was impact velocities (v_{i_flat}). The p-values for the flat bed impact angle test and

coefficient of restitution test were larger than 0.05, while the impact velocity t-test produced a p-value of 2.9×10^{-8}. Thus, the mean impact velocities for splash events with and without newly ejected particles are unequal. From Figure 21 A, the impact velocity distribution for the splash events that produced newly ejected particles is shifted to the right (larger velocities). These results support that for the flat bed runs, impacts with higher velocities are more likely to eject more particles.

For the rippled bed data, there are visible differences between the impact velocity distributions (v_i) and impact angle (θ_i) for splash events with or without newly ejected particles (Fig. 21 B). An additional series of p-tests confirm that for all splash event variables (v_{i_ripple}, θ_{i_ripple}, ϵ_{ripple}) the distributions for with and w/o ejecta particles were all statistically different. All tests had p-values below 0.05 (2.26×10^{-6}, 0.0038, 0.0024 for velocity, angle, and CoR). These results suggest that for the rippled bed runs, impacts with higher velocities, smaller impact angles, and lower CoR values resulted in splash events with >0 newly ejected particles.

Table 6: The summary statistics and distribution parameters for the impact velocity, impact angle, and coefficient of restitution data from flat bed and rippled bed runs are shown in Figure 21.

			Sample Size	Distribution	Mean	Variance	Log Likelihood	A	B
Flatbed runs (1-4)	With Ejecta	Impact Velocity	80	Weibull	2.71	1.80	-134.10	3.05	2.12
	W/o Ejecta	Impact Velocity	91	Weibull	1.67	0.94	-116.29	1.89	1.79
	With Ejecta	Impact Angle	80	Weibull	16.42	56.82	-270.42	18.53	2.31
	W/o Ejecta	Impact Angle	91	Weibull	17.99	57.98	-311.96	20.30	2.53
	With Ejecta	COR	80	Normal	0.58	0.04	14.84	N/A	N/A
	W/o Ejecta	COR	91	Normal	0.63	0.03	25.18	N/A	N/A
Ripple bed runs (5-8)	With Ejecta	Impact Velocity	72	Weibull	2.63	2.22	-124.64	2.96	1.83
	W/o Ejecta	Impact Velocity	110	Weibull	1.69	1.08	-146.60	1.89	1.67
	With Ejecta	Impact Angle	72	Weibull	16.59	41.76	-233.031	18.63	2.78
	W/o Ejecta	Impact Angle	110	Weibull	20.34	90.51	-400.2	22.98	2.27
	With Ejecta	COR	72	Normal	0.51	0.04	12.15	N/A	N/A
	W/o Ejecta	COR	110	Normal	0.61	0.04	23.96	N/A	N/A

Discussion

Our dataset provides new insights into the details of splash events' impacts, rebounds, and ejecta characteristics. Imaging and tracking particles near the bed have proven difficult due to lighting restrictions, bed reflectance, high concentrations of particles, and the time requirement of manual tracking. This project highlights the recent technological improvements and the continued value of non-automated tracking. We synthesize our findings into four main topics related to splash dynamics: impact characteristics, rebound processes, ejection processes, and the influence of ripple morphology.

Impacting Saltons Velocities and Angles Invariant with Wind Strength

How particle trajectories scale with wind speed is critical for flux equations. Yet, there is uncertainty in the literature on the behavior of particle trajectory and speed with increasing wind strength. For instance, Bagnold-type models assume that saltation length and particle velocity scale with increasing wind strength (e.g., Bagnold, 1941). Further, impact velocities of saltons are also a key input for numerical models. More data is needed across varying wind speeds and bedforms. These fundamental mechanics built into aeolian sand transport models remain largely unresolved (Valance et al., 2015). For example, wind-tunnel experiments find that particle velocities do not scale to wind strength (Nalpanis et al., 1993; Rasmussen & Sørensen, 2008; Ho et al., 2011, 2014). Martin & Kok's (2017) analysis of field data with additional results from Greeley et al. (1996), Namikas (2003), and Farrell et al. (2012) show that saltation layer heights remain essentially constant with wind shear velocity. The constancy of the saltation layer height implies that mean particle speeds also remain approximately constant. Results here support previous findings that wind strength has a limited or no influence on mean particle velocity.

Our mean impact velocities generally align with previous findings of Willetts & Rice (1986), Hunt & Nalpanis (1985), and Gordon and Neuman (2011). Willetts & Rice (1986) report a slightly larger mean of 3.60 ms-1 (for a similar grain size), and Hunt & Nalpanis (1985) report a lower value (1.5 ms-1) for a smaller grain size. Though Gordon and Neuman's (2011) results

have lower impact velocities than ours, their data show consistent mean impact velocities with increasing freestream increases. In terms of differing results from previous experiments, the variability in grain size and experimental designs (e.g., saltation cloud vs. a single collision), and not freestream velocity, produce differences in mean impact velocities. For example, Gordon and Neuman (2011) used finer sand (0.0303 vs. 0.0456 cm) in addition to having higher freestream steams.

Valance et al. (2015) suggest that the dependence of saltation layer height, particle velocity, saltation length, and mass flux with grain size remains an important open issue within aeolian sediment transport. Willets and Rice (1986) state that grain shape influences splash; decreasing sphericity (rounder) results in lower velocities and angles. Also, sphericity was linked to increased bed activity (transport). Durán et al. (2011) predict that the saltation layer height and the saltation length should scale linearly with the grain diameter, but this needs to be confirmed by empirical data. A trade-off between our manual tracking and some automated methods is the lack of grain size information without additional measurement steps. Thus, our current efforts do not include grain size. Previous results suggest an important role of grain characteristics. Thus, incorporating grain size and shape will be an important next step for the current dataset.

In summary, empirical data (both presented here and previously) suggests that impact velocities are invariant to wind speed. This agrees with the splash-dominated saltation models of Anderson (1987) and Werner (1990), which set mean saltator liftoff and impact speeds as invariant to wind shear stress. Furthermore, Ungar and Haff's (1987) and Andreotti's (2004) models suggest that particle entrainment is predominantly driven by splash because near-surface wind speeds are significantly reduced from momentum extraction by particles in motion that fluid. Thus, if fluid velocity is reduced so much that lift has a minimal role in particle entrainment, an explanation for increases in transport rates with higher wind velocities (without increases in mean particle velocities) requires a high rebound percentage and/or ejection of additional grains from impacts at higher wind speeds and sand transport rates. Both are discussed in the following sections.

Rebound Process and Functions

Splash events result in horizontal to vertical momentum conversions during bed impacts. Accurate rebound characteristics are important for describing splash dynamics. Empirical data for rebound functions are important for modeling cloud characteristics and estimating saltation flux. The percentage of impacting saltons that rebound is an under-analyzed parameter (Valance et al., 2015; Kok et al., 2017). An exception to this gap is the numerical study by Anderson et al. (1991) that suggests that an exponential function can approximate the probability that a saltating particle will rebound (P_r):

$$P_r = B[1 - exp(-\gamma\, v_i)] \qquad \text{Eq (5)}$$

where the parameter B was determined to be ≈ 0.95 for 0.025 cm for sand particles, and the parameter γ is estimated to be of order 2 sm^{-1} (Anderson et al., 1991). Equation 5 is also used by the popular numerical model for steady-state saltation, COMSALT (Kok & Renno, 2009). Using our mean v_{i_flat}, Eq. 5 produces a rebound probability of 0.93. Figure 22 shows the distribution of all rebound probabilities based on the v_{i_flat}distribution. Most of the impacts from this study have a 50% or more probability of rebounding.

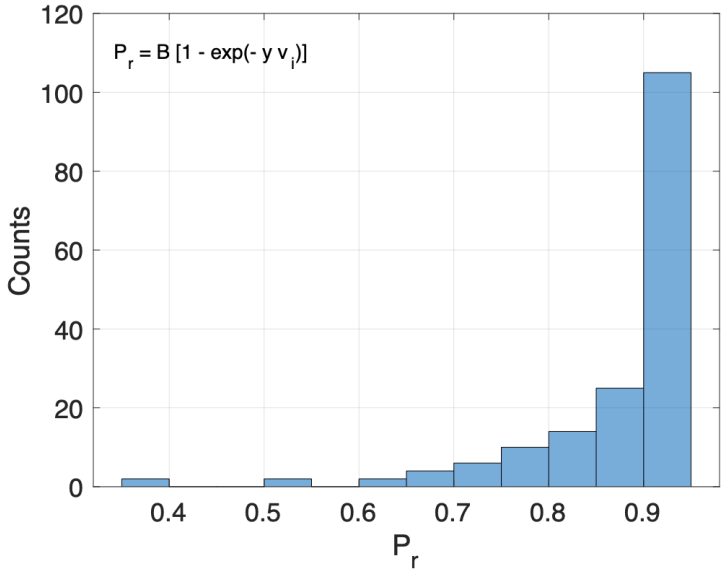

Figure 22: Distributions rebound probabilities (P_r) from v_{i_flat} distribution.

Our calculated rebound probabilities (Fig. 22) using Anderson's (1991) approach and the impact velocity collected here match our empirically expressed rebound percentages. More than 99% of our digitized splash events included the salton rebound. There is limited data to compare to. Relating to results from Gordon and Neuman's (2011) is difficult because they combined ricocheted (rebounding) particles with all other ejecta. Still, their mean ejecta count per splash, including the rebounding particles, ranges from 1.1 to 1.2, suggesting that most of their impacting sand particles rebounded.

In theory, if below a critical impact velocity, particles will be trapped by the bed and will not rebound (Mitha et al., 1986; Anderson et al., 1991; Beladjine et al., 2007). Though Equation 5 does not define a critical impact velocity for rebound, it is important in modeling splash dynamics. From our experimental conditions, given that the only impact that did not rebound had a velocity of 0.44 ms^{-1}, this is likely near the critical impact velocity for a salton to rebound. Though, suggesting a critical impact velocity for rebound may be hasty. Recall that our digitization protocol was designed around tracking saltons using a vertical height threshold. Chapter one results show that a boundary between sand transport modes' velocity is difficult to define (especially at higher

transport rates). Thus, the current dataset may exclude some slower saltons, which may or may not have rebounded. Thus, defining an impact velocity threshold for rebound is beyond the scope of this work.

In addition to estimating rebound probability and validating rebound functions, these data allow for comparing rebound characteristics (velocity and angle) across different impact attributes. Though mean impact and rebound velocities generally remain constant with increasing wind speed, Figures 9 & 10 and Tables 3 & 4 highlight the variability within any given run. Splash events with higher impact velocities generally result in higher rebound velocities. Figures 16 A&C show that rebound velocities increase with increasing impact velocity but at a slightly slower rate (the linear regressions have slopes of 0.6 and 0.5).

Figure 16A shows a strong positive relationship between rebound and impact velocity. The low R^2 between CoR and impact velocity (Fig. 16B suggests) that despite scatter, the rebound to impact velocity ratio remains consistent with increasing impact velocity. As shown in Figure 15 and supported by Wang et al.'s (2008), the CoR is approximately normally distributed. However, the CoR range seems large for impact velocities below 4 ms^{-1}. For rebounding particles to travel at such different speeds when starting at the same initial velocity supports the role of bed conditions and grain characteristics. Though our sand was well-sorted, it is clear in the HS imagery that there is still a grain size and angularity variability. Previous results suggest that more angular grains results in higher rebound velocities and angles (Willetts & Rice, 1986). Though outside of the scope of this current effort to quantify the role of various grain characteristics on trajectories, these results highlight the important role of particle and bed material in physical and numerical modeling. Potential influences on particle trajectories and splash characteristics should be considered if anything other than sand was used in the experimental design.

Further examination of Figure 16 B&D suggests a different trend when focusing on impact velocities above 4 ms^{-1}. Analyzing the entire dataset suggests no relationship between CoR and impact velocity. However, in the faster (upper) half of the distribution (>=4 ms^{-1}), there appears to be a stronger negative relationship. Though additional analysis is needed, this further

supports the theory that particle velocities do not scale with increasing wind speed. In other words, when additional momentum is extracted from the fluid by saltons, resulting in higher impacting speed, it is transferred to the bed and ejecta- instead of being translated into higher rebound velocities. This theory is further explored in the ejecta discussion.

Comparing CoR results across experiments suggests a potential design issue. Gordon and Neuman (2011) and McEwan et al. (1992) reported mean CoR of 0.5 and 0.6. Both the flat and rippled bed run datasets align with these previous results and those reported by Gordon and Neuman (2011) for the saltation runs with sand. Interestingly, Gordon and Neuman (2011) report a much lower mean CoR (0.36) for the high-speed collision experimental runs. Instrument limitations of data collection within a highly saturated cloud have required workarounds to measure particle trajectories from higher wind speed conditions. Thus, many previous experiments have used apparatus to fire a single particle at the bed at higher speeds. The differences in CoR and other results (e.g., Beladjine et al., 2007) between saltation and collision experiments suggest that the latter may not be appropriate for quantifying aeolian saltation cloud attributes. Specific collision experiments that use incorrect particle velocity scaling assumptions may include results that do not apply to natural saltation processes.

Lastly, results included rebound angles. Once a salton rebounds, it is important to characterize the particle angles. We find rebound angles are larger and more variable than impact angles, resulting in a weak relationship between the two. Previous work suggests rebound angles range from 20° to 40° (Willets & Rice, 1986; Gordon & McKenna Neuman, 2011; Valance et al., 2015). Our mean rebound angles range from 35.5° to 52.8°. Beladjine et al. (2007) and others have shown that the rebound process is not specular. Beladjine et al. (2007) also suggest that grazing impact angles (<20◦) result in greater rebound angles than the incident angle. However, for impact angles higher than 20◦, the rebound angle is less than the incident one. Our results do not show a strong relationship between rebound and impact angles (Fig. 17). A linear regression suggests a weak negative relationship with a low R2 value (0.004). Figures 9 & 10 and Tables 3 & 4 show the large variability in rebound angles within any given run; standard

deviations range from 16.9-31.6°. With that large amount of variability in rebound angles, our results suggest that the relationship between rebound and impact angles highly depends on bed characteristics (i.e., grain packing) and sand grain characteristics (i.e., size and angularity).

Ejection Processes and Splash Functions

When saltons impact the bed, they can rebound and eject other particles. The characteristics of ejecta, splashed particles, are described by the splash function (Ungar & Haff, 1987). New ejecta travel in a wide range of directions and rarely overcome 10% of the impact velocity. Ejecta characteristics reported here align with previous results summarized in Table 1.

Results shown in Figure 16 and Table 5 support previous findings that impact velocity influences splash event ejecta (i.e., higher impact velocity produces more ejecta). Similar to predicting rebounding probability, the number of ejecta is often described by a function limited to a critical velocity below which there are no splashed particles. More specifically, Beladjine et al. (2007) state that the number of splashed particles at a given impact angle increases linearly with the impact speed above a critical velocity:

$$n_{ej} = f_{ej}(\theta_i)[\frac{v_i - v_{i\,critical}}{\sqrt{gd}}] \quad \text{Eq (6)}$$

where $f_{ej}(\theta_i)$ is an increasing function of the impact angle and $v_{i\,critical}$ is the critical velocity below which there are no splashed particles. Werner and Haff (1988) suggest $v_{i\,critical} \approx 20\sqrt{gd}$, but Beladjine et al. (2007) suggest a larger value using $v_{i\,critical} \approx 40\sqrt{gd}$.

Determining the critical velocity for producing splashed particles is an important feature of the splash process. It sets the velocity of the saltating particles in the equilibrium state of transport. When the saltation cloud approaches equilibrium, the net production/increase of splashed particles should stop (Valance et al., 2015). Using Werner and Haff's (1988) equation, the critical impact velocity for our grain size is 1.34 ms^{-1}. As in Equation. 6, many authors incorporate a dependency on the number of splashed particles with the impact angle. Werner and Haff (1988) suggest $f_{ej}(\theta_i) = 3sin(\theta_i)$. Using our mean impact angle (17.45) and mean impact velocity (2.17 ms^{-1}) from the flat bed runs in Equation 6 results in n_{ej} = 11.2 (number of splashed

particles). This is much higher than our empirical n_{ej} values, which ranges from 0.2 to 1.1 for all of our flat and rippled bed runs. Using the suggested critical impact velocity and $f_{ej}(\theta_i)$ equations by Beladjine et al. (2007) produces unrealistic ejecta count estimates because the critical velocity value for our mean grain size would be higher than our mean impact velocity.

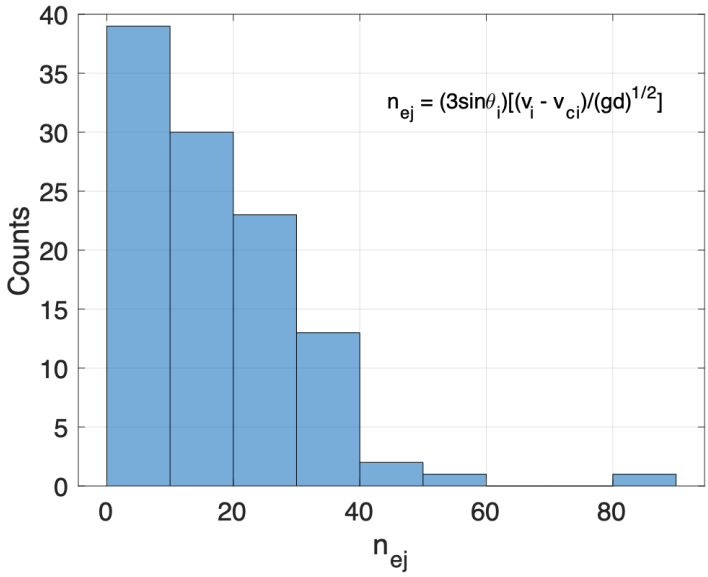

Figure 23: Distributions mean ejecta counts from the flat bed splash events based on Eq. 6 and Werner & Haff's 's functions using v_{i_flat} and θ_{i_flat} distributions.

The differences in ejecta estimates based on different critical impact velocity equations and empirical data reported here suggest the importance of grain characteristics when calibrating models (Fig. 19 compared to Fig. 23). Beladjine et al. (2007) experiment uses 6 mm PVC beds. They use the Froude number ($Fr = \frac{v_i}{\sqrt{gd}}$) the pertinent parameter for characterizing the collision process. Thus, in the collision experiments, they scale their particle velocities (10 to 50 ms^{-1}) to reach Froude numbers for saltating sand grains (50-250). The lack of additional grain characteristics beyond size (i.e., density, plastic response, and angularity) is likely the reason their critical velocity threshold equation and splash function produce unrealistic results for data collected here using saltating sand.

The CDF curves in Figure 19 highlight the frequent occurrence of zero ejecta per splash, the probability ranging from 0.44 to 0.81. While there were large splash events (>=3 newly ejected particles) in most runs, these events were infrequent. Given our 2D analysis and camera position, it is possible that all ejecta were not visible. A 3D analysis or top-down view of the splash event would address this issue but is beyond the scope of this research. Comparing our n_{ej} results to other wind tunnel studies with natural sand suggests our empirical data are accurate, and the estimated n_{ej} from the splash function (Eq. 6) shown in Figure 23 are much too large. Splash functions generated from non-sand experiments do not appear to predict ejection counts accurately. A recent high-speed sand collision experiment by Chen et al. (2019) also suggests that previous results from simulations using alternative materials are quite different from those of sand. Their results also show lower n_{ej} values than Beladjine et al. (2007) and Rice et al. (1995). Valance et al. (2015) state that the splash process is predominantly driven by the transport of momentum rather than energy. Given that particle size and density would affect momentum transfer further suggests splash dynamics for saltation models should be calibrated from aeolian sand saltation simulations. These results imply that current assumptions do not well represent particle-bed interactions and likely overestimate ejecta counts from splash events.

Influence of Ripples on Splash Dynamics

Local Slope

Splash events sustain saltation through conversions of horizontal to vertical grain-borne momentum. Thus, accurate rebound functions that consider ripple morphology and influence are important for saltation numerical models. The relationship between rebound and impact angle remains unclear or weak when examining data from the different aspects (Table 5). Again, we believe this is due to the variability of rebound angles in general. The results here support previous findings that impact angles are generally less than rebound angles, and rebound angles are highly variable. This variability remains for splash events on positive sloping surfaces (stoss).

Comparing the impact angles and nej for each ripple aspect in Table 5, we generally see that the stoss has lower impact angles and larger mean nej. While the impact angles are lower on the ripple stoss, the surface slope itself is positive (~4°), which makes the impact angle larger apparent to the local slope. Yet, Figure 20B shows that the mean impact angle for the distribution of splash events that resulted in ejecta is lower than those that did not. Gordon and McKenna Neuman (2011) report that nej is higher on the positive slopes (stoss) for two of their three saltation runs. However, the standard error of their measurements indicated that the differences were not statistically significant at a 95% confidence level. It remains difficult to determine if the stoss aspect results in a higher amount of ejecta per collision due to changes in local slope or a higher number of collisions relative to the lee slope due to a shadowing effect from the ripple microtopography.

Shadowing Effects

Impact ripples are small features ranging in height from a few millimeters to several centimeters, and few studies have explored the potential of shadowing effects (e.g., Gordon and Mckenna Neuman). Figure 24 shows the percentage impacts per slope aspect normalized by the length of each across the four rippled bed runs (5-8). 40% of the impacts for runs 5-8 (rippled bed runs) occurred on the stoss slope. In contrast, only 10% of impacts occur on the lee slope. The remaining portion of the ripple with no slope (crest and trough) received 50% of the impacts. This significant difference between the stoss and lee supports the theory that shadowing effects occur, focusing particle splashing to the stoss and crest. Even at the small ripple heights observed in this study (0.2-0.3 cm), only particles with higher descending angles can impact the lee, as shown in Table 5.

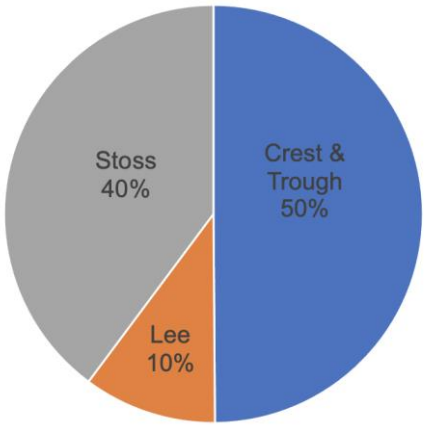

Figure 24: Pie chart showing the percentage of splash events per ripple slope using all data from runs 5-8. Each ripple feature group was normalized by the length percentage it occupies for all datasets.

Gordon and Neuman (2011) provide a schematic demonstrating the shadow effect (Fig. 25). When the average impact angle is much steeper than the average ripple slope, there is no shadowing effect (Fig. 16 A). When the average impact angle is close to or shallower than the average slope, there is a difference between the number of stoss and lee impacts (Fig. 25 B). Our mean impact angles ranged from 14-20° ($-\theta_{im}$ for Fig. 25). Yet, our ripple lee slopes ranged from 8-13°, slightly lower than the mean impact angles. Thus, additional work is needed to confirm how large lee slopes must be to result in notable shadowing effects.

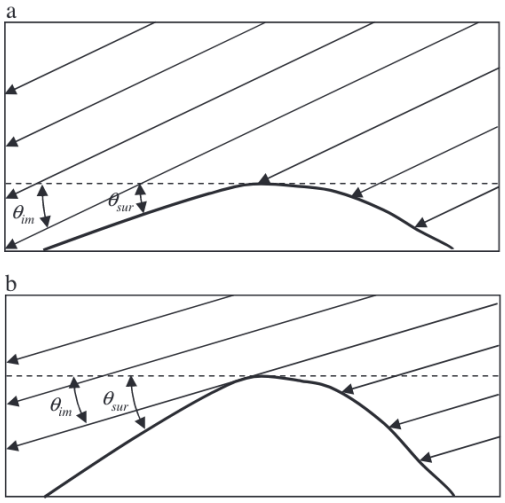

Figure 25: From Gordon and Neuman (2011). A schematic demonstrating the shadow effect with (A) impact angle ($-\theta_{im}$) greater than ripple slope ($-\theta_{sur}$) and (B) impact angle ($-\theta_{im}$) less than ripple slope ($-\theta_{sur}$).

The difference in impact accounts and angles on the lee vs. stoss suggests a shadowing effect is occurring. If shadowing occurs, this potentially affects splash events and functions. As so few high-angle impacts are occurring on the lee, this supports that the range of impact angles is narrow. Recall that some splash functions incorporate impact angle as a variable (Eq. 6). The COMASALT model (Kok & Renno, 2009) does not include the dependence of n_{ej} on the impact angle. They based this decision on several laboratory and modeling studies suggesting that the number of ejected particles scales approximately linearly with the impact speed (Anderson et al., 1987, 1991; McEwan & Willetts, 1991; Rice et al., 1996; Rioual et al., 2000; Oger et al., 2005). Gordon and McKenna Neuman's (2011) results were inconclusive on whether the differences in splash dynamics are due to shadowing and a decrease in the number of collisions on the negative slope, the change in impact angle relative to the surface, or a combination of the two effects. These results suggest shadowing effects might play a more significant influence than local slope, but more analysis is needed.

Conclusions

This chapter reports the characteristics of impact, rebound, and ejecta particles across a range of wind speeds and bedforms from a wind tunnel experiment using HS imagery with manual particle tracking. Given the continued development of numerical models, these empirical results address the need for data to test, validate, and parameterize such models. Though great improvements have been made to automated tracking algorithms, none can accurately associate an impacting salton with its rebound and resulting ejecta from within a saltation cloud. Thus, there is still great utility in manual tracking methods. Our results are summarized as follows:

1. Results for the flat bed runs are comparable to previous findings regarding the mean impact and rebound velocities and angles. With increasing wind speed, we see no significant changes in impact, rebound, and ejecta velocity between the flat and rippled bed runs. The range of CoV values is consistent with previous findings, with mean values between 0.5 and 0.6. We see no significant differences in CoR values between flat and rippled bed data.
2. The probability of zero ejecta per splash event from our flat bed and rippled bed data ranges from 0.44 to 0.81. Most newly ejected particles stayed within 1 cm of the bed. Though infrequent, large splash events are seen in most runs, i.e., >=3 newly ejected particles.
3. For the flat bed runs, impact velocity distributions are the most different (angle vs. COR) when comparing splash with eject vs. no ejecta. For rippled bed runs, impact velocity, and angle distributions show differences in impacts with splash vs. no splash. The rippled bed data showed differences in impact angles and mean ejecta with changes in local slope (stoss vs. lee).
4. Our impact location counts suggest that ripples produce shadowing effects that influence splash dynamics.

Results suggest that the splash dynamics of saltation differ from studies using differing grain materials (e.g., not sand) (Chen et al., 2019), flattened beds (both active and static), and

individual collision experiments (e.g., lacking a transport-limited saltation cloud. Generally, the mean number of ejecta per collision is larger on the stoss slope, but further analysis is needed to confirm a significant difference. Our results suggest that even small impact ripples with gentle slopes can produce shadowing. Separating the influence of impact angle vs. shadowing effect remains difficult but may be possible in future efforts.

Saltation and the splash process are linked to the creation of ripples and dunes, the emission of dust aerosols, and the propagation of land degradation and desertification. The description of the splash process is a crucial ingredient for theoretical and numerical approaches and bedform migration theory. Collecting representative empirical data on the process has been difficult due to the high percentage of sand concentration near the bed at higher wind speeds, the complexity that rippled bedforms add, and the time-intensive manual digitization of grain trajectories when automated methods are not viable. Future efforts will incorporate multi-camera (view) systems and 3-D surface point clouds of the rippled bed to examine 3D particle dynamics along and bedform migration in further quantifying the saltation cloud, creeping/reptating particles, and bed surface interactions.

Supplemental Figures

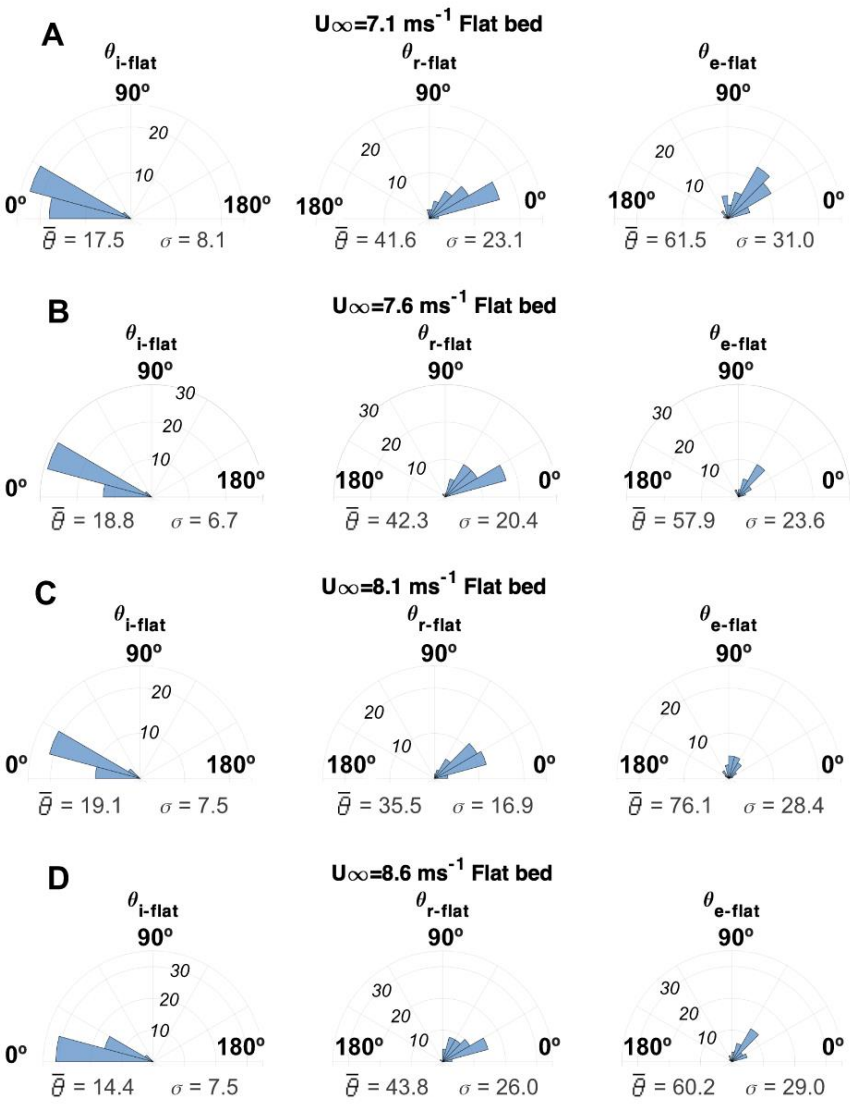

Figure 26: Polar histograms of particle angles ($\theta_{i,r,e}$) for the flat bed runs 1-4 (U_∞ = 7.1 to 8.6 ms^{-1}). all use a bin width of 15°.

SIMULTANEOUS, NEAR BED FLUID-PARTICLE MEASUREMENTS FROM PIV/PTV: TURBULENCE CHARACTERISTICS WITHIN A SALTATION CLOUD

Introduction

Aeolian (windblown) sand transport shapes terrestrial and extraterrestrial surfaces, and aeolian processes influence a wide variety of environments, from coasts to inland deserts to agricultural fields. As sand is eroded, deposited, and transported, landscapes are altered. The quantification and prediction of sand movement throughout Earth systems are vital for many professions, such as biologists, engineers, city planners, military personnel, and health practitioners (Guo et al., 2014). As anthropogenic, geologic, and climatic forcings shape our coasts, deserts, rivers, floodplains, and other sedimentary environments, we require accurate sand transport models to understand these dynamic systems.

The mechanics and quantification of sand transport are key to understanding and modeling the dynamics of sedimentary environments. Bagnold (1936) derived the first physical aeolian model based on the observations that saltation is the dominant mode of transport and grains travel in ballistic trajectories. Almost all physics-based models predict sand transport rates as a function of the second or third power of shear velocity (e.g., Bagnold, 1941; Zingg, 1952; Kawamura, 1951; Lettau & Lettau, 1978). A persistent problem is that the most frequently used sand transport equations produce significant differences between predicted and observed transport rates, with upwards of 300% error within a single model (Sherman et al., 2013; Sherman, 2020). Deviations of this magnitude justify reexamining the fundamental physical aeolian processes that make up the foundation for commonly used models.

The development of aeolian sand transport models has relied heavily on boundary-layer theory (e.g., Bauer 2013). The boundary layer is the flow field region close to the surface where deformation is apparent (Prandtl, 1932). In turbulent flow, the mean velocity (u_z) varies logarithmically with height (z) until it reaches approximately the free stream velocity (Eq. 1, where k is von Karman constant, u_* is shear velocity, and z_0 is roughness length). The thickness of the

boundary layer increases with downstream distance as it comes into equilibrium with the underlying bottom roughness. As wind speed increases, the boundary layer height decreases. A thinner boundary layer (from faster wind speeds) implies that fluid stresses are distributed through a smaller region, and therefore flow deformation is more concentrated near the bed. Fluid shear stress is responsible for initiating sediment transport. Though shear stress cannot be measured directly, it can be estimated from shear velocity (Eq. 2).

$$\overline{u_z} = \frac{u_*}{k} \ln\left(\frac{z}{z_0}\right) \quad \text{Eq. 1}$$

$$\tau = u_*^2 \times \rho \quad \text{Eq. 2}$$

It is standard practice to derive the shear velocity from the slope of velocity profile from the lower 10-15% of the boundary layer, ($\overline{u_z}$) (Bauer et al. 2004), and then estimate the mass transport rate as some function of shear velocity (Bagnold, 1936; Kawamura, 1951; Lettau & Lettau, 1978) (Fig. 6). When the boundary-layer flow becomes saturated with saltating particles, wind tunnel measurements demonstrate an upward convexity in profiles of $\overline{u_z}$ that is attributed to a loss of momentum from the fluid to particles moving near the bed (McKenna Neuman & Nickling, 1994; Bauer et al., 2004). Sand concentration within the saltation cloud increases rapidly toward the bed surface resulting in a decline in the fluid's momentum. When the wind profile is modified by momentum exchanges between the fluid and saltating particles, it is challenging to predict sand transport using the conventional velocity profile methods. Thus, deriving, and interpreting wind shear velocity from the Law of the Wall principles becomes difficult.

Multiple issues have limited the development of a more accurate understanding of the saltation cloud. First, traditional wind and sand instruments (e.g., cup or ultrasonic anemometers, acoustic, piezoelectric, or laser particle counters) are typically bulky and intrusive, often disturbing existing wind and saltation motions, obscuring measurements. Secondly, these instruments often only provide single-point observations of sand or wind characteristics which can vary spatially. Previous studies often only include a small range of wind speeds and transport rates. Additionally, previous studies on the near-bed saltation process often neglected the turbulent characteristics of the wind, assuming that the movement of these particles is not affected by the

turbulent structure of the oncoming wind. Lastly, the design of some previous experiments would result in under-saturated saltation cloud conditions (i.e., supply-limited). To our knowledge, no previous work addresses all these issues. Thus, additional empirical data are needed to address previous design issues and knowledge gaps.

Recent efforts have examined how fluid stress within the saltation cloud relates to the turbulent Reynolds stress (RS) (e.g., Zhang et al., 2008; Li & McKenna Neuman, 2012). Though Li & McKenna Neuman (2012) use a quadrant analysis, previous studies have not calculated flow exuberance to link difference turbulence intensities and RS with increasing saltation. Specifically, exuberance calculations characterize the ratio of turbulent burst-sweep events (contribution to sand entrainment) to inward and outward interactions (are not known to increase flux). Thus, flow exuberance provides insight as to whether turbulence fluctuations are contributing to RS production and resultant transport or if sand transport may be increasing flow turbulence.

There is a well-established positive relationship between sand transport and wind strength. In addition to increases in freestream, increases in turbulence or “gusts” has been shown to correspond to increased sand transport in field observation. For example, Baas and van den Berg’s (2018) fieldwork suggests a correlation between turbulent eddies that scale in size to streamers in the saltation process. Due to previous data limitations, quantifying near-bed, sub-second time-scale correlations between fluid characteristics and sand concentrations have not been examined.

Compared to the traditional instrument described above, high-speed camera systems are an alternative solution to some of the issues that traditional anemometers and particle counters pose. Motion film photography with manual particle identification and tracking has been used since White and Shultz (1977). Nevertheless, experimental observation of sand particles within a fully saturated saltation cloud remains challenging due to inadequate lighting, difficulties with surface detection, and a high degree of error associated with particle detection and trajectory identification.

In recent decades, instrumentation progress has improved the capabilities of laboratory imaging and tracking velocimetry techniques for more accurately characterizing transport within the aeolian saltation layer (Dong et al., 2004; Dong & Wang, 2004; Rasmussen & Sørensen, 2008; Creyssels et al., 2009; Zhang et al., 2008; Wang et al., 2008; Beladjine et al., 2007). Deploying small seeding particles (μm diameter scale) during experimental runs allows Particle image velocimetry (PIV) analysis to measure the fluid velocity field. Particle Tracking Velocimetry (PTV) methods are ideal for sand tracking. Grain paths are recorded with a high-speed (HS) camera as they pass through a light sheet. Detected grains are then linked across sequential frames to produce a record of the grain's trajectory during the sampling period. Combining PIV and PTV techniques allows the velocity fields of the wind and the dispersed sand particles to be measured simultaneously over a spatially continuous volume near the bed.

Objectives

This study employs PIV/PTV methods to examine the turbulence characteristics of a boundary layer flow with increasing amounts of saltating sand particles. The research objectives include: 1) confirming the success of our PIV/PTV empirical data via volumetric flux estimates and wind velocity profiles, 2) quantifying changing fluid characteristics with increases in sand transport, specifically turbulence characteristics and contributions to Reynolds stress (RS) generation, and 3) use cross-correlation analysis to explore relationships between near bed instantaneous fluid velocities and sand concentrations.

Methods

Wind Tunnel Facility

The experiments were conducted in the Planetary Geology Wind Tunnel at Arizona State University (Greeley et al., 1983; Williams, 1987; Greeley, 2002). Natural, well-sorted, medium-sized quartz sand was used for all experiments (mean diameter of 456 microns). The tunnel instrumentation included a high-speed imaging system for PTV/PIV analysis and an RM Young

Ultrasonic Anemometer Model 81000. The same experimental design described in Chapters 1 and 2 was used here with the addition of 3M™ Glass Bubbles K1 for fluid seeding. The glass spheres have an average density of 0.125 gcc^{-1} and a diameter of 65 microns. The seeding material was deposited on the bed 1 m upwind of the imaging area and allowed to release and disperse throughout the flow naturally. For runs with wind speeds above 8.0 ms^{-1}, a sled was used to cover (protect) the seed material until 1 second before imaging began, which then was pulled away to allow seed dispersion. These neutral buoyant particles are visible (along with sand particles) as they pass through the laser sheet.

Experimental Design

Table 1 shows the six different experimental runs reported in this study. Runs were conducted on 5/25 and 6/03/2021. For each day of the experiment, the temperature and humidity varied very little between runs (from 91-95°F and 7-8% on 5/25 and 105-107°F and 10-11% on 6/02). The tunnel freestream wind speed ranged from 6.0 to 9.6 ms^{-1}. This range was selected to include wind conditions just below and above the fluid threshold. Thus, datasets range from no transport up to higher transport rates. Table 1 reports the free stream velocity (U) calculated from 10 seconds of data from the 3Dsonic anemometer, the Reynolds number (Re), shear velocity (u_*), boundary layer depth (δ), volumetric flux rate (Q), and the run duration. Boundary layer depth (δ) is estimated using Equation 3, and the Reynolds number (Re) is calculated using Equation 4.

$$\delta = \frac{0.38x}{(\rho Ux/\mu)^{1/5}} \quad \text{Eq. 3}$$

$$Re = \frac{U\delta}{\nu} \quad \text{Eq. 4}$$

where x is the downstream distance to the imaging location (9,5m), ρ is fluid density (1.2 kgm^{-3}), μ is dynamic viscosity, and ν is kinematic viscosity ($\mu = \rho\nu$ and $\nu = 1.5 * 10^{-5}\ m^2 s^{-1}$). All runs have turbulent flows.

$$u_* = k/m \quad \text{Eq. 5}$$

Table 1: Six experimental runs varying in wind speed. Re (Reynolds number, Eq. 4), u* (shear velocity, Eq. 5), δ (boundary layer thickness, Eq. 3)), q_{vol_total} (total volumetric flux, Eq. 14). † Sample size was decreased due to data corruption during transfer.

Run	U ms^{-1}	Re $(\times 10^4)$	u_* ms^{-1}	δ m	$q_{vol_{total}}$ m^2s^{-1}	Bed condition	Duration min
1	6.0	7.0	0.30	0.17	7.0E-05	Active, Flat	4.5
2	6.3	7.3	0.36	0.17	5.4E-05	Active, Flat	2.4†
3	7.0	7.9	0.46	0.17	4.1E-04	Active, Flat	4.5
4	8.1	8.9	0.53	0.16	9.8E-04	Active, Flat	2.4†
5	9.0	9.6	0.64	0.16	6.5E-03	Active, Flat	4.5
6	9.6	10	0.71	0.16	7.0E-05	Active, Flat	4.5

Figure 1 provides an example of a typical run. Once the tunnel started, sand trickled into a feeder that entered the working section. The boundary layer was developed after approximately 10s; then, we waited for an additional 10s to confirm that the wind flow and saltation cloud had equilibrated. Figure 1 shows that the flow reached a stationary temporal average. Previous papers suggest that the saltation cloud typically adjusts within 1 s of changing wind conditions. Thus, ten seconds was assumed to be sufficient to reach equilibrated conditions.

3D sonic anemometer data from the final 10 seconds of the run (30 seconds from the start of the tunnel) was used to define mean freestream wind velocity. During this time, approximately 4.5 s of HS imagery from the camera system was also collected (Fig. 1). A deposit of seeding particles 1 m upwind of the measurement section in the tunnel was then dispersed into the flow by removing a sled cover just before imaging. This allowed seeding material to be dispersed throughout the imaging volume while remaining highly concentrated, both spatial and temporally.

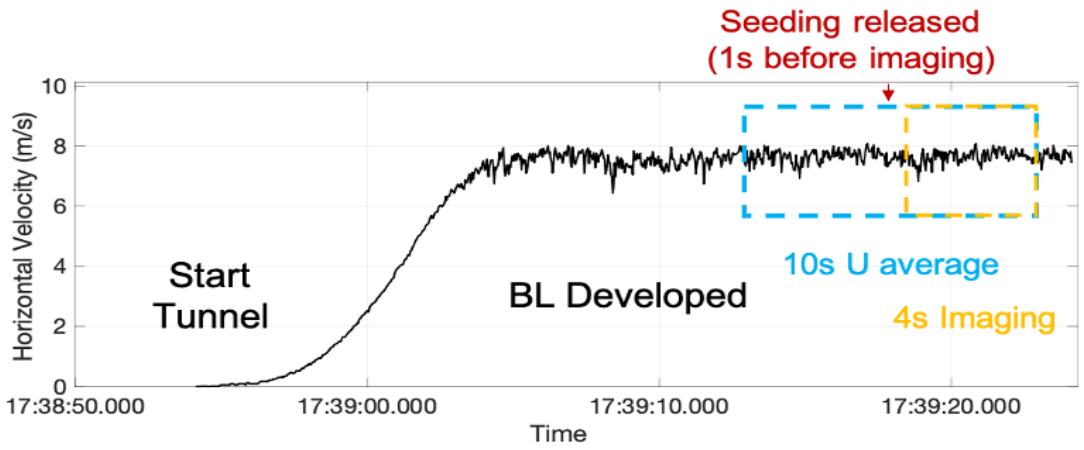

Figure 1: 3D sonic anemometer data from an example run. Once the wind tunnel is turned on, it takes about 10-20s for the boundary layer and saltation clouds to develop and reach a steady state. Ten-second averages are used to calculate the mean U from the 3D anemometer (blue box). Imagery collected for ~4.5 seconds (yellow box). Fluid seeding was released just prior to imaging by removing the sled.

Preprocessing of the HS imagery was necessary prior to PIV/PTV analysis. First, an object detection script was applied to detect larger sand grains (compared to seeding grains). In each frame, sand grains were detected based on size, and everything other than the sand particles was removed via a mask. These output images were used for the PTV sand tracking. The script was run a second time on the original images, but the mask was applied to the sand grains on the second itineration. This second stack of output images included only seeding particles and was used for the PIV analysis. This two-step preprocessing greatly improved both our PTV and PIV algorithms' success.

PTV

Particle trajectories were generated from an automated tracking algorithm called TrackMate in FIJI/ImageJ (Tinevez et al., 2017). The PTV algorithm uses a Laplacian Gaussian detector with an estimated object diameter (12 pixels), quality threshold (15), a pre-process median filter, and sub-pixel localization. Next, a Simple LAP tracker was used to track the

detected objects with a linking distance of 55 pixels, a gap-closing max distance of 55 pixels, and a gap-closing frame of 2. A post-tracking filter was applied to remove low-quality tracks based on the number of detected objects in a track (i.e., a track must include a minimum of 4 spots), similar to the approach of O'Brien & Mckenna Neuman (2016). The results were exported as XML files for further analysis in MATLAB.

PIV

We developed a PIV Python algorithm using the OpenCV library (Bradski, 2000) to characterize fluid motions via the seeding particle movements observed via HS imagery. The algorithm performed a cross-correlation of the pixels of the same small interrogation area of two consecutive frames (e.g., Yager & Schmeeckle, 2013). The cross-correlation of these two integration areas is very effectively calculated by fast Fourier transforming (FFT) both areas, multiplying the transformation of one of the areas by the complex conjugate of the other, and then performing an inverse FFT the peak value in the cross-correlation field gives an average pixel shift of the particles in the interrogation area. The window size was 64x64 pixels with 30-pixel spacing between windows. Additional post-processing of the PIV data was required. In particle image velocimetry (PIV), outlier vectors exhibit large unphysical variations in magnitude and direction from neighboring valid vectors. A common approach for removing outliers is based on statistical data analysis (Westerweel, 1994). Here, the u- and v-velocities below the 10th and above the 90th percentile are removed via a mask. Matching masks were applied to both u- and v-velocity datasets.

Fluid Characterization

PIV results allow the quantification of turbulence characteristics and fluid stresses throughout the transport layer and saltation cloud. Figure 2 shows the Reynolds decomposition method to convert instantaneous velocity values ($u\ and\ v$) into deviation components ($u'and\ v'$) about their respective mean values ($\bar{u}\ and\ \bar{v}$). Equations 6 and 7 are the equations from Figure 2 rearranged to solve for the fluctuating component. Note that we differentiate between the mean

velocity at a given height and the freestream mean velocity. Figure 6 shows the mean values ($\bar{u}$) for each PIV window for runs 1-6 with increasing freestream velocities (U).

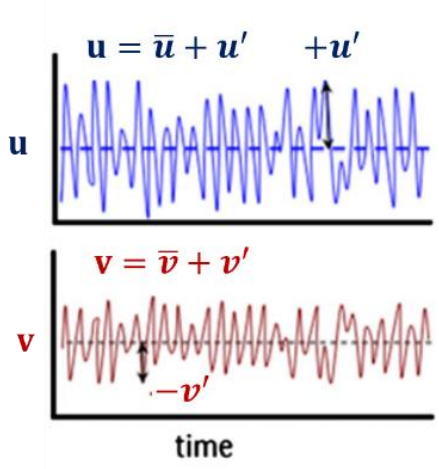

Figure 2: Turbulent velocity time series components plotted as quasi-instantaneous u′ and v′ (modified from Chapman et al. 2012)

$$u' = (u - \bar{u}) \quad \text{Eq. 6}$$

$$v' = (v - \bar{v}) \quad \text{Eq. 7}$$

The root-mean-square of turbulent velocity fluctuations (u′ and v′) and the cross-moment (u′ w′) can then be calculated using equations 8-10. Here the horizontal and vertical turbulence intensities and RS term are normalized using the freestream velocity calculated from the 3D sonic anemometer. dimensionless vertical turbulence intensity

$$\text{dimensionless vertical turbulence intensity} = \frac{\sqrt{v'^2}}{U} \quad \text{Eq. 8}$$

$$\text{dimensionless horizontal turbulence intensity} = \frac{\sqrt{u'^2}}{U} \quad \text{Eq. 9}$$

$$\text{dimensionless RS} = \frac{\sqrt{u'v'}}{U} \quad \text{Eq. 10}$$

RS signals can be decomposed into four categorical ‘events’ by quadrants. Figure 3 shows the four event types: quadrant 1 (Q1) outward interactions ($u' > 0, v' > 0$), quadrant 2 (Q2) ejections ($u' < 0, v' > 0$), quadrant 3 (Q3) inward interactions ($u' < 0, v' < 0$), and quadrant 4

(Q4) sweeps ($u' > 0, v' < 0$). Both ejections and sweeps (Q2 and Q4) contribute positively to RS generation.

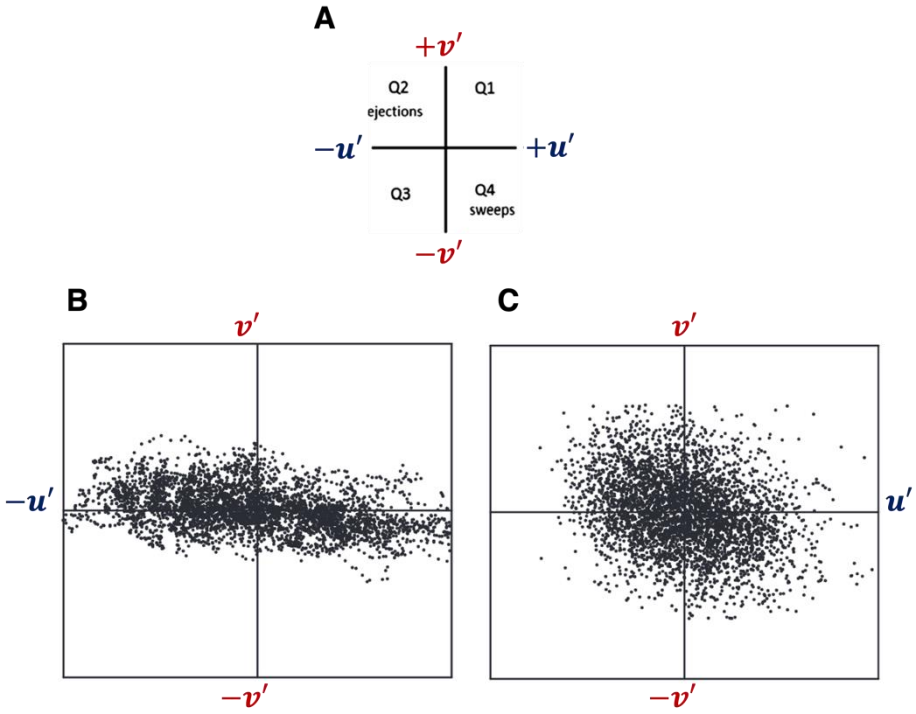

Figure 3: (A) Quadrant analysis of fluctuating velocity components. Q2 ejection and Q4 sweep event activity typically dominate the Reynolds stress signal. (B)Example of Q2 and Q4 dominance and EX_{FL} approaching 0. (C) Example of equal Q1-Q4 contributions and EX_{FL} approaching -1. Data are not from this study, for example only.

Flow exuberance (EX_{FL}) describes the shape of the quadrant frequency distribution using the ratio of Q1 and Q3 to Q2 and Q4 Reynolds stresses (Shaw et al., 1983) (Fig. 3A). EX_{FL} is the ratio of the negative to positive contributions to RS generation (Eq. 11). For example, Figure 3C shows that when the ratio is close to one, the distribution of fluid stress events is occurring in all four quadrants. Exuberance values approaching zero indicate the dominance of Q2 ejection and Q4 sweep activity, which results in increasing shearing flows (Fig. 3B).

$$EX_{FL} = \frac{Q_1+Q_3}{Q_2+Q_4} \qquad \text{Eq. 11}$$

Lastly, Equation 12 calculates the coefficient of variation of the u-velocity distributions. This ratio highlights the amount of variance (turbulence) compared to the mean of the distribution.

$$CoV = \frac{\sigma}{\bar{u}} \quad \text{Eq. 12}$$

Results

Validation of PTV Methods

To our knowledge, only one previous experiment used PIV/PTV to simultaneously measure fluid characteristics and sand transport due to difficulty differentiating sand and seed particles at high concentrations near the bed. Chapter 1 highlights the success of the sand tracking algorithm compared to manual tracking. To validate our PTV-derived sand tracks from runs with fluid seeding, we compare the volumetric flux profiles to runs of comparable wind speeds from Chapter 1 (without fluid seeding). Volumetric flux (q_{vol}) is calculated for each bin using Equation 13, where v_s is the grain volume (0.05 cm^3), v_b is the bin volume (0.33 cm^3) z_b is the bin height (0.2 cm), and the sampling period is listed in Table 1 (refer to Chapter 2, Fig. 5 for particle edge vs. track definition). Table 1 reports the depth-integrated volumetric flux (q_{vol_total}) per run using Equation 14.

$$q_{vol} = \frac{sum(edge\ displacement) \times v_s}{v_b \times t} \quad \text{Eq. 13}$$

$$q_{vol\_total} = \sum(q_{vol} \times z_b) \quad \text{Eq. 14}$$

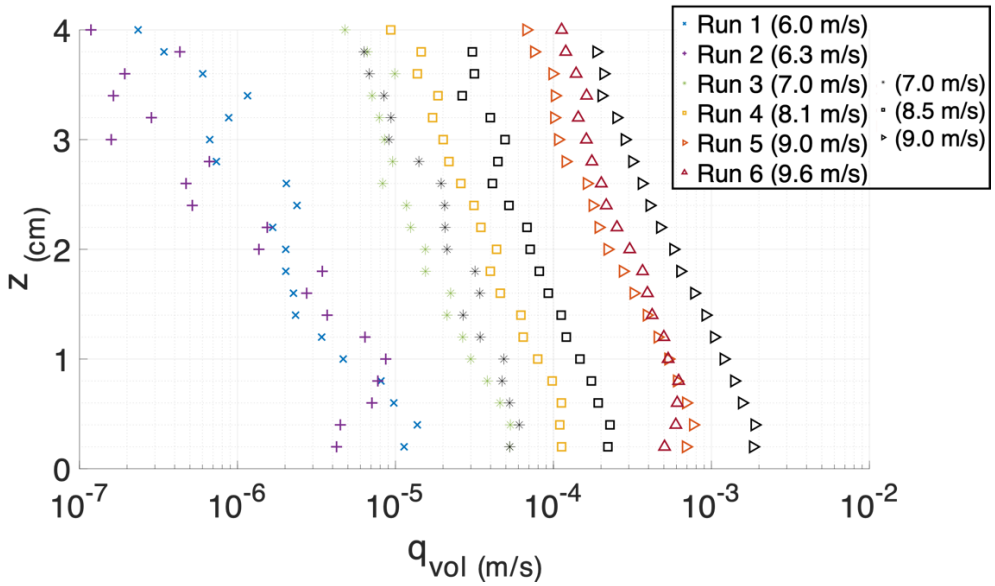

Figure 4: Height versus volumetric flux for runs 1-6. The q_{vol} is estimated using Equation 13 and results from the PTV tracking algorithm. Three additional runs from Chapter 1 are included to compare the PTV algorithm success between imagery from the seeded flat bed runs (1-6) to non-seeded runs from Chapter 1. Data from Chapter 1 is shown by black symbols, which correspond to runs with similar freestream.

The open-source PTV package TrackMate (Tinevez et al., 2017) successfully tracked sand particles for the current experimental design, including adding fluid seeding particles. The volumetric flux profiles in Figure 4 follow the expected exponential decay with increasing height (for further discussion, see Chapter 1) and positive relationship with increasing U. Note that smaller grain count sample sizes correspond to slower wind speed runs, and this results in increased volumetric flux variability within a single profile (i.e., runs 1 and 2 (U <7.0 ms^{-1}) in Fig. 4). Previous studies report that a higher percentage of sand transport occurs in the transport layer. From these experiments, the total percentage of volumetric flux from the transport layer for runs 1-6 ranged from 44-68%.

Three volumetric flux profiles from the previous experiment (Chapter 1) are shown in Figure 4. These runs were selected for comparison of runs 3-5 and assessment of the PTV success on the seeding-masked pre-processed images. Recall that in this experiment, fluid seeding was removed by the object detection algorithm. The three flux profiles from Chapter 1 are slightly higher than the comparable seeded-PTV flux profiles (U of 7.0-9.0 ms^{-1}). The difference may be due to a combination of sources. First, difficulties in sand grain tracking remain with increased concentration. Thus, there may be an increased potential for error for higher freestreams and sand transport runs. Secondly, it is possible that the object detection mask incorrectly removed some sand particles in addition to seeding material. Lastly, as shown in Chapter 1, particle concentration becomes over-dispersed with increasing wind speed. Thus, volumetric flux estimates could also show increased variability with increasing wind. This could be sample size dependent. More work is needed to explore this potential explanation of flux variability from similar wind speed conditions. Thus, all three of these issues could contribute to the difference seen in Figure 4. However, given the small differences (within an order of magnitude) that are spatial consistent (not biased towards the bed or upper portion of the profile), the PTV results are reliable for the given objectives.

PIV Results

Figure 5 shows the 2D time-averaged u-velocities across the imaging area for runs 1-6. The y-axis is the vertical height, and the x-axis is the horizontal length. The 3D sonic collected data 15 cm above the bed to characterize the freestream velocity. The PIV imaging area was much closer to the bed. Note that the u-velocity at the top of each PIV-derived 2D mean velocity figure does not reach the freestream velocity of the run (e.g., it is slower). This was expected since the imaging height (~4 cm) should be within the log-linear layer and below the freestream height.

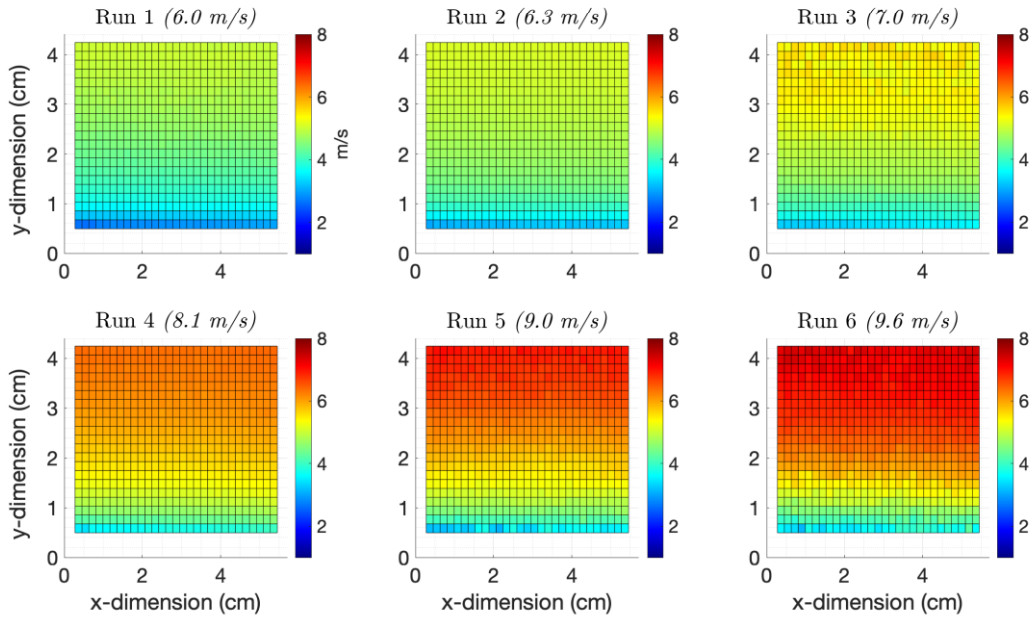

Figure 5: Mean u-velocities from PIV for runs 1-6 (flat bed). The y-axis is the vertical height, x-axis is the horizontal length, and the same color bar scale is used for each.

The vertical profiles shown in Figure 6 were generated from the horizontal center of the PIV u-velocity array shown in Figure 5. To further validate the PIV results, Figure 6 includes the mean velocity from the 3D sonic anemometer, measured at 15 cm. A good fit exists between the mean PIV u-velocities above 2 cm and the mean u-velocities from the anemometer. At 15 cm, data are from the top of the boundary layer and have effectively reached freestream velocities. Thus, the mean velocity from the anemometer should be larger than all PIV results. The slopes of the linear regressions in Figure 6 were used to calculate shear velocity (Eq. 5 and Table 1). Comparing runs 1 through 6 in Figures 5 and 6 shows a steady increase in shear velocity with freestream velocity.

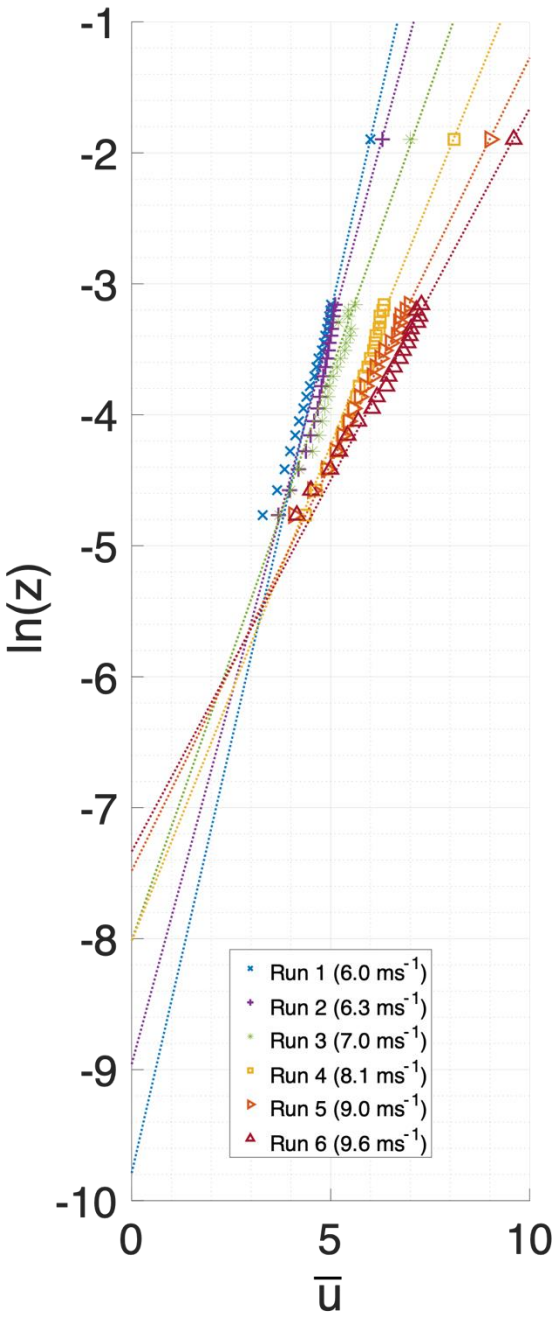

Figure 6: Vertical profiles of mean u-velocity combining PIV data (>=4 cm) and 3D sonic anemometer (15 cm. Linear regression based on all data above 2 cm. Regression slope used to estimate shear velocity (Eq. 5 and Table 1).

Sand-Fluid Interaction: Momentum Exchanges

Figure 7 shows volumetric flux profiles and horizontal wind velocity profiles for runs 1-6 up to ~4 cm ($0.25z/\delta$). The transport layer seems to reach $0.06z/\delta$ based on where volumetric flux begins to decrease. Generally, at low wind speeds, with minimal or no sand transport, vertical profiles of u-velocity will follow the logarithmic law of the wall (Bauer et al., 2004). As seen in Figure 7 for runs 1-3 ($U<=7.0ms^{-1}$), with increasing wind speed profiles without sand transport will have increased shear stress due to increased profile deformation near the bed runs (1-3). Figure 7 also shows the influence of sand in transport for runs 4-6 ($U>=8.0ms^{-1}$). Due to increased sand concentration, the u-velocities dramatically decrease near the bed for runs 5 and 6. As others have shown (e.g., McKenna Neuman and Nickling, 1994; Bauer et al., 2004), saltation extracts momentum from the fluid, so much so that the profiles do not follow the law of the wall within the transport region. Thus, increases in freestream velocity correspond with decreases in near-bed mean u-velocity due to the increased sand flux.

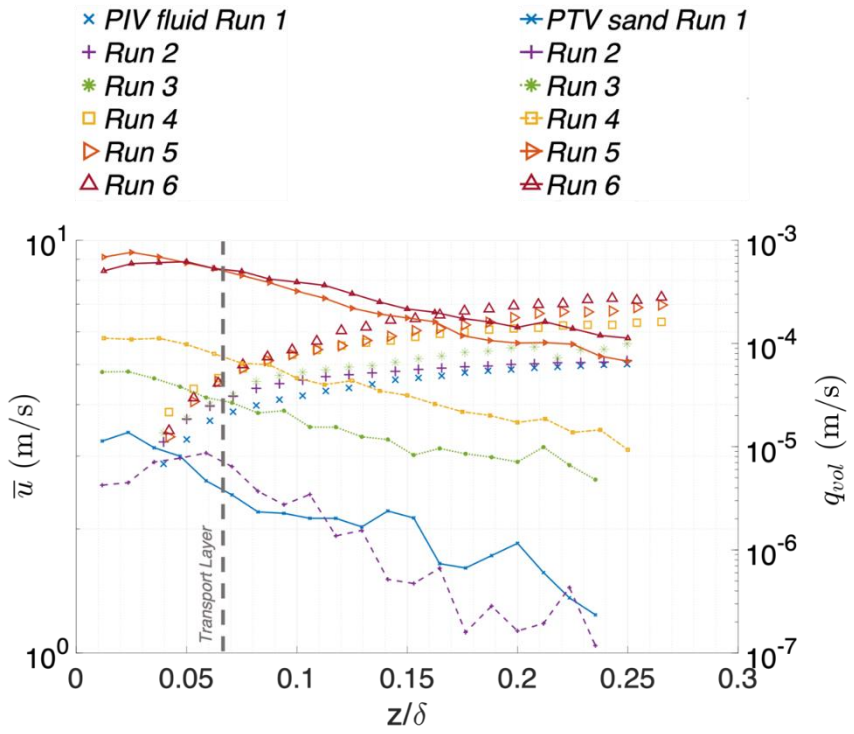

Figure 7: The left y-axis shows mean u-velocity versus height for runs 1-6. The right y-axis shows volumetric flux versus height. Height given in dimensionless form as z/δ ($\delta\ calcuated\ from\ Eq.3$). There is a negative relationship between near bed u-velocity and sand concentration due to momentum extraction by moving sand grains.

Sand-Fluid Interaction: Turbulence Statistics

Vertical profiles of the dimensionless u- and v-turbulence intensity, dimensionless RS, flow exuberance, and coefficient of variation for runs 1-8 are shown in Figure 8. Results on turbulent intensities and RS are consistent with most findings from wind tunnel studies (e.g., Krogstadt and Antonia, 1999; Zhang et al., 2008; Li & Neuman, 2012). The addition of flow exuberance and coefficient of variation further support our findings that near-bed turbulence is associated with increased flux but does not result in increased production of RS.

Figure 8A shows that the dimensionless v-turbulence intensities increase with wind speed. As seen in runs 1-3 with lower wind speeds (U<=7.0 ms^{-1}) (with limited sand transport), the v-turbulence intensities below z/δ= 0.09 remain between 0.040 and 0.055. Above this height,

the v-turbulence intensities for runs 1-3 start to decrease with height. Runs 5 and 6 have higher wind speeds (U>=9.0 ms^{-1}) and increased saltation. These v-turbulence intensity profiles are still highest near the bed but are not constant within the transport layer. The profiles for run 5 and 6 decrease dramatically with height throughout the transport layer. Above the transport layer ($z/\delta \approx 0.1$), v-turbulence intensities continue to decrease but more gradually with height.

Figure 8B shows the u-turbulence intensities relative to freestream velocities. The u-turbulence intensities also increase with wind speed. All profiles near the bed (runs 1-6) have larger values than v-turbulence intensities (Fig. 8B versus A). For runs 1-3 (U<=7.0ms), there is a semi-constant, negative linear relationship between u-turbulence intensities and height. Runs 5 and 6 (U>=9.0 ms^{-1}) have high u-turbulence intensities closest to the bed. Both profiles strongly decrease with height throughout the transport layer but slow their decline above $z/\delta \approx 0.15$.

Regarding u- and v-turbulence intensities, our findings match the results reported by Zhang et al. (2008). Our run 4 (U of 8.0ms-1) corresponds with their single experiment run (U=8.0ms-1). Nearest the bed, they report a T_u (horizontal turbulence intensities) of 12%. T_u is u-turbulence intensity x 100%. The equivalent Tu for run 4 nearest the bed is 11% (Fig. 8B). The overall trends between turbulence intensities and height for sand-laden runs also match, with the highest values near the bed that decrease with height through the transport layer. Li & McKenna Neumann (2012) also report that turbulence intensities increase with sand flux in the near-bed region.

In general, Figure 8 A&B suggests turbulence intensities increase with both wind speed and sand concentration. The v-turbulence intensities appear more influenced than the u-turbulence intensities. In contrast, the normalized Reynolds stress profiles show increases with wind speed but decrease with sand concentration (Fig. 8C). This is visible both in height and across runs because sand concentration increases approaching the bed and across runs 1-6). The sand-laden runs (4-6) compared to minimal sand transport runs (1-3) show lower Reynolds stress within the transport layer but large increases above it ($z/\delta \approx 0.07$). This finding is

inconsistent with Li & McKenna Neumann (2012), that state dimensionless Reynolds stress increases with the mass transport rate in the near-bed region.

The coefficient of variation (Fig. 8 D) is calculated using Equation 12. The profile trends are like those seen in u- and v- turbulence intensity profiles, increasing with freestream and decreasing with height. Closest to the bed, the ratio is much larger for sand-laden runs compared to runs with minimal or no transport. The EX_{FL} profiles are shown in Figure 8E. Runs 1-6 are all roughly between -0.5 and -0.3 above z/$\delta \approx 0.07$. Within the transport layer, runs with increased saltation (4-6) trend closer to -1 approaching the bed, which produces a convex-up shape. As expected, EX_{FL} values closer to 0 correspond with higher RS.

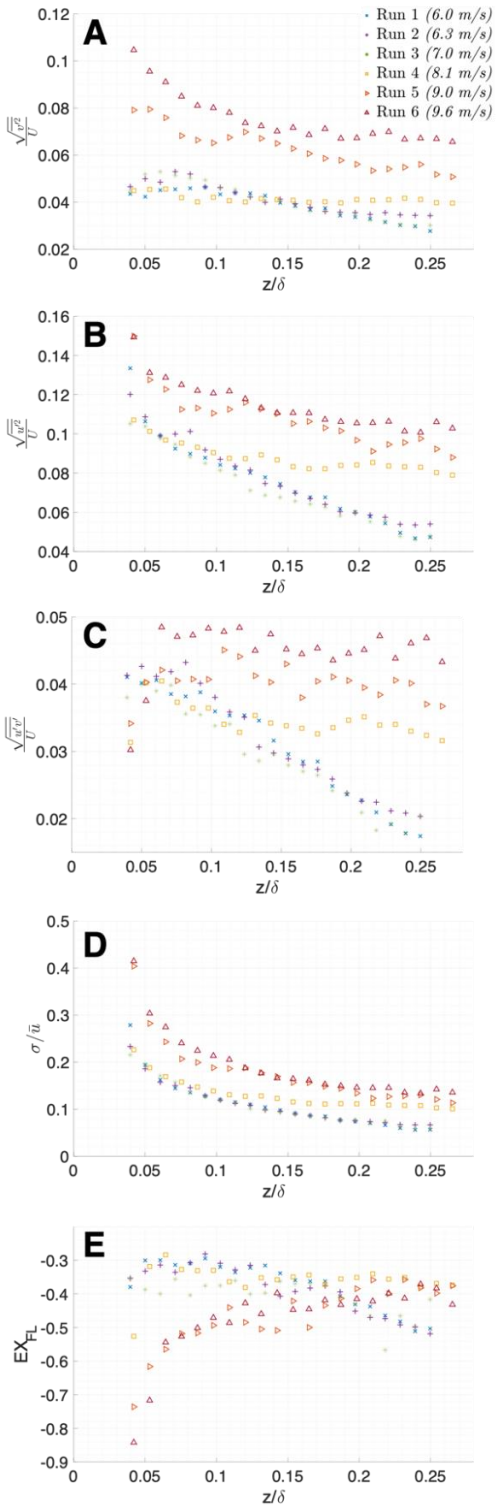

Figure 8: Runs 1-6 profiles of (a) dimensionless v-turbulent intensities (Eq. 8), (b) dimensionless u-turbulent intensities (Eq. 9), (c) dimensionless Reynolds stress (Eq. 10), (d) coefficient of

variation (Eq. 12), and (e) flow exuberance (Eq. 11). The x-axis is the height normalized by the boundary layer depth.

Temporal Correlations

Cross-correlation measures the similarity of two series as a function of the displacement of one relative to the other. Here cross-correlation analysis is used on the near-bed u-velocities and sand grains in motion (counts per frame) to quantify the near-bed relationship between instantaneous fluid velocity and sand concentrations at the sub-second timescale. Lag (time) shifts with values close to 1 or -1 suggest a strong relationship between the two series. Figure 9 shows the cross-correlation between fluid velocities from 0.8 cm and grain counts from run 6. All values are extremely small (~0), suggesting no detectable relationship between the two variables at any time shift.

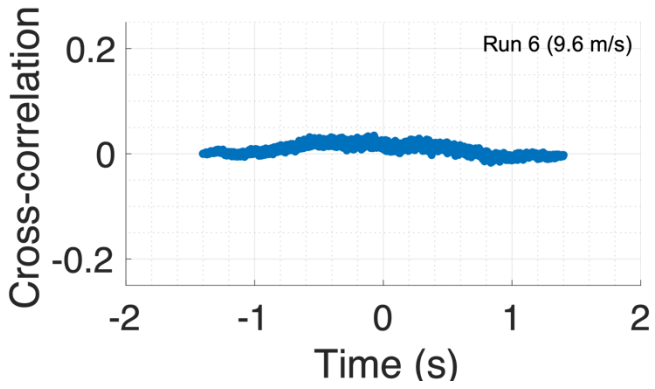

Figure 9: Cross-correlation time-series for run 6 between sand grain counts per frame and near-bed (0.8 cm) u-velocity. For all lag shift, the cross-correlation values are extremely small suggesting no detectable relationship at the given temporal resolution.

The correlation coefficient (R) at various heights above the bed for runs 3, 5, and 6 was calculated (Fig. 10) to confirm the lack of correlation between fluid characteristics and sand concentration at the sub-second timescale. Again, the correlation coefficient is a statistical measure of the strength of a linear relationship between two variables and ranges from -1 to 1.

Like the results in Figure 9, there is no detectable relationship between the fluid u-velocities and sand concentrations at the sub-second timescale from ~4.5 seconds of data.

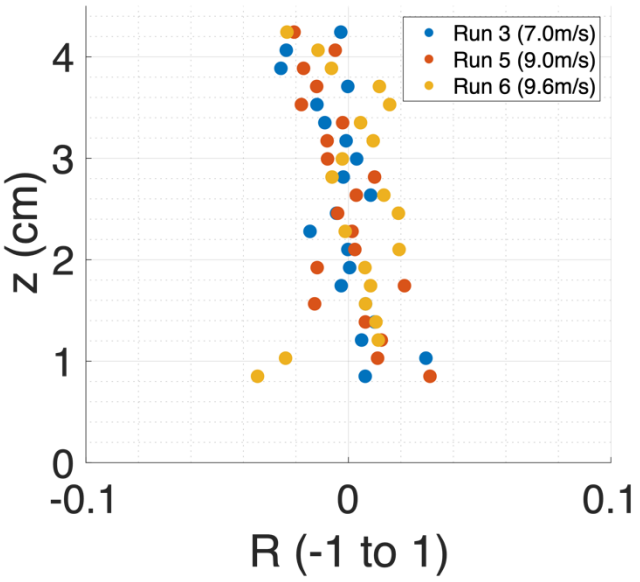

Figure 10: The correlation coefficient (R) vertical profiles for runs 3,5, and 6. Both figures highlight the very values and thus no detectable correlation between fluid and sand at this temporal scale. For each run and at each height, values are extremely small suggesting no detectable relationship at the given temporal resolution.

Discussion

Momentum Exchanges and Shear Stress Issues

Feedbacks between sand in motion and fluid flow have been an interest of aeolian geomorphologic research for a long time. Results from Figure 5 support previous findings on fluid-particle momentum exchanges (i.e., saltation results in visible deformation of the near-bed velocity profile). According to the Law of the Wall for clean air conditions (no sand), the velocity gradient increases with increasing freestream. This is the first of three important velocity profile characteristics for contextualizing results. Increases in the freestream velocity and near-bed velocity gradient (for sand-free conditions) directly result in increased shear stress and shear velocity (Bauer, 2013). The low wind speed runs 1- 3 ($U<=7.0\ ms^{-1}$) had essentially no sand flux.

These profiles match the clean air profiles report by Li and McKenna Neumann (2012) and follow this behavior.

Comparing the u-velocity profiles for run 4 (U=8.1 ms^{-1}) to runs 5 and 6 (U>=9.0 ms^{-1}), there is an interesting change in the trend below and above the transport (Fig. 5). In run 4, there is some sand transport but much less than the higher runs. Saltating particles decrease the mean u-velocities near the bed. This explains why the near bed (<0.1 z/δ) velocities for run 4 (U=8.1 ms^{-1}) are larger than runs 5 and 6 (U>=9.0 ms^{-1}). There is less fluid momentum loss to saltating particles within the transport layer during run 4 compared to runs 5 and 6. This is the second important characteristic of velocity profiles.

Lastly, note that the mean u-velocity nearest the bed for run 6 is approximately equal to run 3 (~3.5 ms^{-1}) and less than run 4 (~4 ms^{-1}). Yet, the run 6 u-velocities quickly surpass the profiles of runs 1-4 above 0.1 (z/δ). The third important velocity profile characteristics is that increases in sand concentration results in increases in the fluid velocity gradients (more deformation) within the transport layer.

All three characteristics described above are important to understanding changes in shear stress within the transport layer. In general, above the transport layer, dimensionless RS increases with freestream but decreases with height (Fig. 6C). Yet the sand laden runs 4-6 (U>=8.1 ms^{-1}) show much smaller RS decrease with height. Results support previous findings that stress perturbation caused by grain-borne momentum extraction can extend beyond the transport layer and into the outer layer of flow (e.g., Bauer et al., 2004; Li and McKenna Neuman, 2012). This directly relates to issues in calculating shear velocities from vertical profiles.

Furthermore, results from the sand-laden runs 4-6 (U>=8.1 ms^{-1}, Fig. 8C) show lower dimensionless RS than runs 1-3 closest to the bed. Within the transport layer, the dimensionless RS increases with height but decrease with saltation. Below 0.07 (z/δ) corresponds with increasing of sand concentration extracting fluid momentum and decreases in mean u-velocity. This finding has two implications. First, our results support Li and McKenna Neuman's (2012) finding that turbulent Reynolds stress continual decrease toward the surface of the mobile bed

when saltation is present suggest that neither the grain- or air-borne stress is constant within the saltation layer (Li & McKenna Neuman, 2012). Secondly, Figure 8C shows that saltation influences the relationship between dimensionless RS and height. This supports Owen's (1964) theory that aeolian saltation modifies the fluid velocity profile's apparent roughness height.

Causes of Increased Turbulence with Saltation

It has been shown that introducing particles to a flow may modify the turbulence, even at low particle concentrations (Hestroni, 1989). Our results support previous findings that particle concentration increases turbulence intensities. Earlier wind tunnel studies have measured the fluid turbulence intensity and RS in the presence of saltating particles using LDA (Taniere et al., 1997; Li & McKenna Neumann, 2012) and PIV/PTV (Zhang et al., 2008) methods. There seems to be a consensus that dimensionless RS decreases near the bed with increasing saltation, but dimensionless u- and v-turbulence intensities increase.

Focusing first on turbulence intensities, the highest values occur with the most sand transport and closest to the bed. Though the u-turbulence intensities are generally larger, the v-turbulence intensities profiles within the saltation layer change shape with increasing saltation and have a larger difference near the bed when compared to u-turbulence intensities. Results shown in Figures 8A&B suggest that v-turbulence intensities are more influenced by the introduction of saltating particles than u-turbulence intensities. First, note that for runs 5 and 6, the v-turbulence intensities dramatically decrease with height within the saltation cloud. However, for runs with minimal or no sand transport, the profiles either remain constant or show slight increases, followed by sight decreases throughout the transport layer. Secondly, the near-bed v-turbulence intensities for run 6 to run 1 are 0.105 and 0.045, respectively. The range is smaller for the u-turbulence intensities, which are 0.15 and 0.13, respectively.

Multiple processes could result in increased turbulence from increased saltation, including fluctuations in sand concentration, near-bed fluid deformation, and particle wake. First, results from Chapter 1 show increases in sand concentration variability with increased flux. For

high wind speed runs, this results in large fluctuations of grain counts on the second timescale. An increase or decrease of twice the particles in motion would result in a modification of the flow. Thus, the randomness of the saltation process could be responsible for increased near-bed turbulence.

Secondly, as discussed above, the fluid profile becomes increasingly modified with saltation. The fluid deformation and increases to near-bed velocity gradient directly result in increased shear stress and shear velocity. It is important to note that the exuberance plots (Fig. 6E), so values approaching -1 for runs 5 and 6 near the bed (the same experimental run and location where turbulence is high, but RS is low). This means that though the turbulence intensities are high, the fluid motions are not contributing to RS.

Lastly, wake production can induce enhanced turbulence in the presence of saltating sand particles (Hetsroni, 1989). Zhang et al.'s (2008) hypothesize that a wake region can form behind individual spinning sand particles within the transport layer, and increased concentration would lead to overlap and interaction of individual particle's wake would begin to overlap and interact. Zhang et al.'s (2008) further argue that the seen stronger influence on v-turbulence intensities (compared to horizontal) suggests that particle trajectories influence turbulence. Near the bed, where v-turbulence intensities are highest, corresponds with converting horizontal particle momentum to vertical during particle-bed collisions. Impacts of particles on the sand bed, inter-particle collision, and even creep motion may interactively augment the wind turbulence further. Further analysis is needed to examine fluid characteristics around individual spinning sand particles to confirm this theory, which unfortunately cannot be achieved in this study due to the PIV window size.

Progress of Simultaneous PIV/PTV

Our results show the capability of PIV/PTV systems for further quantifying fluid-particle interactions throughout the saltation cloud. The vertical sand concentration profiles reported here match our previous results from runs without seeding (Chapter 1). Fluid characteristics (Figs. 8), including mean velocity, turbulence, and RS profiles, generally align with previous results

reported by Li and McKenna Neuman (2012) and Zhang et al. (2008). Thus, we are confident in the performance of our PIV/PTV system and related pre- and post-processing. Previously, PIV/PTV methods were considered too difficult for aeolian sand transport applications. For example, Li and McKenna Neuman (2012) opted to use the LDA approach because of the complexity of image processing, insufficient sand-eliminating algorithms, and difficulty maintaining a high concentration of seeding particles, all related to PIV methods. The open questions relating to sand particles generating turbulence, suggested by Zang et al. (2008) and echoed here, will require spatially contiguous data. Though reliable, LDA point measurements cannot quantify flow characteristics around moving sand particles. Thus, continued improvement of PIV/PTV systems and analysis is critical. These results highlight the great technological and computing progress made in the decade applied to aeolian research.

This work highlights two important gaps that future improvement to PIV/PTV can address. First, though no correlation was detected between changes in near-bed fluid velocities and sand concentration, that does not mean correlations would not be detected at different scales. Here, a fine temporal resolution (~2300 FPS) results in a temporal data limitation of only ~4.5 seconds of data. Thus, future projects must address this trade-off to collect data over longer durations. Then it will be possible to re-evaluate near-bed instantaneous correlations between fluid characteristics and sand flux. Secondly, LDA cannot address questions relating to particle wake production and turbulence. While our PIV window size currently limits us, future work can focus on employing experimental configurations specificity designed to address the important open issues.

Conclusion

Much effort has been made to measure turbulence in clean air flows and within saltation clouds. This wind tunnel experiment used a customized PIV/PTV to collect simultaneous measurements of fluid characteristics and sand particle trajectories within the near-bed saltation cloud across increasing freestream speeds. Results highlight the success of sand tracking and deriving wind characteristics from highspeed imagery data to quantify feedback between changes

in freestream velocities, sand concentration, and fluid turbulent characteristics at various heights above the bed.

Results suggest multiple sources of error in shear velocity estimates for estimating sand flux. The horizontal and vertical turbulence intensities generally increase with freestream velocity and saltation but decrease with height. Results show expected trends in mean u-velocity profiles within increasing saltation due to momentum exchanges. The modification of both mean flow characteristics and changes in turbulence intensity due to saltation highlight problems of calculation shear velocity from velocity profiles. The lack of observations of a constant stress layer within the saltation cloud is also problematic for the calculation and application of shear velocity for flux estimates and may partly explain why conventional sand transport models tend to overestimate sand transport. The existence of a constant stress region is a necessary assumption for applying the Law of the Wall and Prandtl-Von Karman equation to velocity profile measurements for deriving estimates of shear velocity and roughness length. Lastly, the increases in turbulence intensity with saltation suggesting apparent roughness length should also be adjusted for sand flux.

The increases in turbulence closest to the bed also corresponded with decreases in RS. Exuberance calculations confirm that the turbulence increases linked to saltation do not result in increased burst-sweep events or contributions to RS. Multiple sources were proposed for turbulence production, such as concentration fluctuations, flow deformation, and particle wake. However, the quantification of each is the beyond the scope of this work.

Direct measurements from PIV/PTV at the high level of precision reported in this study have not been previously reported for fully developed boundary layer flow with an equilibrated saltation cloud for a wide range of freestream velocities. These measurements can inform best practices of traditional field measurements, direct future PIV/PTV wind tunnel studies, and inform future refinements of numerical saltation models.

CONCLUSIONS

This dissertation's motivation rests in developing a better understanding of the mechanics of wind-driven sand transport, driven by observations noting substantial discrepancies between observed and modeled rates of sand transport (Sherman, et al., 2013). In particular, technological advances in software and equipment in the past decade offers opportunities to explore the mechanics of aeolian transport that might drive this ongoing discrepancy.

The first research chapter highlights the emergent behavior of the saltation cloud. The open-source PTV algorithm, TrackMate, successfully detected sand grains in motion and tracked their trajectories under different wind speeds and bed surface conditions. Results support previous findings that mean particle velocities do not scale with wind speed, which contradicts the shear-flux laws used in common models (e.g., Bagnold, 1936).

The velocity distribution characteristics (such as skewness, kurtosis, and modality) changed with increasing wind speed, sand transport, and height. At higher transport rates, = velocity distributions at all heights become more continuous (unimodal). These data are important when applying particle velocity to indicate transport mode (saltation, reptation, and creep) and for further describing the contributions of different modes to total sand flux.

The study also examined the influence of ripples, common features in sandy environments. Results show differences in transport modes across ripple slopes. On the stoss, particle velocities indicate both faster saltons and creeping particles, compared to few creeping particles on the lee. This supports findings in the second research as evidence of shadowing effects.

Particle trajectory results from the first research chapter have implications for improving sand flux and saltation models. First, the results do not support the shear-flux scale laws used in Bagnold-type equations. This may explain (some of) the large discrepancies between observed and predicted sand transport estimates. Secondly, empirical data from a range of transport rates is essential for validating numerical models. Analytical approaches have made great advances in explicitly simulating particle trajectories, the collision of particles with the bed, and momentum

transfers between the wind flow and saltating particles. However, these models require empirical data from field and laboratory experiments for parameterization and validation. Thus, reporting mean characteristics and full data distributions from the first research chapter has the potential to improve future numerical models.

The second research chapter highlights the utility of manual particle tracking to examine the characteristics of impacting, rebounding, and ejecta particles during splash events. Though time-intensive, manual tracking remains the only method to identify and characterize all particles involved in a single splash event within a dense saltation cloud. These results suggest that the complexity of splash dynamics is not completely captured by previous studies that use different grain materials, flattened beds, or single-grain collision experiments. Results align with previous findings regarding mean impact and rebound velocities and angles. Increasing wind speed did not significantly affect particle velocities for flat or rippled bed runs. Additionally, the distribution of impacts across the different ripple slopes suggests that shadowing effects influence splash dynamics. The influence of impact angle versus shadowing effects remains challenging to separate but should be the focus of future studies.

Of the digitized splash events, all but one impact resulted in a rebound. However, the probability of zero ejecta per splash event ranged from 0.44 to 0.81. Although infrequent, large splash events with three or more newly ejected particles were observed in most runs. Lastly, most newly ejected particles remained within 1 cm of the bed. These results contradict findings from non-sand collision experiments. Additional analysis is needed to confirm previously suggested alternative theories on why flux increases with wind speed (if particles remain constant).

Understanding the splash process in saltation is crucial for theoretical and numerical approaches to bedform migration theory, dust aerosol emission, land degradation, and desertification. However, collecting representative empirical data on the process is challenging due to the high sand concentration near the bed at higher wind speeds, the complexity introduced

by rippled bedforms, and the time-intensive manual digitization of grain trajectories when automated methods are not feasible.

The third research chapter uses combined PIV & PTV techniques to simultaneously measure fluid characteristics and sand particle trajectories within the near-bed saltation cloud. Data demonstrate the successful tracking of sand particles and the derivation of wind characteristics from high-speed imagery data, enabling the quantification of feedback between changes in freestream velocities, sand concentration, and fluid turbulent characteristics at different heights above the bed.

The increases in fluid velocity result in increases in turbulence. Highspeed runs within the saltation cloud correspond to the highest turbulence to mean velocity results. Exuberance calculations confirmed that the turbulence increases linked to saltation did not lead to elevated contributions to RS. Several potential sources were proposed for turbulence production, including concentration fluctuations, flow deformation, and particle wake. However, the quantification of each source was beyond the scope of the work.

The mean u-velocity fluid profiles exhibited expected trends with increasing saltation due to momentum exchanges. However, results suggest several sources of error in estimating shear velocity and resultant sand flux calculations. First, modification of mean flow characteristics with saltation poses challenges in accurately calculating shear velocity from velocity profiles. Additionally, the increases in turbulence intensity associated with saltation indicated the need for adjustments in apparent roughness length when considering sand flux. Lastly, results show an absence of a constant stress layer within the transport. This directly defies the assumption of a constant stress region necessary for applying the Law of the Wall to estimate shear velocity and roughness length.

Direct measurements obtained from PIV/PTV with the high precision reported in this research had not been previously reported for fully developed boundary layer flow with an equilibrated saltation cloud across a wide range of freestream velocities. These measurements contribute to the general body of knowledge on aeolian processes, as well as guide future wind

tunnel studies, inform refinements of numerical saltation models, and help establish better practices for traditional field measurements.

In summary, this process-oriented geomorphological dissertation incorporates advances in fluid mechanics, aerodynamics, and physics. Leveraging the advances in high-speed imaging and analysis, the results highlight dynamic feedbacks along fluid, sand and bedrocks through quantifying saltation cloud characteristics in the first research chapter. The second research chapter focuses on changing splash dynamics with wind speed and bedforms. The third research chapter deals with momentum exchanges between fluid flow and sand in transport that presented with further details on fluid turbulence characteristics.

REFERENCES

Anderson, R. S. (1987). A theoretical model for aeolian impact ripples. Sedimentology, 34(5), 943–956. https://doi.org/10.1111/j.1365-3091.1987.tb00814.x

Anderson, R. S., & Haff, P. K. (1988). Simulation of Eolian Saltation. Science, 241(4867), 820–823. https://doi.org/10.1126/science.241.4867.820

Anderson, R. S., Sørensen, M., & Willetts, B. B. (1991). A review of recent progress in our understanding of aeolian sediment transport. In O. E. Barndorff-Nielsen & B. B. Willetts (Eds.), Aeolian Grain Transport 1 (Vol. 1, pp. 1–19). Springer Vienna. https://doi.org/10.1007/978-3-7091-6706-9_1

Andreotti, B. (2004). A two-species model of aeolian sand transport. Journal of Fluid Mechanics, 510, 47–70. https://doi.org/10.1017/S0022112004009073

Baas, A. C. W., & Sherman, D. J. (2005). Formation and behavior of aeolian streamers. Journal of Geophysical Research: Earth Surface, 110(F3). https://doi.org/10.1029/2004JF000270

Baas, A. C. W., & Van Den Berg, F. (2018). Large-Scale Particle Image Velocimetry (LSPIV) of aeolian sand transport patterns. Aeolian Research, 34, 1–17. https://doi.org/10.1016/j.aeolia.2018.07.001

Bagnold, R. (1941). The physics of blown sand and desert dunes: New York. William Morrow & Company.

Bagnold, R. A. (1936). The Movement of Desert Sand. Proceedings of the Royal Society of London. Series A, Mathematical and Physical Sciences, 157(892), 594–620.

Bagnold, R. A. (1937). The Transport of Sand by Wind. The Geographical Journal, 89(5), 409–438. https://doi.org/10.2307/1786411

Bauer, B. O. (2013). 11.2 Fundamentals of Aeolian Sediment Transport: Boundary-Layer Processes. In J. F. Shroder (Ed.), Treatise on Geomorphology (pp. 7–22). Academic Press. https://doi.org/10.1016/B978-0-12-374739-6.00295-5

Bauer, B. O., & Davidson-Arnott, R. G. D. (2014). Aeolian particle flux profiles and transport unsteadiness. Journal of Geophysical Research, 22.

Bauer, B. O., Davidson-Arnott, R. G. D., Hesp, P. A., Namikas, S. L., Ollerhead, J., & Walker, I. J. (2009). Aeolian sediment transport on a beach: Surface moisture, wind fetch, and mean transport. Geomorphology, 105(1–2), 106–116. https://doi.org/10.1016/j.geomorph.2008.02.016

Bauer, B. O., Houser, C. A., & Nickling, W. G. (2004). Analysis of velocity profile measurements from wind-tunnel experiments with saltation. Geomorphology, 59(1–4), 81–98. https://doi.org/10.1016/j.geomorph.2003.09.008

Bechtold, B., Fletcher, P., Seamusholden, & Gorur-Shandilya, S. (2021). bastibe/Violinplot-Matlab: A Good Starting Point (v0.1) [Computer software]. Zenodo. https://doi.org/10.5281/ZENODO.4559847

Beladjine, D., Ammi, M., Oger, L., & Valance, A. (2007). Collision process between an incident bead and a three-dimensional granular packing. Physical Review E, 75(6), 061305. https://doi.org/10.1103/PhysRevE.75.061305

Best, J. (1993). On the interactions between turbulent flow structure, sediment transport and bedform development: Some considerations from recent experimental research. In N. J. Clifford, J. R. French, & J. Hardisty (Eds.), Turbulence: Perspectives on flow and sediment transport (pp. 61–92). Wiley.

Bradski, G. (n.d.). Bradski, G. (2000). The openCV library. Dr. Dobb's Journal: Software Tools for the Professional Programmer, 25(11), 120-123. [Computer software].

Butterfield, G. (1991). Grain transport rates in steady and unsteady turbulent airflows. In Aeolian Grain Transport 1 (pp. 97–122). Springer.

Butterfield, G. R. (1998). Transitional behaviour of saltation: Wind tunnel observations of unsteady winds. Journal of Arid Environments, 39(3), 377–394. https://doi.org/10.1006/jare.1997.0367

Chapman, C. A., Walker, I. J., Hesp, P. A., Bauer, B. O., & Davidson-Arnott, R. G. D. (2012). Turbulent Reynolds stress and quadrant event activity in wind flow over a coastal foredune. Geomorphology, 151–152, 1–12. https://doi.org/10.1016/j.geomorph.2011.11.015

Chen, Y., Zhang, J., Huang, N., & Xu, B. (2019). An Experimental Study on Splash Functions of Natural Sand-Bed Collision. Journal of Geophysical Research: Atmospheres, 2018JD029967. https://doi.org/10.1029/2018JD029967

Crassous, J., Beladjine, D., & Valance, A. (2007). Impact of a Projectile on a Granular Medium Described by a Collision Model. Physical Review Letters, 99(24), 248001. https://doi.org/10.1103/PhysRevLett.99.248001

Creyssels, M., Dupont, P., El Moctar, A. O., Valance, A., Cantat, I., Jenkins, J. T., Pasini, J. M., & Rasmussen, K. R. (2009). Saltating particles in a turbulent boundary layer: Experiment and theory. Journal of Fluid Mechanics, 625, 47–74. https://doi.org/10.1017/S0022112008005491

Davidson-Arnott, R. G. D., MacQuarrie, K., & Aagaard, T. (2005). The effect of wind gusts, moisture content and fetch length on sand transport on a beach. Geomorphology, 68(1–2), 115–129. https://doi.org/10.1016/j.geomorph.2004.04.008

Delorme, P., Nield, J. M., Wiggs, G. F. S., Baddock, M. C., Bristow, N. R., Best, J. L., Christensen, K. T., & Claudin, P. (2023). Field Evidence for the Initiation of Isolated Aeolian Sand Patches. Geophysical Research Letters, 50(4). https://doi.org/10.1029/2022GL101553

Dong, F., Liu, D., & He, D. (1995). Progresses and trends in the research of blown sand movement (in Chinese). Adv. Mech, 25, 368–391.

Dong, Z., Qian, G., Luo, W., & Wang, H. (2006). Analysis of the mass flux profiles of an aeolian saltating cloud. Journal of Geophysical Research, 111(D16), D16111. https://doi.org/10.1029/2005JD006630

Dong, Z., Wang, H., Liu, X., & Wang, X. (2004). A wind tunnel investigation of the influences of fetch length on the flux profile of a sand cloud blowing over a gravel surface. Earth Surface Processes and Landforms, 29(13), 1613–1626. https://doi.org/10.1002/esp.1116

Durán, O., Claudin, P., & Andreotti, B. (2011). On aeolian transport: Grain-scale interactions, dynamical mechanisms and scaling laws. Aeolian Research, 3(3), 243–270. https://doi.org/10.1016/j.aeolia.2011.07.006

El-Baz, F., & Hassan, M. H. A. (1986). Physics of desertification. Springer Netherlands.

Ellis, J. T., & Sherman, D. J. (2013). 11.6 Fundamentals of Aeolian Sediment Transport: Wind-Blown Sand. In J. F. Shroder (Ed.), Treatise on Geomorphology (pp. 85–108). Academic Press. https://doi.org/10.1016/B978-0-12-374739-6.00299-2

European Commission. Joint Research Centre. (2018). World atlas of desertification :rethinking land degradation and sustainable land management. Publications Office. https://data.europa.eu/doi/10.2760/9205

Everett, R. A., Miller, A. W., & Ruiz, G. M. (2018). Shifting sands could bring invasive species. Science, 359(6378), 878–878. https://doi.org/10.1126/science.aar7741

Farrell, E. J., Sherman, D. J., Ellis, J. T., & Li, B. (2012). Vertical distribution of grain size for wind blown sand. Aeolian Research, 7, 51–61. https://doi.org/10.1016/j.aeolia.2012.03.003

Gordon, M., & McKenna Neuman, C. (2009). A comparison of collisions of saltating grains with loose and consolidated silt surfaces. Journal of Geophysical Research, 114(F4), F04015. https://doi.org/10.1029/2009JF001330

Gordon, M., & Neuman, C. M. (2011). A study of particle splash on developing ripple forms for two bed materials. Geomorphology, 129(1), 79–91. https://doi.org/10.1016/j.geomorph.2011.01.015

Greeley, R. (2002). Saltation impact as a means for raising dust on Mars. Planetary and Space Science, 50(2), 151–155. https://doi.org/10.1016/S0032-0633(01)00127-1

Greeley, R., Blumberg, D. G., & Williams, S. H. (1996). Field measurements of the flux and speed of wind-blown sand. Sedimentology, 43(1), 41–52. https://doi.org/10.1111/j.1365-3091.1996.tb01458.x

Greeley, R., & Iversen, J. D. (1986). Wind as a Geological Process. Sedimentary Geology, 49(3–4), 299–300. https://doi.org/10.1016/0037-0738(86)90050-3

Greeley, R., Williams, S. H., & Marshall, J. R. (1983). Velocities of Windblown Particles in Saltation: Preliminary Laboratory and Field Measurements. In Developments in Sedimentology (Vol. 38, pp. 133–148). Elsevier. https://doi.org/10.1016/S0070-4571(08)70793-3

Guo, Z., Huang, N., Dong, Z., Van Pelt, R., & Zobeck, T. (2014). Wind Erosion Induced Soil Degradation in Northern China: Status, Measures and Perspective. Sustainability, 6(12), 8951–8966. https://doi.org/10.3390/su6128951

Hetsroni, G. (1989). Particles-turbulence interaction. International Journal of Multiphase Flow, 15(5), 735–746. https://doi.org/10.1016/0301-9322(89)90037-2

Hintze, J. L., & Nelson, R. D. (1998). Violin Plots: A Box Plot-Density Trace Synergism. The American Statistician, 52(2), 181. https://doi.org/10.2307/2685478

Ho, T. D., Valance, A., Dupont, P., & Ould El Moctar, A. (2011). Scaling Laws in Aeolian Sand Transport. Physical Review Letters, 106(9), 094501. https://doi.org/10.1103/PhysRevLett.106.094501

Ho, T. D., Valance, A., Dupont, P., & Ould El Moctar, A. (2014). Aeolian sand transport: Length and height distributions of saltation trajectories. Aeolian Research, 12, 65–74. https://doi.org/10.1016/j.aeolia.2013.11.004

Hunt, J. C. R., & Nalpanis, P. (1985). Saltating and suspended particles over flat and sloping surfaces. I. Modelling concepts II. Experiments and numerical simulations. In Proc. Intl. Workshop on the Physics of Blown Sand, 8. https://illiad.lib.asu.edu/illiad/illiad.dll?Action=10&Form=75&Value=1795157

Jiang, C.-W., J. R. Parteli, E., Dong, Z.-B., Zhang, Z.-C., Qian, G.-Q., Luo, W.-Y., Lu, J.-F., Xiao, F.-J., & Mei, F.-M. (2022). Wind-tunnel experiments of Aeolian sand transport reveal a bimodal probability distribution function for the particle lift-off velocities. CATENA, 217, 106496. https://doi.org/10.1016/j.catena.2022.106496

Jones, D. K. C. (2001). Blowing sand and dust hazard, Tabuk, Saudi Arabia. Geological Society, London, Engineering Geology Special Publications, 18(1), 171–180. https://doi.org/10.1144/GSL.ENG.2001.018.01.24

Kang, L., & Liu, D. (2010). Numerical investigation of particle velocity distributions in aeolian sand transport. Geomorphology, 115(1–2), 156–171. https://doi.org/10.1016/j.geomorph.2009.10.001

Kawamura, R. (1951). Study on sand movement by wind (Reports of Physical Sciences Research Institute of Tokyo University, pp. 95–112).

Kocurek, G., & Ewing, R. C. (2012). Source-to-Sink: An Earth/Mars Comparison of Boundary Conditions for Eolian Dune Systems. In J. P. Grotzinger & R. E. Milliken (Eds.), Sedimentary Geology of Mars (Vol. 102, p. 0). SEPM Society for Sedimentary Geology. https://doi.org/10.2110/pec.12.102.0151

Kok, J. F., Parteli, E. J. R., Michaels, T. I., & Karam, D. B. (2012). The physics of wind-blown sand and dust. Reports on Progress in Physics, 75(10), 106901. https://doi.org/10.1088/0034-4885/75/10/106901

Kok, J. F., & Renno, N. O. (2009). A comprehensive numerical model of steady state saltation (COMSALT). Journal of Geophysical Research: Atmospheres, 114(D17). https://doi.org/10.1029/2009JD011702

Krogstadt, P.-Å., & Antonia, R. A. (1999). Surface roughness effects in turbulent boundary layers. Experiments in Fluids, 27(5), 450–460. https://doi.org/10.1007/s003480050370

Lancaster, N. (2023). Geomorphology of Desert Dunes (2nd ed.). Cambridge University Press. https://doi.org/10.1017/9781108355568

Le Cessie, S., Goeman, J. J., & Dekkers, O. M. (2020). Who is afraid of non-normal data? Choosing between parametric and non-parametric tests. European Journal of Endocrinology, 182(2), E1–E3. https://doi.org/10.1530/EJE-19-0922

Leeder, M. R. (1983). On the Interactions between Turbulent Flow, Sediment Transport and Bedform Mechanics in Channelized Flows. In J. D. Collinson & J. Lewin (Eds.), Modern and Ancient Fluvial Systems (pp. 3–18). Blackwell Publishing Ltd. https://doi.org/10.1002/9781444303773.ch1

Lettau, K., & Lettau, H. (1978). Experimental and micrometeorological field studies of dune migration (Lettau, H. and Lettau, K. (Eds), Exploring the World's Driest Climate., pp. 110–147). University of Wisconsin-Madison IES Report.

Li, B., & Neuman, C. M. (2012). Boundary-layer turbulence characteristics during aeolian saltation. Geophysical Research Letters, 39(11). https://doi.org/10.1029/2012GL052234

Livingstone, I., & Warren, A. (Eds.). (2018). Aeolian geomorphology: A new introduction. Wiley-Blackwell.

Lorenz, R. D., Wall, S., Radebaugh, J., Boubin, G., Reffet, E., Janssen, M., Stofan, E., Lopes, R., Kirk, R., Elachi, C., Lunine, J., Mitchell, K., Paganelli, F., Soderblom, L., Wood, C., Wye, L., Zebker, H., Anderson, Y., Ostro, S., … West, R. (2006). The Sand Seas of Titan: Cassini RADAR Observations of Longitudinal Dunes. Science, 312(5774), 724–727. https://doi.org/10.1126/science.1123257

Luijendijk, A., Hagenaars, G., Ranasinghe, R., Baart, F., Donchyts, G., & Aarninkhof, S. (2018). The State of the World's Beaches. Scientific Reports, 8(1), 6641. https://doi.org/10.1038/s41598-018-24630-6

Manukyan, E., & Prigozhin, L. (2009). Formation of aeolian ripples and sand sorting. Physical Review E, 79(3), 031303. https://doi.org/10.1103/PhysRevE.79.031303

Martin, R. L., & Kok, J. F. (2017). Wind-invariant saltation heights imply linear scaling of aeolian saltation flux with shear stress. Science Advances, 3(6), e1602569. https://doi.org/10.1126/sciadv.1602569

Martínez, M. L., Psuty, N. P., & Lubke, R. A. (2004). A perspective on coastal dunes. Coastal Dunes: Ecology and Conservation, 3–10.

McEwan, I. K., & Willetts, B. B. (1991). Numerical model of the saltation cloud. In O. E. Barndorff-Nielsen & B. B. Willetts (Eds.), Aeolian Grain Transport 1 (Vol. 1, pp. 53–66). Springer Vienna. https://doi.org/10.1007/978-3-7091-6706-9_3

McEwan, I. K., Willetts, B. B., & Rice, M. A. (1992). The grain/bed collision in sand transport by wind. Sedimentology, 39(6), 971–981. https://doi.org/10.1111/j.1365-3091.1992.tb01991.x

McKenna Neuman, C., Gillies, J. A., O'Brien, P., Saarenvirta, G., & Nickling, W. G. (2023). Development of ornamentation on ventifacts: An examination of flow and saltation kinematic mechanisms. Earth Surface Processes and Landforms, 48(3), 555–568. https://doi.org/10.1002/esp.5502

Mitha, S., Tran, M. Q., Werner, B. T., & Haff, P. K. (1986). The grain-bed impact process in aeolian saltation. Acta Mechanica, 63(1–4), 267–278. https://doi.org/10.1007/BF01182553

Nalpanis, P., Hunt, J. C. R., & Barrett, C. F. (1993). Saltating particles over flat beds. Journal of Fluid Mechanics, 251, 661–685.

Namikas, S. L. (2003). Field measurement and numerical modelling of aeolian mass flux distributions on a sandy beach. Sedimentology, 50(2), 303–326. https://doi.org/10.1046/j.1365-3091.2003.00556.x

Neuman, C. M. (2004). Effects of temperature and humidity upon the transport of sedimentary particles by wind. Sedimentology, 51(1), 1–17. https://doi.org/10.1046/j.1365-3091.2003.00604.x

Neuman, C. M., & Nickling, W. G. (1994). Momentum extraction with saltation: Implications for experimental evaluation of wind profile parameters. Boundary-Layer Meteorology, 68(1–2), 35–50. https://doi.org/10.1007/BF00712663

Nickling, W. G., & Neuman, C. M. (2009). Aeolian sediment transport. In Geomorphology of desert environments (pp. 517–555). Springer.

Nordstrom, K. F. (1994). Beaches and dunes of human-altered coasts. Progress in Physical Geography: Earth and Environment, 18(4), 497–516. https://doi.org/10.1177/030913339401800402

North, H. (2014). The effect of fetch on the development of the saltation carpet [Unpublished Honours thesis]. Trent University.

O'Brien, P., & McKenna Neuman, C. (2012). A wind tunnel study of particle kinematics during crust rupture and erosion. Geomorphology, 173–174, 149–160. https://doi.org/10.1016/j.geomorph.2012.06.005

O'Brien, P., & McKenna Neuman, C. (2016). PTV measurement of the spanwise component of aeolian transport in steady state. Aeolian Research, 20, 126–138. https://doi.org/10.1016/j.aeolia.2015.11.005

Oger, L., Ammi, M., Valance, A., & Beladjine, D. (2005). Discrete Element Method studies of the collision of one rapid sphere on 2D and 3D packings. The European Physical Journal E, 17(4), 467–476. https://doi.org/10.1140/epje/i2005-10022-x

Owen, P. R. (1964). Saltation of uniform grains in air. Journal of Fluid Mechanics, 20(2), 225–242. https://doi.org/10.1017/S0022112064001173

Ozer, P., Laghdaf, M. B. O. M., Lemine, S. O. M., & Gassani, J. (2007). Estimation of air quality degradation due to Saharan dust at Nouakchott, Mauritania, from horizontal visibility data. Water, Air, and Soil Pollution, 178(1–4), 79–87. https://doi.org/10.1007/s11270-006-9152-8

Parteli, E. J. R. (2022). Physics and Modeling of Wind-Blown Sand Landscapes. In Treatise on Geomorphology (pp. 20–52). Elsevier. https://doi.org/10.1016/B978-0-12-818234-5.00158-9

Prandtl, L. (1932). Zur turbulenten Strömung in Rohren und längs Platten. In Ergebnisse der aerodynamischen Versuchsanstalt zu Göttingen Lfg. 4 (pp. 18–29). De Gruyter. https://doi.org/10.1515/9783486764406-006

Prigozhin, L. (1999). Nonlinear dynamics of Aeolian sand ripples. Physical Review E, 60(1), 729–733. https://doi.org/10.1103/PhysRevE.60.729

Rasmussen, K. R., & Mikkelsen, H. E. (1998). On the efficiency of vertical array aeolian field traps. Sedimentology, 45(4), 789–800. https://doi.org/10.1046/j.1365-3091.1998.00179.x

Rasmussen, K. R., & Sørensen, M. (2008). Vertical variation of particle speed and flux density in aeolian saltation: Measurement and modeling. Journal of Geophysical Research, 113(F2), F02S12. https://doi.org/10.1029/2007JF000774

Rasmussen, K. R., Valance, A., & Merrison, J. (2015). Laboratory studies of aeolian sediment transport processes on planetary surfaces. Geomorphology, 244, 74–94. https://doi.org/10.1016/j.geomorph.2015.03.041

Ravi, S., D'Odorico, P., Breshears, D. D., Field, J. P., Goudie, A. S., Huxman, T. E., Li, J., Okin, G. S., Swap, R. J., Thomas, A. D., Van Pelt, S., Whicker, J. J., & Zobeck, T. M. (2011). AEOLIAN PROCESSES AND THE BIOSPHERE. Reviews of Geophysics, 49(3), RG3001. https://doi.org/10.1029/2010RG000328

Rice, M. A., & McEwan, I. K. (2001). Crust strength: A wind tunnel study of the effect of impact by saltating particles on cohesive soil surfaces. Earth Surface Processes and Landforms, 26(7), 721–733. https://doi.org/10.1002/esp.217

Rice, M. A., Willetts, B. B., & McEWAN, I. K. (1995). An experimental study of multiple grain-size ejecta produced by collisions of saltating grains with a flat bed. Sedimentology, 42(4), 695–706. https://doi.org/10.1111/j.1365-3091.1995.tb00401.x

Rice, M. A., Willetts, B. B., & McEWAN, I. K. (1996). Observations of collisions of saltating grains with a granular bed from high-speed cine-film. Sedimentology, 43(1), 21–31. https://doi.org/10.1111/j.1365-3091.1996.tb01456.x

Rioual, F., Valance, A., & Bideau, D. (2000). Experimental study of the collision process of a grain on a two-dimensional granular bed. Physical Review E, 62(2), 2450–2459. https://doi.org/10.1103/PhysRevE.62.2450

Sarre, R. (1987). Aeolian sand transport. Progress in Physical Geography, 11(2), 157–182.

Seeger, M. (2017). Experiments as tools in geomorphology. Cuadernos de Investigación Geográfica, 43(1), 7–17. https://doi.org/10.18172/cig.3207

Seely, M. (1991). The ecology of desert communities. In Sand dune communities (pp. 348–382).

Shaw, R. H., Tavangar, J., & Ward, D. P. (1983). Structure of the Reynolds Stress in a Canopy Layer. Journal of Climate and Applied Meteorology, 22(11), 1922–1931. JSTOR.

Sherman, D., Houser, C., & Baas, A. (2013). Electronic measurement techniques for field experiments in process geomorphology.

Sherman, D. J. (2020). Understanding wind-blown sand: Six vexations. Geomorphology, 107193. https://doi.org/10.1016/j.geomorph.2020.107193

Sherman, D. J., Davis, L., & Namikas, S. L. (2013). 1.13 Sediments and Sediment Transport. In Treatise on Geomorphology (pp. 233–256). Elsevier. https://doi.org/10.1016/B978-0-12-374739-6.00013-0

Sherman, D. J., & Ellis, J. T. (2022). Sand Transport Processes. In Treatise on Geomorphology (pp. 385–414). Elsevier. https://doi.org/10.1016/B978-0-12-818234-5.00165-6

Sherman, D. J., Jackson, D. W. T., Namikas, S. L., & Wang, J. (1998). Wind-blown sand on beaches: An evaluation of models. Geomorphology, 22(2), 113–133. https://doi.org/10.1016/S0169-555X(97)00062-7

Sherman, D. J., Li, B., Ellis, J. T., Farrell, E. J., Maia, L. P., & Granja, H. (2013). Recalibrating aeolian sand transport models. Earth Surface Processes and Landforms, 38(2), 169–178. https://doi.org/10.1002/esp.3310

Sherman, D. J., Li, B., Ellis, J. T., & Swann, C. (2018). Intermittent Aeolian Saltation: A Protocol For Quantification. Geographical Review, 108(2), 296–314. https://doi.org/10.1111/gere.12249

Sørensen, M. (1985). Estimation of some aeolian saltation transport parameters from transport rate profiles. Proceedings of the International Workshop on the Physics of Blown Sand, 8, 141–190.

Sterk, G., van Boxel, J. H., & Zuurbier, R. (2002). Interactions between turbulent wind flow and saltation sand transport. ICAR5/GCTE-SEN Joint Conference, International Center for Arid and Semiarid Lands Studies, 63–65.

Stout, J. E., & Zobeck, T. M. (1997). Intermittent saltation. Sedimentology, 44(5), 959–970. https://doi.org/10.1046/j.1365-3091.1997.d01-55.x

Swann, C., Lee, D., Trimble, S., & Key, C. (2021). Aeolian sand transport over a wet, sandy beach. Aeolian Research, 51, 100712. https://doi.org/10.1016/j.aeolia.2021.100712

Tanière, A., Oesterlé, B., & Monnier, J. C. (1997). On the behaviour of solid particles in a horizontal boundary layer with turbulence and saltation effects. Experiments in Fluids, 23(6), 463–471. https://doi.org/10.1007/s003480050136

Telfer, M. W., Parteli, E. J. R., Radebaugh, J., Beyer, R. A., Bertrand, T., Forget, F., Nimmo, F., Grundy, W. M., Moore, J. M., Stern, S. A., Spencer, J., Lauer, T. R., Earle, A. M., Binzel, R. P., Weaver, H. A., Olkin, C. B., Young, L. A., Ennico, K., Runyon, K., … Tyler, L. (2018). Dunes on Pluto. Science, 360(6392), 992–997. https://doi.org/10.1126/science.aao2975

Tessler, Z. D., Vörösmarty, C. J., Grossberg, M., Gladkova, I., Aizenman, H., Syvitski, J. P. M., & Foufoula-Georgiou, E. (2015). Profiling risk and sustainability in coastal deltas of the world. Science, 349(6248), 638–643. https://doi.org/10.1126/science.aab3574

The physics of Aeolian sand transport—ScienceDirect. (n.d.). Retrieved July 16, 2023, from https://www-sciencedirect-com.ezproxy1.lib.asu.edu/science/article/pii/S1631070515000079

Tinevez, J.-Y., Perry, N., Schindelin, J., Hoopes, G. M., Reynolds, G. D., Laplantine, E., Bednarek, S. Y., Shorte, S. L., & Eliceiri, K. W. (2017a). TrackMate: An open and extensible platform for single-particle tracking. Methods, 115, 80–90. https://doi.org/10.1016/j.ymeth.2016.09.016

Tinevez, J.-Y., Perry, N., Schindelin, J., Hoopes, G. M., Reynolds, G. D., Laplantine, E., Bednarek, S. Y., Shorte, S. L., & Eliceiri, K. W. (2017b). TrackMate: An open and extensible

platform for single-particle tracking. Methods, 115, 80–90. https://doi.org/10.1016/j.ymeth.2016.09.016

Tsoar, H., & Pye, K. (1987). Dust transport and the question of desert loess formation. Sedimentology, 34(1), 139–153. https://doi.org/10.1111/j.1365-3091.1987.tb00566.x

Ungar, J. E., & Haff, P. K. (1987). Steady state saltation in air. Sedimentology, 34(2), 289–299. https://doi.org/10.1111/j.1365-3091.1987.tb00778.x

Valance, A., Rasmussen, K. R., Ould El Moctar, A., & Dupont, P. (2015). The physics of Aeolian sand transport. Comptes Rendus Physique, 16(1), 105–117. https://doi.org/10.1016/j.crhy.2015.01.006

Walker, I. J., & Nickling, W. G. (2002). Dynamics of secondary airflow and sediment transport over and in the lee of transverse dunes. Progress in Physical Geography: Earth and Environment, 26(1), 47–75. https://doi.org/10.1191/0309133302pp325ra

Wang, D., Wang, Y., Yang, B., & Zhang, W. (2008). Statistical analysis of sand grain/bed collision process recorded by high-speed digital camera. Sedimentology, 55(2), 461–470. https://doi.org/10.1111/j.1365-3091.2007.00909.x

Wang, Z.-T., Zhang, C.-L., & Wang, H.-T. (2014). Intermittency of aeolian saltation. The European Physical Journal E, 37(12), 126. https://doi.org/10.1140/epje/i2014-14126-x

Werner, B. T. (1990). A Steady-State Model of Wind-Blown Sand Transport. The Journal of Geology, 98(1), 1–17.

Werner, B. T., & Haff, P. K. (1988). The impact process in aeolian saltation: Two-dimensional simulations. Sedimentology, 35(2), 189–196. https://doi.org/10.1111/j.1365-3091.1988.tb00944.x

Westerweel, J. (1994). Efficient detection of spurious vectors in particle image velocimetry data. Experiments in Fluids, 16–16(3–4), 236–247. https://doi.org/10.1007/BF00206543

White, B. (1996). Laboratory Simulation of Aeolian Sand Transport and Physical Modeling of Flow Around Dunes. Annals of Arid Zone, 35.

White, B. R., & Mounla, H. (1991). An experimental study of Froude number effect on wind-tunnel saltation. In O. E. Barndorff-Nielsen & B. B. Willetts (Eds.), Aeolian Grain Transport 1 (Vol. 1, pp. 145–157). Springer Vienna. https://doi.org/10.1007/978-3-7091-6706-9_9

White, B. R., & Schulz, J. C. (1977). Magnus effect in saltation. Journal of Fluid Mechanics, 81(03), 497. https://doi.org/10.1017/S0022112077002183

Willetts, B. B., & Rice, M. A. (1985). Intersaltation collisions. Proceedings of International Workshop on the Physics of Blown Sand University of Aarhus (Denmark), 1, 83–100.

Willetts, B. B., & Rice, M. A. (1986). Collisions in aeolian saltation. Acta Mechanica, 63(1–4), 255–265. https://doi.org/10.1007/BF01182552

Willetts, B. B., & Rice, M. A. (1989). Collisions of quartz grains with a sand bed: The influence of incident angle. Earth Surface Processes and Landforms, 14(8), 719–730. https://doi.org/10.1002/esp.3290140806

Williams, S. H. (1987). A comparative planetological study of particle speed and concentration during aeolian saltation. Arizona State University.

Wilson, I. G. (1972). AEOLIAN BEDFORMS-THEIR DEVELOPMENT AND ORIGINS. Sedimentology, 19(3–4), 173–210. https://doi.org/10.1111/j.1365-3091.1972.tb00020.x

Yager, E. M., & Schmeeckle, M. W. (2013). The influence of vegetation on turbulence and bed load transport. Journal of Geophysical Research: Earth Surface, 118(3), 1585–1601. https://doi.org/10.1002/jgrf.20085

Zhang, P., Sherman, D. J., & Li, B. (2021). Aeolian creep transport: A review. Aeolian Research, 51, 100711. https://doi.org/10.1016/j.aeolia.2021.100711

Zhang, W., Wang, Y., & Lee, S. J. (2008). Simultaneous PIV and PTV measurements of wind and sand particle velocities. Experiments in Fluids, 45(2), 241–256. https://doi.org/10.1007/s00348-008-0474-8

Zhang, X., Zhao, L., Tong, D., Wu, G., Dan, M., & Teng, B. (2016). A Systematic Review of Global Desert Dust and Associated Human Health Effects. Atmosphere, 7(12), 158. https://doi.org/10.3390/atmos7120158

Zingg, A. (1952). Wind tunnel studies of the movement of sedimentary material. In Proc. 5th Hydraulics Conf. IAHR.